2010년 2월

박사학위 논문

New Chemistry Based on Photonic Crystal Polymers and Nanomaterials

조 선 대 학 교 대 학 원

화 학 과

김 지 훈

New Chemistry Based on Photonic Crystal Polymers and Nanomaterials

광 결정 고분자와 나노소재를
기초로 한 새로운 화학

2010년 2월 25일

조 선 대 학 교 대 학 원

화 학 과

김 지 훈

New Chemistry Based on Photonic Crystal Polymers and Nanomaterials

지도교수 손 홍 래

이 논문을 이학박사학위신청 논문으로 제출함.

2009년 10월

조 선 대 학 교 대 학 원

화 학 과

김 지 훈

김지훈의 박사학위논문을 인준함

위원장   전남대학교   교수   우 희 권 (인)

위 원   단국대학교   교수   김 용 민 (인)

위 원   전남대학교   교수   정 현 담 (인)

위 원   조선대학교   교수   조 성 동 (인)

위 원   조선대학교   교수   손 홍 래 (인)

2009년 12월

조 선 대 학 교   대 학 원

TABLE OF CONTENTS

PART I. Electical and Optical Properties of Porous Silicon

CHAPTER ONE : INTRODUCTION OF POROUS SILICON

LIST OF SYMBOLS AND ABBREVIATIONS

PS	Porous silicon
TNT	Trinitrotoluene
HF	Hydrofluoric Acid
μm	Micrometer
%	Percent
m^3	Cubic Meter
c-Si	Crystalline Silicon
m	Mass
M	Molarity
NaOH	Sodium Hydroxide
FE-SEM	Field Emission-Scanning Electron Microscope
d	Density
CCD	Charge-Coupled Detector
A.U.	Arbitrary Units
PL	Photoluminescence
LED	Light Emitting Diode
Pt	Platinum
n	Refractive Index
Hz	Hertz
FWHM	Full-Width at Half-Maximum
nm	Nanometer
DBR	Distributed Bragg Reflector
BFG	Band Filter Gradient

THF	Tetrahydrofuran
FT-IR	Fourier Transform Infrared Spectroscopy
PSD	Porous Silicon Dioxide
CPT	Camptothecin
DMAP	4-di(methylamino)pyridine
DMEM	Dulbecco's Modified Eagle Medium
FBS	Fetal Bovine Serum
DMSO	Dimethyl Sulfoxide
UV-Vis	Ultraviolet-Visible
mA	Milliampere
mL	Milliliter
Ω	Ohm
XRD	X-ray Diffractometer
A_i	Amplitude
k_i	Frequency
λ	lambda
mmol	Millimole
PMMA	Polymethylmethacrylate
PSA	Particle Size Analyzer
TEM	Transmission Electron Microscope
SAED	Selected Area Electron Diffraction
SQUID	Superconducting Quantum Interference Device
MRI	Magnetic Resonance Imaging
Pt	Platinum
MER	Multi-encoded Rugate
PPR	Porous Polystyrene Replica

PBS	phosphate buffer solution
TOPO	Tri-*n*-octylphosphineoxide
V	Volume
μg	Microgram
π	Pi
Al	Aluminium
ε	Epsilon
ν	Nu
δ	Delta
Mw	Molecular Weight
σ	Sigma
t	Time
CdSe	Cadmium Selenide
B	current density
λ_{em}	Emission Wavelength
ODE	Octadecene
ODA	Octadecylamine
TOPO	Trioctylphosphine oxide
TBP	Tributylphosphine

LIST OF TABLES

LIST OF SCHEMES

LIST OF FIGURES

초 록

광 결정 고분자와 나노소재를 기초로 한 새로운 화학

박사과정 : 김 지 훈

지도교수 : 손 홍 래

조선대학교 화학과

현재 과학 기술은 과거의 과학 기술 발전 속도에 비해 대단히 빠른 속도로 발전하고 있다. 이중에서도 전기·전자 기술의 발달은 금속, 반도체 기술의 발전에 따라 최근 몇 십 년간 눈부신 발전을 이룩하였다. 현재 전자기술의 발전은 끊임없는 소자 크기의 감소를 통해 이루어지고 있으며, 이러한 경향은 전자 소자의 집적도 수준에서의 증가뿐만 아니라 동시에 소자 실행 속도의 증가라는 두 가지 목적을 두고 발전하였다. 하지만, 기존의 소자 기술은 이미 21세기 과학 및 기술의 요구를 충족하기 어려운 한계성이 예시되고 있으며, 당면한 문제점들을 해결하기 위한 새로운 형태 또는 크기를 갖는 소재가 필요하게 되었다. 이러한 요구 조건을 만족시킬 수 있는 새로운 21세기 연구 영역으로서 나노 과학(nanoscience)및 나노기술(nanotechnology)이 대두되고 있다. 나노 과학은 탄소 나노 튜브(CNT, carbon nanotube), C_{60}(buckyballs), 메조포러스 물질(mesoporous materials), 금속 및 반도체 나노 결정(nanocrystal, nanocluster, quantum dot) 등과 같은 물질 합성 분야와 STM, AFM, lithography를 통한 제어 및 응용 분야로 크게 두 가지로 분류 되고 있다. 특히, 화학 원리를 이용한 물질 합성 및 제어 나노 화학은 지난 수년간 괄목할 만한 획기적 연구가 진행되어 왔다. 나노 결정은 불연속적 전자 에너지 밀도를 가진 원자나 분자와 연속적 에너지 밴드를 가진 벌크

(bulk) 결정의 중간체이다. 따라서 나노 결정의 광학 및 전기적 성질은 벌크 결정 성질과 원자, 분자의 성질과는 다른 성질을 나타내게 된다. 이러한 나노 신소재 개발 분야는 기초과학에서부터 첨단과학까지의 융합학제 (interdisciplinary)간 학문 분야로 미래 기술의 선점 및 국가경쟁력 확보에 있어서 우위를 차지하는데 중요한 역할을 할 것으로 기대된다.

본 연구논문의 주제는 **"광 결정 고분자와 나노소재를 기초로 한 새로운 화학"**으로써, 반도체 실리콘 재료에 전기화학적 식각(etching)을 통해 제작된 광 결정(photonic crystal)을 함유하고 일정한 패턴의 나노크기의 기공을 갖는 다공성 실리콘(porous silicon)의 광학적 특성의 분석 및 응용에 대한 연구와 고분자를 이용하여 다공성 실리콘의 광 결정을 함유하는 역구조의 광 결정 고분자 복사체(porous polymer replica)의 제작 및 그것의 응용에 대한 연구를 목표로 한다. 이러한 광 결정을 기초로 한 기술은 광 결정소재의 광학적 특성과 광학 스펙트럼에 대한 조작의 가능성으로 인해, 화학·생물학적 센서나 의학적 진단요법에 매우 유용하게 활용될 수 있어 수년 동안 많은 연구가 이루어지고 있는 분야이다.

본 연구논문은 Part I, II 내에 11개의 Chapter들로 이루어져 있으며, part I에서는 높은 표면적에 나노크기의 기공을 갖는 다공성 실리콘의 간섭 막의 굴절률 조절로 인한 가시광선 및 적외선 영역에서 특정한 파장에서 좁은 반사 띠의 보강간섭을 갖는, 다층 다공성 실리콘(multilayer porous silicon)의 광학적 특성 및 그것의 응용에 대해 연구하였다. 또한 비대칭 식각을 통한 굴절율의 변화에 따른 Full Color Display로써의 광학적 특성의 변화에 대해 조사하고, 다공성 실리콘 필름의 물리적 불안정성을 보완하여 제작된 광학 필터로써의 가능성 제시하고 화학적 센서에 대한 응용에 대해 연구한 결과를 보여주는 Part이다. 또한, 다공성 실리콘 표면에 항암제인 Camptothecin 약물을 유도체화 시켜, 공유 접합(covalent attachment) 방법을 이용하여 targeted Delivery 와 controlled Release의 가능성에 대해 조사하고, 약물 전달 시스템(drug delivery system)으로써의 독성 검사 및 선택성과 효율성에 대해 조사한 연구결과를 조사하였다.

Part II에서는 다공성 실리콘의 구조를 이용한 고분자 복사체의 제작과 그것의 응용분야에 대해 조사하였다. 다공성 실리콘을 이용한 광 결정 고분자의 대한 연구는 University

of California의 Michael J. Sailor (2003년 Science, Vol. 299, p. 2045)에 의해 처음 보고되었으며, 본 연구에 사용된 광 결정 고분자 복사체는 광 결정의 구조를 갖는 광학 고분자 재료로써, 주물로 사용된 다공성 실리콘 구조의 역학 구조를 갖는 재료로써 다공성 실리콘에서 나타나는 광학적 특징이 그대로 나타난다. 본 연구에서는 광 결정 고분자 복사체를 제작하는 과정에서 기능성 나노입자를 합성하여, 고분자 용액에 자성 (magnetite, Fe_2O_3) 및 발광 (luminescence, CdSe) 나노 입자를 첨가하여 다양한 기능성을 갖는 광 결정 고분자 복사체의 제작에 대한 연구결과를 발표할 것이며, 광 결정 고분자 복사체를 화학 및 바이오센서로 응용하기 위해 avidin과 streptavidin과 자리결합을 할 수 있는 biotin 감지 인식 체를 혼합하여 고분자 복사체를 제작하여 광학 스펙트럼을 이용하여 생물분자를 감지할 수 있는 나노 바이오센서를 개발하였다.

최근 다공성 실리콘의 광학적 특성을 이용한 여러 응용분야에 접목하는 연구가 광범위하게 진행되고 있으나, 아직 다공성 실리콘을 주물로 이용하는 광 결정 고분자 복사체를 이용한 화학센서 또는 바이오센서의 개발이 다른 분야에 비하여 상대적으로 연구가 미흡한 상태이다. 광 결정을 함유하는 고분자 복사체를 이용한 바이오센서의 경우는 국내·외에서는 수행되지 않는 연구로써 처음으로 개발될 독창적인 연구이다. 또한 다양한 학문 분야의 지식을 바탕으로 한 학제 간 융합학문 분야의 연구 결과로서 아직까지 정확히 확립되지 않은 나노센서 (nanosensor), 나노바이오센서 (nano bio-sensor), 나노소재 (nanomaterial)의 분석 및 그 응용과 관련된 중요한 정보를 구축하는데 크게 기여하여 이 분야의 연구를 선도할 것으로 기대된다.

Part I.

Electical and Optical

Properties of Porous Silicon

Chapter One

Introduction of Porous Silicon

1.1 History of Porous Silicon

The Porous silicon (PS) was first discovered by accident in 1956 by Arthur Uhlir Jr. and Ingeborg at the Bell laboratories in the U.S. At the time, Ulhir and Ingeborg were in the process of developing a technique for polishing and shaping the surfaces of silicon and germanium [1]. However, it was found that under several conditions a crude product in the form of thick black, red or brown film were formed on the surface of the material. At the time, the findings were not taken further and were only mentioned in Bell's labs technical notes.

Despite the discovery of porous silicon in the 1950's, the scientific community was not interested in porous silicon until the late 1980's. At the time, L. T. Canham first reported efficient, tunable, room temperature luminescence in the visible range from PS [2] that interest in the field grew exponentially. From this point on, a large number of academic and industrial researchers from all over the world began to study the PS pore structure [3,4], light emission mechanism [5,6], surface chemistry [7,8], and feasibility for optoelectronic applications [9].

The published result stimulated the interest of the scientific community in its non-linear optical and electrical properties. The growing interest was evidenced in the number of published work concerning the properties and potential applications of porous silicon. In an article published in 2000, it was found that the number of published work grew exponentially in between 1991 and 1995. The many favorable

characteristics and the vast interest in PS have given rise to a variety of new applications such as light emitting devices [10], multi-layer structure [11], solar energy conversion [12], chemical and biological sensors [13-18], drug delivery application [19], ultrasound generators [20], micro-engineering [21], astrophysics [22], signal processing [23], and nuclear science [24]. Due to these multi-functional applications of PS, recently it has been proposed to be an educational vehicle for introducing nano-technology and inter-disciplinary materials science by eminent scientists in the field [25].

In 2001, a team of scientists at the Technical University of Munich inadvertently discovered that hydrogenated porous silicon reacts explosively with oxygen at cryogenic temperatures, releasing several times as much energy as an equivalent amount of TNT, at a much greater speed (an abstract of the study can be found below). Explosion occurs because the oxygen, which is in a liquid state at the necessary temperatures, is able to oxidize through the porous molecular structure of the silicon extremely rapidly, causing a very quick and efficient detonation. Although hydrogenated porous silicon would probably not be effective as a weapon, due to its functioning only at low temperatures, other uses are being explored for its explosive properties, such as providing thrust for satellites.

1.2 Electrochemical Preparation of Porous Silicon

1.2.1 Formation of Porous Silicon by Anodization

PS can be produced in many different ways. One method of introducing pores in
silicon is through the use of an anodization cell. A possible anodization cell
employs platinum cathode and silicon wafer anode immersed in Hydrofluoric acid
(HF) electrolyte. Corrosion of the anode is produced by running electrical current
through the cell. It is noted that the running of constant DC current is usually
implemented to ensure steady tip-concentration of HF resulting in a more
homogenous porosity layer although pulsed current is more appropriate for the
formation of thick silicon wafers bigger than 50 μm.

It was noted by Halimaoui that hydrogen evolution occurs during the formation
of porous silicon - "When purely aqueous HF solutions are used for the PS
formation, the hydrogen bubbles stick to the surface and induce lateral and in-depth
inhomogeneity" [26]. The hydrogen evolution is normally treated with absolute
ethanol in concentration exceeding 15%. It was found that the introduction of
ethanol eliminates hydrogen and ensures complete infiltration of HF solution within
the pores. Subsequently, uniform distribution of porosity and thickness is improved.

The extremely large surface to volume ratio (≥ 500 m^2/cm^3) of the PS
nano-structures, the its easy formation and control of the surface morphology
through variation of the formation parameters, its compatibility of silicon IC
technology and hence amenability to the development of smart system-on-chip
sensors-all these properties have made it to be a very attractive sensing material.

Although there is still some consideration regarding the surface dissolution
mechanism, it is commonly agreed that holes are required for the dissolution

mechanism to begin. The required holes are present in p-type crystalline silicon, but they need to be supplied for the dissolution process to be initiated in n-type crystalline silicon. Illumination is the most common way for supplying holes.

In normal anodization conditions, the surface of crystalline silicon is inert against hydrofluoric acid at low pH values. In 1991, Lehmann and Gösele [27] proposed a reaction model of the dissolution chemistry for the formation of PS. This formation mechanism is illustrated in Figure 1.1. This model is well accepted and proposes that when silicon is under anodic bias and holes reach the surface, nucleophilic attack of the silicon-hydrogen bonds by fluorine ions occurs. This attack gives rise to a silicon-fluorine bond as shown in Figure 1.1. Once fluorine is attached, its large electro-negativity polarizes the structure making it possible for another fluorine ion to bond to the surface. During this process, an electron is ejected into the electrode and hydrogen is released. At this point, the large polarization of two silicon-fluorine bonds lower the electron density from the silicon-silicon bonds, making them weak and vulnerable for attack by hydrofluoric acid and water. This results in the removal of a silicon atom in the form of the soluble ion SiF_6^{2-} and leaves the remaining silicon atoms hydrogen terminated. The overall reaction can be expressed as follows [28]:

$$2\,Si + 6\,HF + 2\,h^+ \longrightarrow \underset{\textbf{Porous Si Surface}}{\overset{\textbf{H}}{Si}} + H_2SiF_6 + 2H^+ + 1/2\,H_2$$
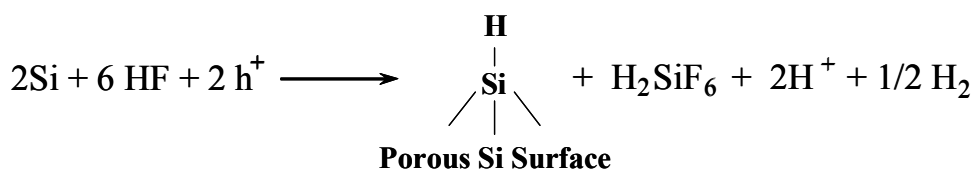
The removal of the silicon atom creates an atomic size dip or irregularity in the once atomically flat surface. The change in surface geometry concentrates the electric field lines on the irregularity site. PS pore formation and side-wall

dissolution will be inhibited by the depletion of holes. The depletion is caused by quantum confinement of charge carriers that results from the small dimensions of the pore walls. The quantum confinement increases the effective band-gap energy, making it more difficult for holes to enter the silicon region between the etched pores.
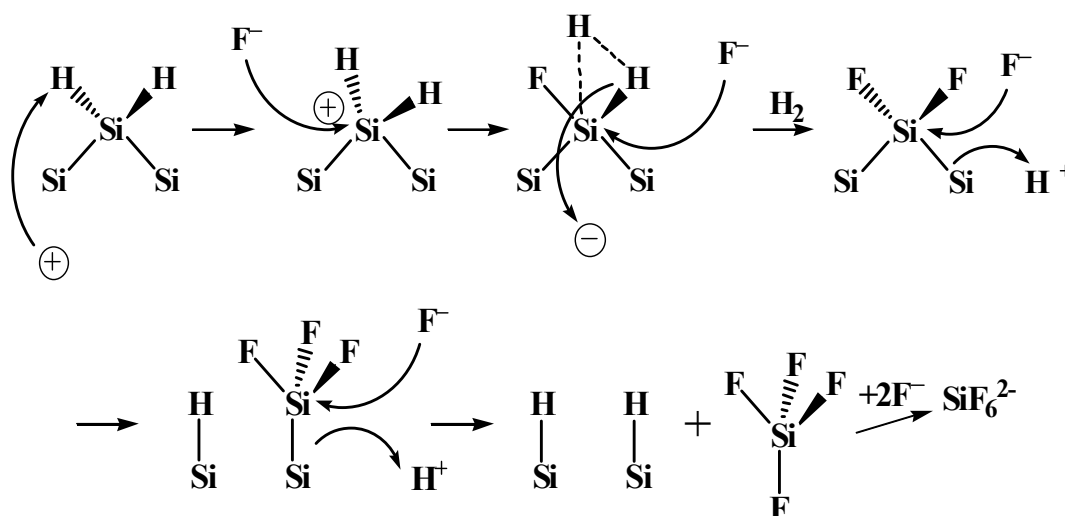
Figure 1.1. Dissolution mechanism of crystalline silicon in hydrofluoric acid associated with the formation of porous silicon.

1.2.2 Electrochemical Etching Setup

Figure 1.2 shows that a picture of experimental setup to produce PS. The anodization cell is made of Teflon, which is resistive against attack from the hydrofluoric acid electrolyte. The aluminum foil serves as the anode and it is sandwiched between the top and bottom parts of the Teflon cell. For a better contact, a platinum wire is placed against the silicon wafer where leads can be connected. The cathode is a circular platinum wire that is submerged in the hydrofluoric acid electrolyte. The cathode is held in place, three wing nuts hold the entire anodization cell together during the electrochemical etching process. The hydrofluoric acid electrolyte is placed inside the top part of the Teflon cell. Enough electrolyte must be present to supply the required fluorine ions and to cover the platinum wire cathode. The top part of the Teflon cell has a circular window of area 1.2 cm^2 which exposes the silicon to hydrofluoric acid and forms the PS. The entire electrochemical process is carried out under constant current supplied by a computer controlled Keithley 2420 power sourcemeter.
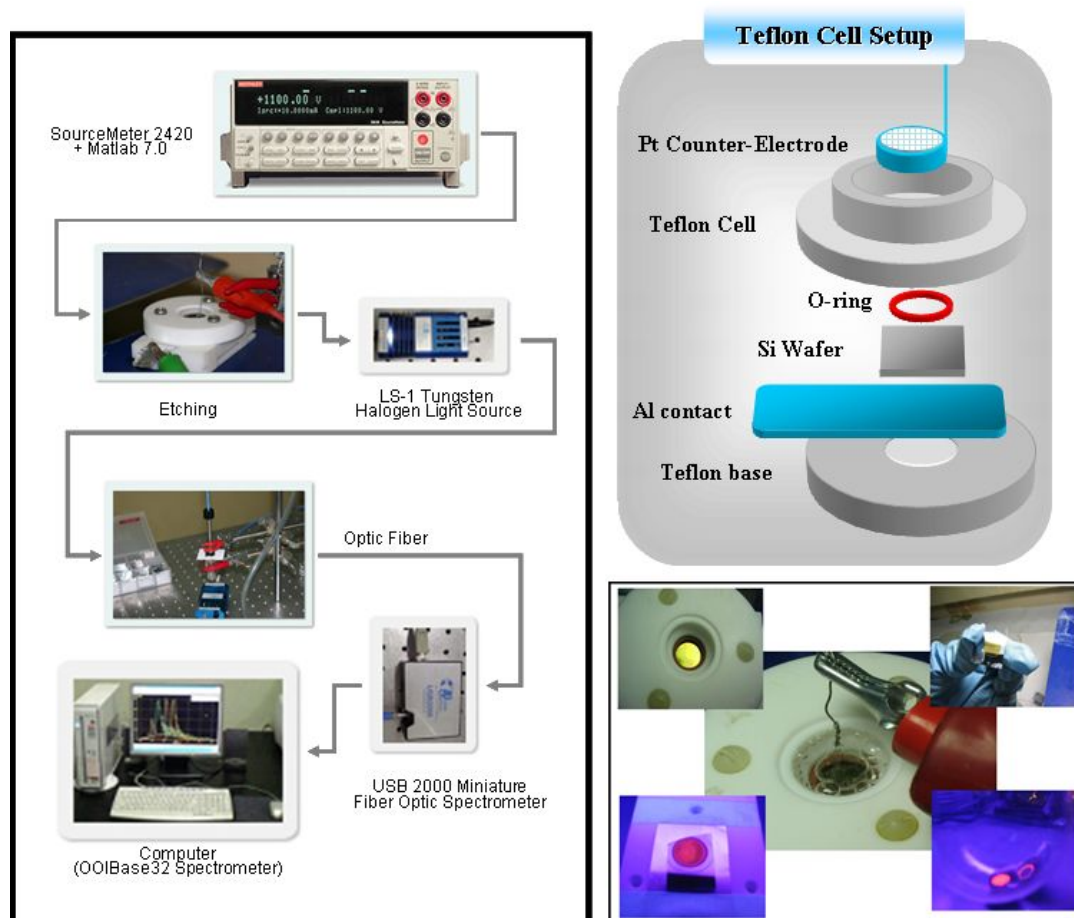
Figure 1.2. Experimental setup to produce porous silicon (left). Anodization is conducted under a constant current with the hydrofluoric acid electrolyte in the top of portion of the Teflon cell. The aluminum foil serves as the anode and the platinum wire as the cathode (right).

1.3 Control of the Morphology and Porosity

1.3.1 Current Density

The dissolution of silicon requires the presence of fluorine ions (F^-) and hole (h+). The pore initiation and growth mechanisms are qualitatively understood. Pore growth can be explained by several models, each one of which is more relevant in a specific regime of porosity and pore size [29-31]. IF the silicon/electrolyte interface becomes irregular shortly after etching starts, the surface fluctuations of the Si/electrolyte interface may either grow (PS formation) or disappear (electropolishing). A depletion region is formed in the thin PS layer itself and also in a region of the Silicon wafer near the PS/c-Si interface. In forward bias for p-type substrates, the holes can still reach the Si/electrolyte interface as the electric field lines are focused at the tip of the pores. Thus, holes will preferentially reach the Si/electrolyte interface deep in the pores, where etching will proceed rapidly (Figure 1.3). In contrast, no holes will reach the end of the Si rods, effectively stopping the etching there. In addition, if this electrostatic effect is not strong enough, the random walk of the holes toward the Si/electrolyte interface makes it more likely that they reach it at or near the pore's tip, resulting in an effect similar to the electrostatic one. When an n-type substrate is used, porous silicon formation takes place in reverse bias since holes are required for etching to proceed. Another important mechanism becomes predominant if the Si rods are narrow enough (typically much less than 10 nm). In this size regime, the electronic states start to differ from those of bulk silicon. When the motion of carriers is restricted in one or more dimensions, the holes in the valence band are pushed to lower energy by quantum confinement,

which produces a potential barrier to hole transport from the wafer to the Si rods. The holes can no longer drift or diffuse into the Si rods and further etching stops.
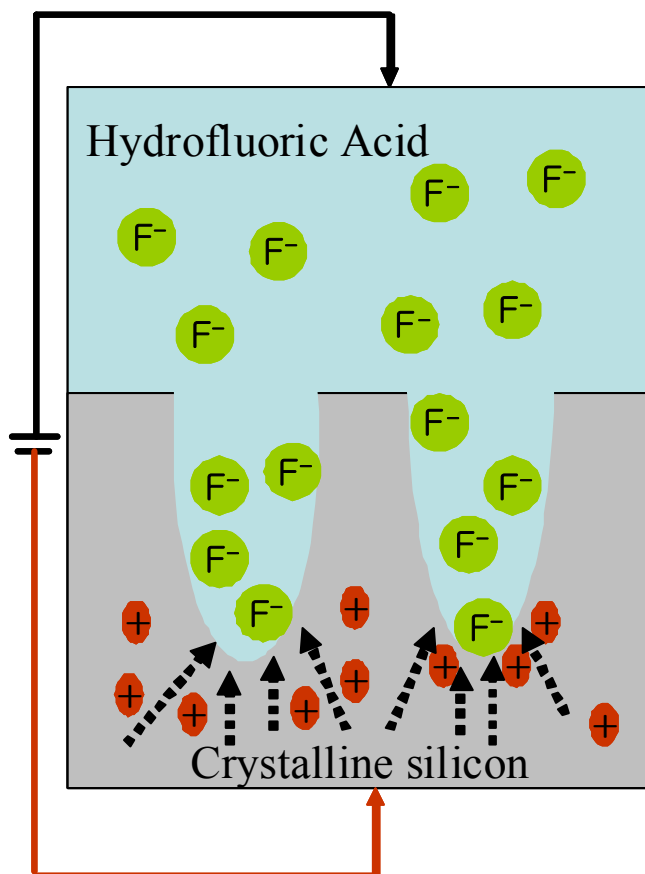
Figure 1.3. Schematic of PS formation. Etching occurs only at the pore tips where the holes (h^+) are focused by the electric field.

Pore formation occurs when the fluorine ions are delivered faster than the holes, the interpore regions of PS are depleted of holes, and further etching occurs only

at the pore tips. When the current density decreases, the number of holes at the pore tips drops, which leads to smaller pore sizes. Thus, the porosity (defined as the percentage of void space in the material) can be precisely controlled by the etching current density. As the current density increase, the silicon dissolution rate increases, resulting in a higher porosity and etching rate. Figure 1.4 shows that linear dependence of PS porosity and etching rate as a function of current density [32].

The most important quantity when characterizing a porous materials is the porosity which is defined as the ratio of the empty pore volume to the total volume. The porosity of a PS can be calculated gravimetrically using following equation [33]:

$$\text{Porosity (\%)} = \frac{m_1 - m_2}{m_1 - m_3}$$

Where m_1 is the mass of the initial silicon wafer in grams, m_2 is the mass of the silicon wafer after anodization in grams, m_3 is the mass of the silicon wafer after dissolution of the porous layer in grams. The dissolution of PS is performed using a 0.1 M aqueous solution of sodium hydroxide (NaOH).

This gravimetric method is applicable in cases where the PS layer is sufficiently thick (> 5 μm). The differnce in masses is larger than the amount of error induced in the measurements. However, when the PS layer is thin (< 200 nm), the mass difference is the same order of magnitude as the error in measurements, and the porosity value obtained is unreliable.
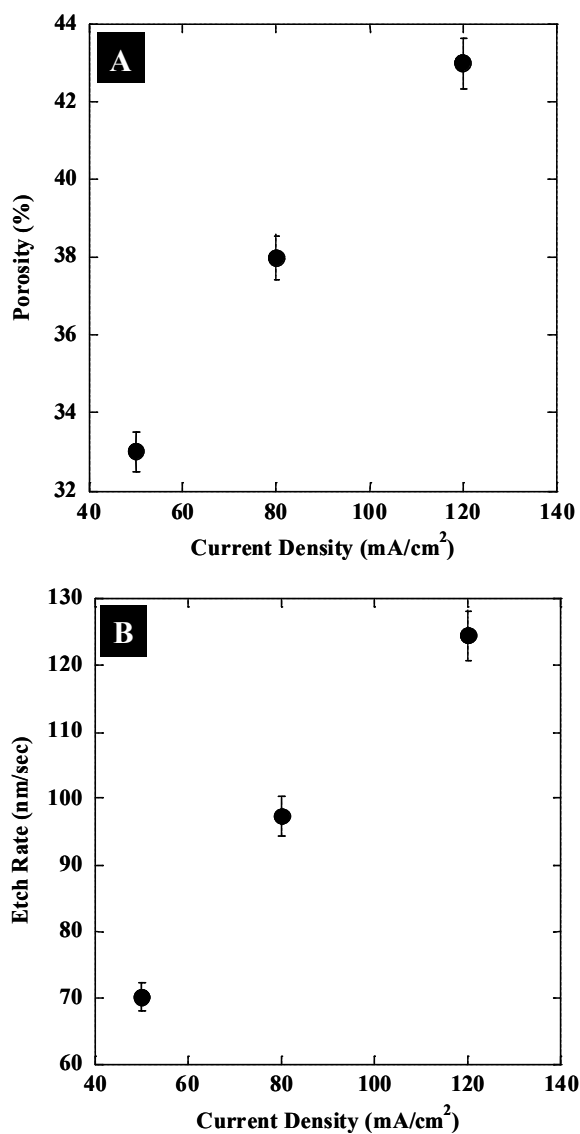
Figure 1.4. PS porosity (A) and etch-rate (B) dependence versus current density for p-type crystalline silicon substrate anodized in 35% hydrofluoric acid concentration electrolyte.

The size of pores formed during anodization is predominantly controlled by the current density [34], with an increase in the pore size corresponding to an increase in the current density. At low current densities, the pores are randomly directed. When the current density gradually increased, the diameter of PS pores increased. Figure 1.5 shows that surface images of etched PS with different current densities is measured by field emission-scanning electron microscope (FE-SEM, Hitachi-4800S).
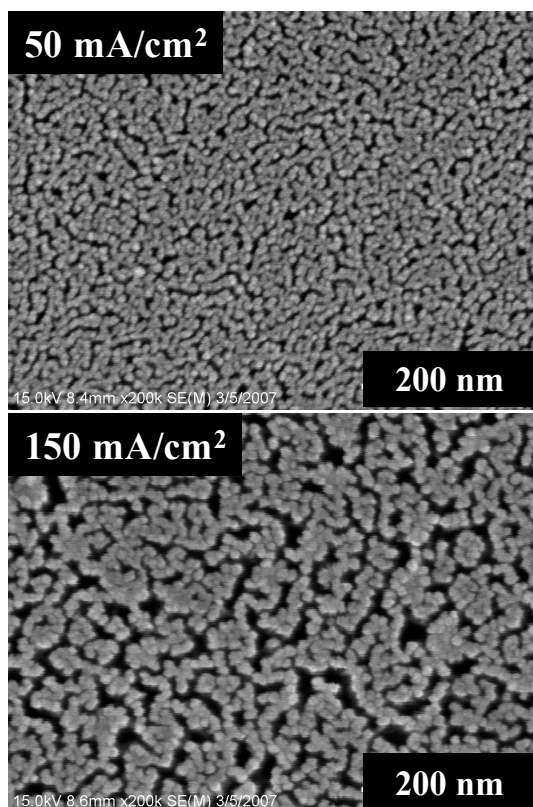
Figure 1.5. Surface FE-SEM images of PS with different current densities

1.3.2 Concentration of Etching Solution and Anodization Time

The composition of HF solution determines the etching process. In the anodization of PS, hydrofluoric acid with ethanol as an etchant solution is typically used. When aqueous HF solutions are used in the formation of PS, the hydrogen bubbles evolved stick to the surface. To improve the surface uniformity in PS, the hydrogen bubbles must be removed. The ethanol solution ensures the uniformity of the PS by removing the hydrogen bubbles from the PS surface and enables the HF penetration into the pores. Concentration of the hydrofluoric acid and etching time determine the PS porosity and thickness. For given time, porosity is inversely proportional to the HF concentration [35]. Therefore, lowering the HF concentration increase in the PS porosity. Since PS thickness is related to HF concentration, an increase in the HF concentration cause an increase in the PS thickness which in turn leads to a reduction of the PS porosity for a fixed time [36].

As the etching time is varied, the thickness and porosity of the PS layers change. Figure 1.6 shows that the thickness of the PS layer as a function of anodization time [37] for a p-type substrate that is etched at a constant current density of 50 mA/cm^2 in a 35% hydrofluoric acid solution. The figure shows a linear relationship between the etching time and the thickness of the PS layer.

The thickness of PS can be determined using either non-destructive or destructive techniques. One non-destructive technique is the use of an ellipsometer which requires the extensive understanding of the refractive index. For the PS samples, the index is difficult to determine since the porosity varies vertically with depth. There are two available destructive techniques that can be used with significant ease. One determines the approximate PS thickness using following equation:

$$\text{Thickness} = \frac{M_1 - M_3}{S \cdot d}$$

Where M_1 is the mass of the original silicon wafer, M_3 is the wafer with anodized material removed, S is the area of the PS sample, and d is the density of the silicon substrate.
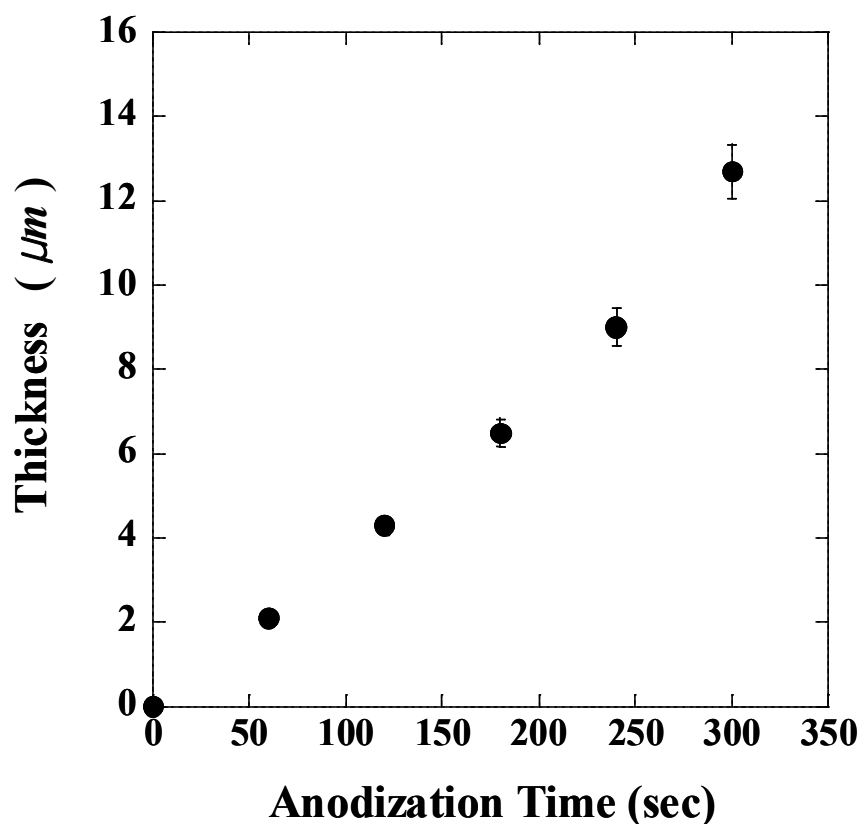
Figure 1.6. Thickness of PS with different anodization time for p-type crystalline silicon substrates anodized at a fixed current density of 50 mA/cm^2.

The second and more accurate technique uses a FE-SEM after scribing the PS sample to visualize a cross sectional view. This technique can resolve the thickness of PS to a few nanometers as well as provide additional information on the PS morphology.

1.4 Optical Properties of Porous Silicon

Some properties, such as porosity, refractive index, thickness, pore diameter, multi-structures, and optical properties, are strongly dependent on the anodization process parameters. These parameters include HF concentration, current density, anodization time, and silicon wafer type and resistivity.

1.4.1 Substrate Properties

Silicon substrates are identified by properties such as dopant type (i.e., n-type or p-type), substrate resistivity, dopant concentration, and substrate orientation. During anodization, dopant of the silicon substrate plays a significant role. Since holes (h^+) are the most important element in the chemical reaction leading to the formation of PS, the use of p-type wafer is the most popular. However, n-type wafer can be used with external illumination.

Substrate resistivity determines the achievable thickness of PS. For example, a very low resistivity wafer (<0.01 Ω-cm) is capable of producing thicker PS compared to a wafer with a higher resistivity (>10 Ω-cm) under same anodization conditions.

The morphology of the PS can be grouped into four categories based on doping concentration: p, p^+, p^{++}, n, n^+, and n^{++}. For p-type silicon wafer, the pore diameters and interpore spacing are very small (20-100 Å). As the dopant concentration increases, the pore diameter and spacing increase slightly (100-1000 Å). For n-type silicon, the pore diameters are considerably larger than those of the p-type substrate.

Substrate orientation is also important in the structure of the PS morphology. The main pore growth direction is essntially the same irrespective of the substrate orientation, dopant concentration or anodization conditions [38-39].

1.4.2 Refractive Index of Porous Silicon

The complex refractive index determines how light waves progagate inside a materials [40]. The refractive index is one of the important property of PS. This property controls the reflection and transmission of waves incident on the PS-air interface. There are many approximations that predict the refractive index of PS based on porosity [41-42]. However, none of them covers the entire porosity range with the same degree of high accuracy.

The refractive index of PS is calculated by using the Bruggeman approximation as described below :

$$\textbf{(1-P)}\ \frac{\varepsilon_{\text{Silicon}} + \varepsilon_{\text{porous silicon}}}{\varepsilon_{\text{Silicon}} + 2\varepsilon_{\text{porous silicon}}} + \textbf{(P)}\ \frac{\varepsilon_{\text{air}} + \varepsilon_{\text{porous silicon}}}{\varepsilon_{\text{air}} + 2\varepsilon_{\text{porous silicon}}} = \textbf{0}$$

where P is the porosity of porous silicon, $\varepsilon_{\text{silicon}}$ is the dielectric constant of silicon, ε_{air} is the dielectric constant of air, and $\varepsilon_{\text{porous silicon}}$ is the dielectric constant of porous silicon. The values of refractive indices for various porosities can be used to design PS layer stacks whose optical properies can be predicted quite accurately before production. It is clear that for any application of a material in optics or opto-electronics it is essential to know its refractive index.

1.4.3 Optical Properties and Bench Setup

The optical properties of PS are discussed in a wide spectral range from the infrared to the ultraviolet. PS has two optical properties such as photoluminescence (PL) for n-type with external illumination (300 W tungsten lamp) and optical reflectivity (Fabry-Pérot fringe) for p-type as shown in Figure 1.7. The ability of PS to emit and reflect in visible range is the most attractive property of the material. One explanation for the visible luminescence is based on the nanometer-size crystalline structure for PS [43-45].

PL spectrum of PS has been obtained with Ocean Optics LS-1 (blue LED). Optical reflectivity spectrum of PS showing Febry-Pérot fringe pattern has been measured by using tungsten-halogen lamp and an Ocean Optics S2000 charge-coupled detector (CCD) spectrometer fitted with a fiber optic input. The reflected light collection end of the fiber optic is positioned at the focal plane of the optical microscope as described in Figure 1.8.
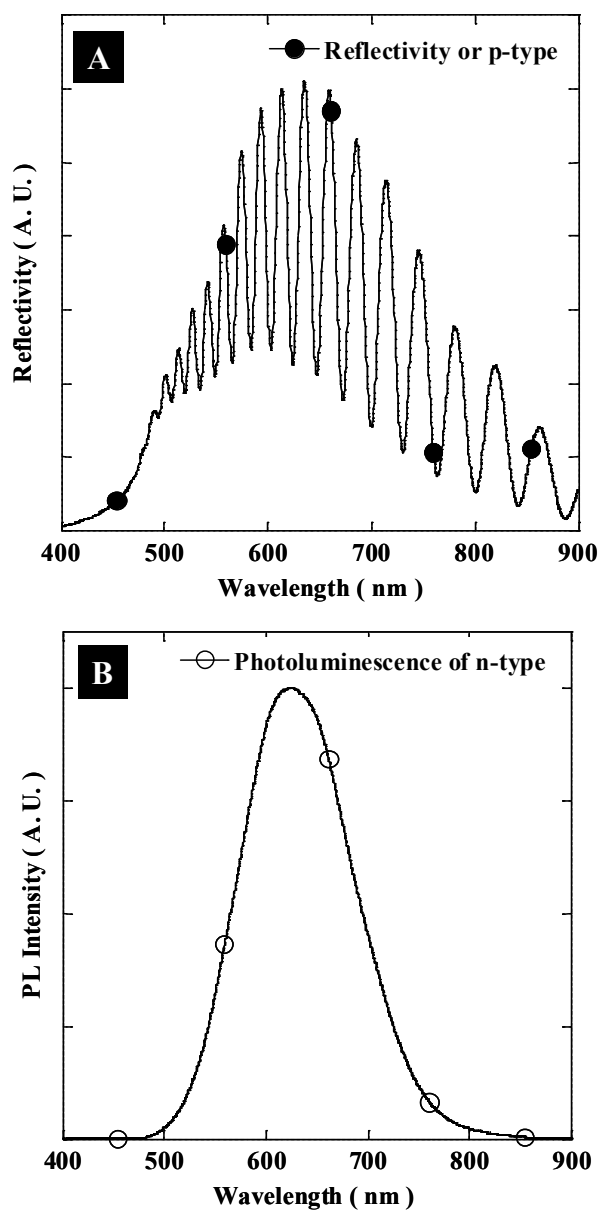
Figure 1.7. Optical properties of porous silicon; reflectivity (top) and photoluminescence (bottom).
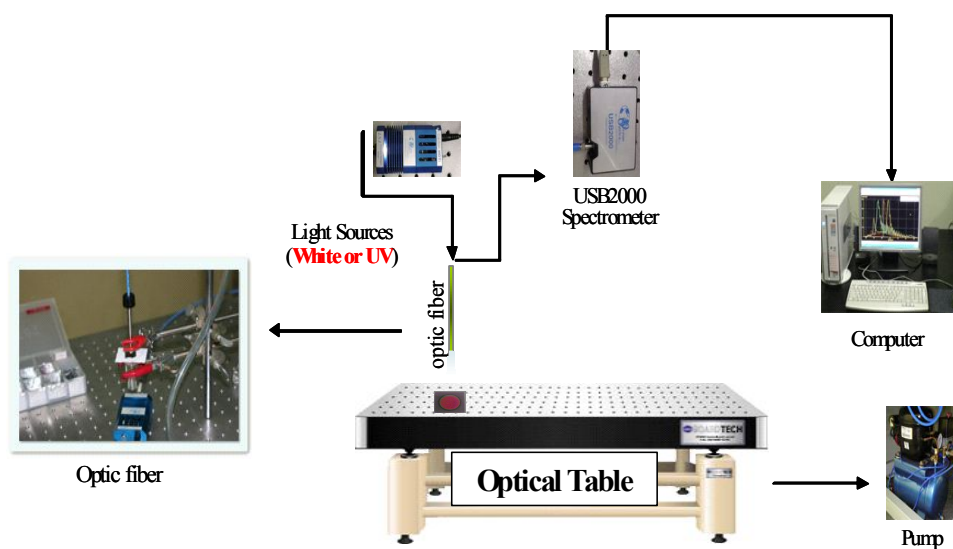
Figure 1.8. Optical bench setup for obtaining the optical properties of porous silicon

1.5 references

[1] A. Uhlir, "Electrolytic shaping of germanium and silicon," *Bell Syst. Tech. J.* **35**, 333-347 (1956).

[2] L. T. Canham, *Appl. Phys. Lett.* **57**, 1046 (1990).

[3] A. G. Cullis and L. T. Canham, *Nature* **353**, 335 (1991).

[4] Z. Sui, P. P. Leong, I. P. Herman, G. S. Higashi, and H. Temkin, *Appl. Phys. Lett.* **60**, 2086 (1992).

[5] C. Delerue, G. Allan, and M. Lannoo, *Phys. Rev. B* **48**, 11024 (1993).

[6] F. Koch, V. Petrova-koch, T. Muschik, A. nikolov, and V. Gavrilenko, *Mater. Res. Soc. Symp. Proc.* **298**, 319 (1993).

[7] E. J. Lee, T. W. Bitner, J. S. Ha, M. J. Shane, and M. J. Sailor, *J. Am. Chem. Soc.* **118**, 5375 (1996).

[8] J. M. Buriak and M. J. Allen, *J. Am. Chem. Soc.* **120**, 1339 (1998).

[9] A. Richter, P. steiner, F. Kozlowski, and W. Lang, *IEEE Electron Device Lett.* **12**, 691 (1991).

[10] K. D. Hirschmann, L. Tsybeskov, S. P. Duttagupta, and P. M. Fauchet, *Nature* **384**, 338 (1996).

[11] C. Mazzoleni and L. Pavesi, *Appl. Phys. Lett.* **67**, 2983 (1995).

[12] G. Smestad, M. Kunst, and C. Vial, *Sol. Energy Mater. Sol. Cells* **26**, 277 (1992).

[13] J. M. Lauerhaas and M. J. Sailor, *Science* **261**, 1567 (1993).

[14] H. Sohn, S. Letant , M. J. Sailor, and C. Trogler, *J. Am. Chem. Soc.* **122**, 5399 (2000).

[15] S. Letant and M. J. Sailor, *Adv. Mater.* **13**, 355 (2001).

[16] S. Chan, S. R. Horner, P. M. Fauchet, and B. L. Miller, *J. Am. Chem. Soc.* **123**, 11797 (2001).

[17] H. Sohn, R. M. Calhoun, M. J. Sailor, and W. C. Trogler, *Angew. Chem. Int. Ed.* **40**, 2104 (2001).

[18] H. Sohn, M. J. Sailor, D. magde, and W. C. Trogler, *J. Am. Chem. Soc.* **125**, 3821 (2003).

[19] X, Li, J. L. Coffer, Y. D. Chen, R. F. Pinizzotto, J. Newey, and L. T. Canham, *J. Am. Chem. Soc.* **120**, 11706 (1998).

[20] N. Koshida, T. Nakajima, M. Yoshiyama, K. Ueno, T. Nakagawa, and H. Shinoda, *Mater. Res. Soc. Symp. Proc.* **536**, 105 (1999).

[21] T. E. Bell, P. T. J. Gennissen, D. Demunter, and M. Kuhl, *J. Micromech. Microeng.* **6**, 361 (1996).

[22] V. G. Zubko , T. L. Smith, A. N. Witt, *Astrophys. J.* 501 (1998).

[23] V. P. Parkhutik, E. Matveeva, R. Perez, J. Alamo, and D. BeltraÂn, *Mater. Sci. Engn. B* **69-70**, 53 (2000).

[24] V. P. Bondarenko, Y. V. Bogatirev, J. P. Colinge, L. N. Dolgyi, A. M. Dorofeev, and V. A. Yakovtseva, *IEEE. Trans. Nucl. Sci.* **44**, 1719 (1997).

[25] V. P. Parkhutik and L. T. Canham, *Phys. Stat. Sol. A* **182**, 591 (2000).

[26] A. Halimaoui, "Porous silicon formation by anodisation," in Properties of Porous Silicon, L. Canham, ed., (INSPEC, London, UK, 1997) 12-22.

[27] V. Lehmann and U. Gösele, *Appl. Phys. Lett.* **58**, 856 (1991).

[28] M. J. Sailor, J. L. Heinrich, and J. M. Lauerhaas, *Stud. Surface Sci. Cat.* **103**, 209 (1996).

[29] R. L. Smith and S. D. Collins, *J. Appl. Phys.* **71**, R1 (1992).

[30] A. G. Cullis, L. T. Canham, and P. D. J. Calcott, *J. Appl. Phys.* **82**, 909 (1997).

[31] V. Lehmann, *Electrochemistry of Silicon*, Wiley-VCH Verlag, GmbH (2002).

[32] H. Ouyang, M. Christophersen, R. Viard, B. L. Miller, and P. M. Fauchet,

Adv. Funct. Mater. **15**, 1851 (2005).

[33] D. Brumhead, L. T. Canham, D. M. Seekings, and P. J. Tufton, *Electrochim*. *Acta*. **38**, 191 (1993).

[34] W. Theiss, *Surf. Sci. Rep.* **29**, 91 (1997).

[35] S. M. Hossain, J. Das, S. Chakraborty, S. K. Dutta, and H. Saha, *Semicon*. *Sci. Tech*. **17**, 55 (2002).

[36] I. K. Itotia and R. F. Drayton, *IEEE Antenn. Propag. Soc*. **2**, 663 (2003).

[37] A. Halimaoui, Porous Silicon Science and Technology, edited by J. C. Vial and J. Derrien, Springer-Verlag, New York, p. 33 (1995).

[38] M. Christopersen, J. Carstensen, and H. Foll, *Phys*. *Stat*. *Sol*. *A* **182**, 601 (2000).

[39] S.-F. Chuang, S. D. Collins, and R. L. Smith, *Appl*. *Phys*. *Lett.* **55**, 675 (1989).

[40] See e.g. J. D. Jackson, *Classical Electrodynamics*, John Wiley & Sons, New York (1975).

[41] D. J. Bergman, *Phys*. *Rep*. *C* **43**, 377 (1978).

[42] H. Looyenga, *Physica* **31**, 401 (1965).

[43] S. Sawada, N. Hamada, N. Ookubo, *Phys*. *Rev*. *B* **49**, 5236 (1994).

[44] A. J. Read, R. J. Needs, K. J. Nash, L. T. Canham, P. D. J. Calcott, and A. Qteish, *Phys*. *Rev*. *Lett*. **69**, 1232 (1992).

[45] Y. Kanemitsu, H. Uto, Y. Masumoto, T. Futagi, and H. Mimura, *Phys*. *Rev*. *B* **48**, 2827 (1993).

Chapter Two

Fabrication and Optical Characterization of Full Color Stop Band Based on Rugate-Structured Porous Silicon

2.1 Introduction

The technology to manage and manipulate light by controlling absorption, luminescence, and reflection has been a great interest in modern display technology [1,2]. Photonic crystals have been extensively studied in recent years because of their unique optical properties and the possibility of modulating the spectral resonance of optical spectrum. The optical properties of porous silicon (PS) prepared by electrochemical etching of p-type silicon wafer in HF are one candidate of photonic structured materials using reflection. PS is a network of pores within an interconnected silicon matrix. Since the discovery of PS, PS has been intensively investigated for a variety of applications, such as chemical [3] and biological sensors [4], optical band pass filters [5], micro chemical reactors [6], micro fuel cells [7], and drug delivery [8], due to its high surface area [9], open pore structure, convenient surface chemistry, and optical signal transduction capability [10].

Despite the structural inhomogeneities at the nanoscale, PS grown on highly doped p-type Si substrate showed typical optical properties of a dielectric material with a single effective refractive index (n). The structure and photonic characteristics of the PS layer depend on the conditions of the anodizing process,

such as current density, temperature, composition ratio of the solution, and conductivity of the silicon substrate [11,12]. In particular, the porosity or n of the PS layer can be precisely controlled by altering the anodizing current density [11]. One dimensional photonic structure of PS layers based on sinusoidal waveform of porosity forms a rugate reflector [13-15], which displays a sharp reflection resonance in the optical reflectivity spectrum at a wavelength that is controlled by the etch parameters. In this work, the effect of an etching time for the formation of rugate photonic structure and the effect of a frequency for the reflection band characteristics of rugate PS were investigated.

2.2 Experiments

2.2.1 Sample Preparation

Rugate PS was prepared by an electrochemical etching of the heavily doped p^{++}-type Si (100) substrate (boron doped, polished on the (100) face, resistivity of 0.8-1.2 mΩ-cm, Siltronix, Inc.). The etching solution consists of a 1:3 by volume mixture of absolute ethanol (ACS reagent, Aldrich Chemicals) and aqueous 48% HF (ACS reagent, Aldrich Chemicals). Etching was carried out in a Teflon cell by using a two-electrode configuration with a Pt mesh counter electrode to have the structural homogeneities. Rugate PS sample was prepared by using a computer-generated periodic sine wave current density. To prevent the photo-generation of carriers, the anodization was performed in the dark. All samples were then rinsed several times with ethanol and dried under Ar atmosphere prior to use.

2.2.2 Instrumentation and Data Acquisition

The anodization current was supplied by a Keithley 2420 high-precision constant current source which is controlled by a computer to allow the formation of PS multilayers. Optical reflectivity spectra were measured using a tungsten-halogen lamp in the wavelength rance 400-1200 nm and an Ocean Optics S2000 CCD spectrometer fitted with a fiber optic input. The reflected light collection end of the fiber optic was positioned at the focal plane of the optical microscope.

2.3 Results and Discussion

2.3.1 Effect of Etching Time

In order to generate periodic layers of sinusoidal refractive index profile, a computer-generated pseudo-sinusoidal current waveform was used. The sine waveform used in the present work was represented by

$$y_i = A_i[sin(k_it)] + B \quad \text{----------------} \quad (1)$$

where y_i represented a temporal sine wave of amplitude, A_i ; frequency, k_i ; time, t; applied current density, B. The values of k_i were from 0.28 Hz. The values of A_i and B were 11.55 and 63.05 mA, respectively. After all values were fixed, the etching time varied from 200 to 400, 600, 800, and 1000 s. Figure 1 showed reflectivity spectra of rugate PS with one reflection band while the etching time varied. A critical etching time of 200 s was needed to form rugate PS. The reflection resonance of rugate PS with 200 s of etching time occurred at 681 nm with sidelobes around the reflectance peak in the optical reflectivity and its full width at half maximum (FWHM) was 14 nm. The reflection band of rugate PS shifted to shorter wavelength by about 30 nm as the etching time increased, however their FWHMs of the reflection band were almost identical. The reflection band of rugate PS placed at the same position while the etching time was over 1000 s.
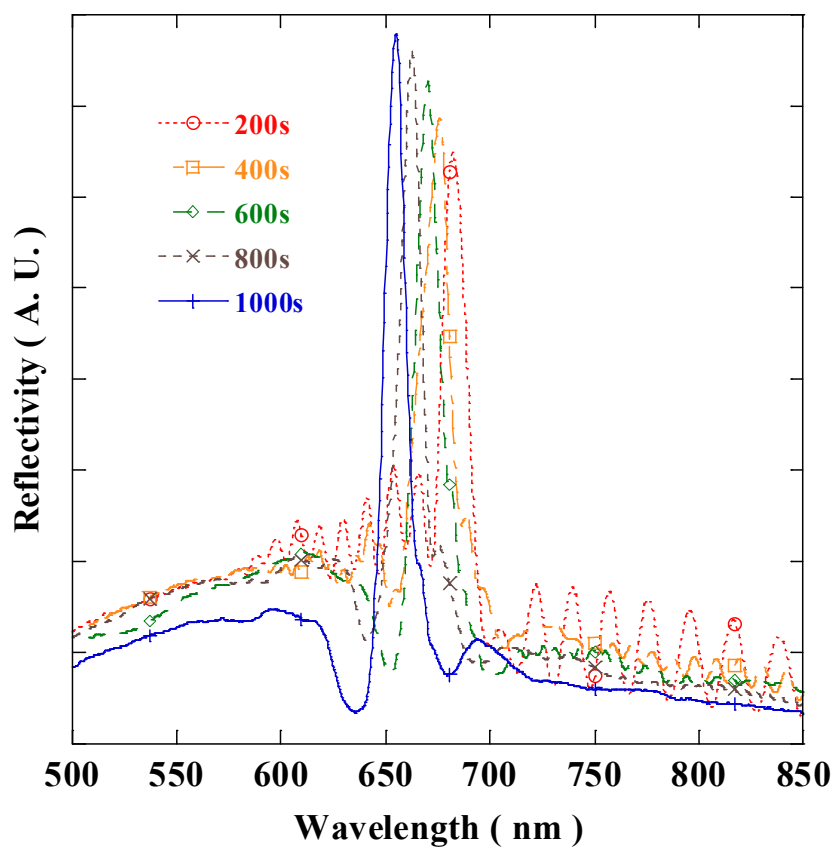
Figure 2.1. The reflection resonances of rugate PS according to etching time from 200 to 400, 600, 800, and 1000 s.

 The relationship among the reflection wavelengths, the relative reflection intensities, and the etching times was summarized in Figure 2. Rugate PS displayed a linear relationship profile between the reflection wavelengths and the etching times. The relative reflection intensities increased linearly as the etching time increased. The relative reflection intensities of rugate PS over 1000 s of etching time start to decrease.
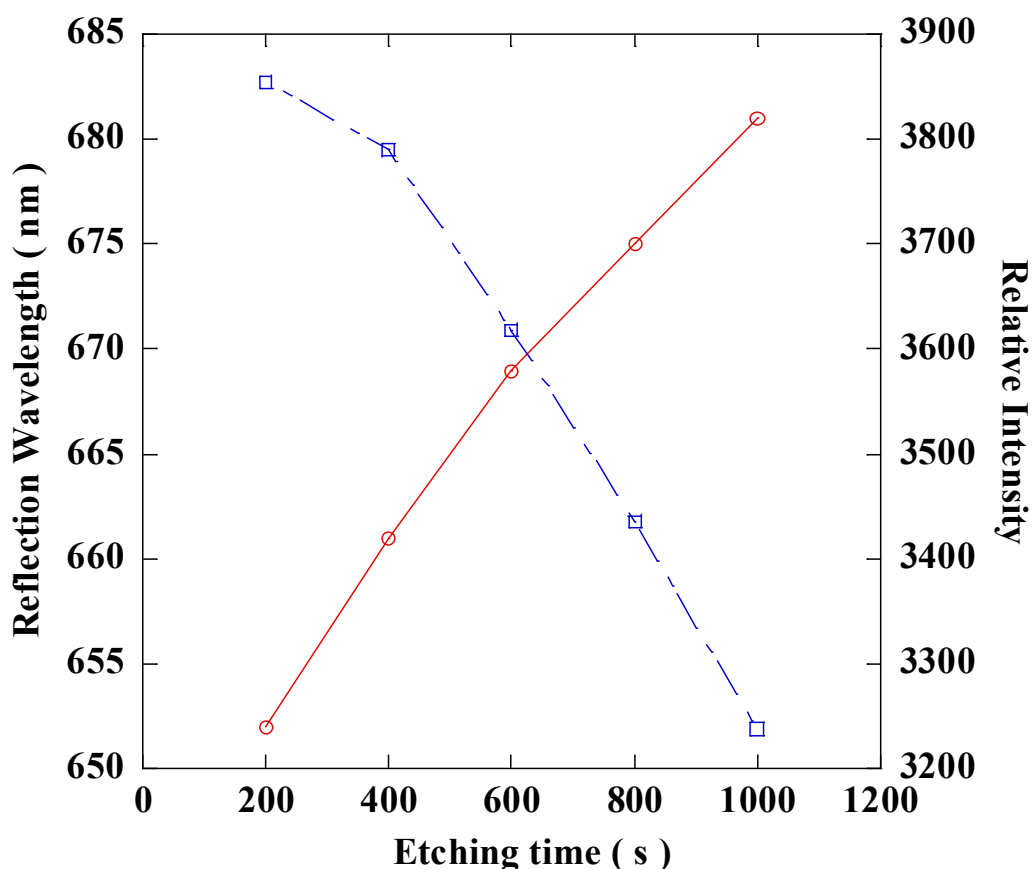
Figure 2.2. Plot showing the relationship among the reflection wavelengths, the reflection intensities, and the etching times.

2.3.2 Effect of Frequency

The effect of frequency for the formation of rugate PS was investigated. All parameters but frequency were fixed. The values of A_i, B, and t were 11.55 and 63.05 mA and 1000 s, respectively. The frequencies, k_i, varied from 0.22 to 0.38 Hz with a spacing of 0.01 Hz between sine components. The reflection band characteristics of 17 rugate PS samples according to the frequency change were listed in Table I.

The relationship between the reflection wavelengths and the frequencies was summarized in Figure 3. Rugate PS exhibited a linear dependence between the reflection wavelengths and the etching frequencies. The reflection band of rugate PS shifted to shorter wavelength by about 13 nm as the etching frequency increased by 0.01 Hz. Their FWHMs of the reflection band varied from 13 to 17 nm.

Figure 4 showed the 3-D reflection stop bands (A) and the photograph of 17 rugate PS samples (B). This result illustrates that the reflection band can be controlled by tuning the etching frequency and appear anywhere in the visible range depending on the sine waveform.

Samples (N)	Value (Hz)	Wavelength (nm)	Δ [N-(N+1)] (nm)	F.W.H.M (nm)
1	0.22	730	14	16.92
2	0.23	716	14	15.14
3	0.24	702	13	16.27
4	0.25	689	14	13.27
5	0.26	675	13	15.4
6	0.27	662	12	16.83
7	0.28	650	14	14.83
8	0.29	636	12	14.57
9	0.30	624	14	13.24
10	0.31	610	14	16.08
11	0.32	596	13	14.05
12	0.33	583	13	15.17
13	0.34	570	12	14.53
14	0.35	557	13	13.51
15	0.36	545	12	12.49
16	0.37	534	11	13.59
17	0.38	522	12	16.88

Table 2.1. Reflection band characteristics of 17 rugate PS samples according to the frequency change.
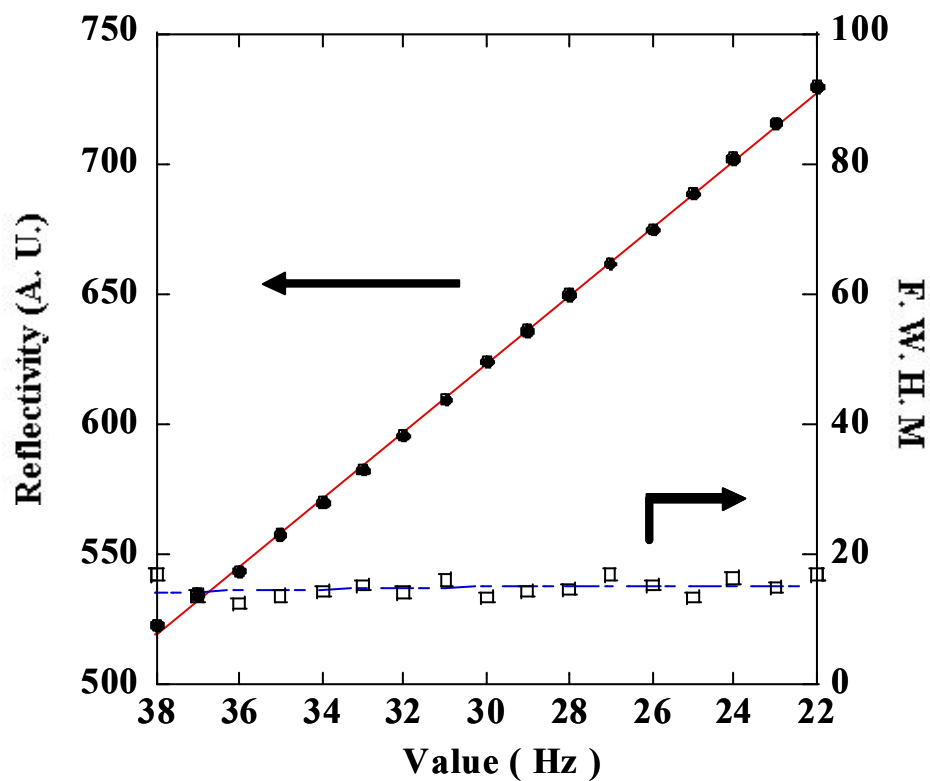
Figure 2.3. Connection of reflection spectra and FWHM about rugate PS samples.
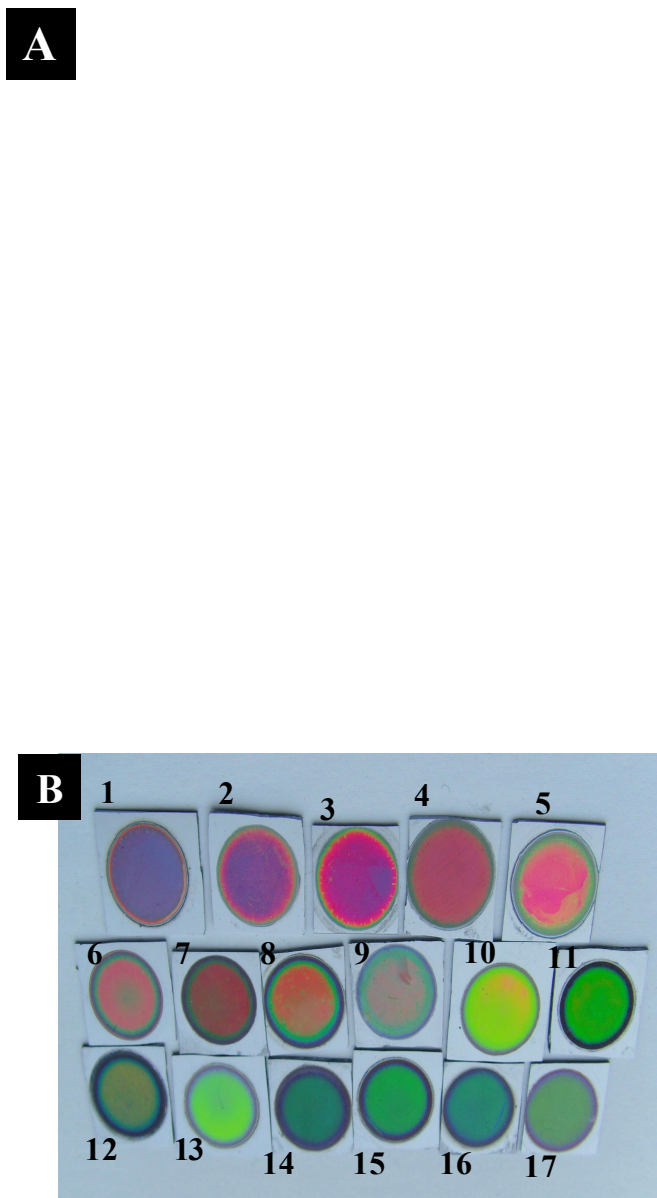
Figure 2.4. Reflection spectra and photograph of 17 rugate PS samples.

2.4 Conclusion

The effect of an etching time for the formation of rugate photonic structure and the effect of a frequency for the reflection band characteristics of rugate PS were investigated. A critical etching time of 200 s was needed to obtain the reflection resonance of rugate PS. The reflection band of rugate PS shifted to shorter wavelength as the etching time increased. Their FWHMs of the reflection band remain the same. The reflection band characteristics of 17 rugate PS samples according to the frequency change were measured. The relationship between the reflection wavelengths and the frequencies was indicated that rugate PS exhibited a linear dependence between the reflection wavelengths and the etching frequencies. The reflection band of rugate PS shifted to shorter wavelength as the etching frequency increased.

2.5 References

[1] V. Wood, M. J. Panzer, J. Chen, M. S. Bradley, J. E. Halpert, M. G. Bawendi, and W. Bulovic *Adv. Mater.* **21**, 2151 (2009).

[2] L. Qu and X. Peng, *J. Am. Chem. Soc.* **124**, 2049 (2002).

[3] H. Sohn, S. L?tant, M. J. Sailor, and W. C. Trogler, *J. Am. Chem. Soc.* **122**, 5399 (2000).

[4] V. S.-Y. Lin, K. Motesharei, K.-P. S. Dancil, M. J. Sailor, and M. R. Ghadiri, *Science* **278**, 840 (1997).

[5] J. Kim, S. Jang, Y. Koh, C. Park, H.-G. Woo, S. Kim, and H. Sohn, *J. Nanosci. Nanotechnol.* **8**, 4951 (2008).

[6] M. A. Khan, M. S. Haque, H. A. Naseem. W. K. Brown, and A. P. Malshe, *Thin Solid Films* **332**, 93 (1998).

[7] S. E. L?tant, S. Content, T. T. Tan, F. Zenhausern, and M. J. Sailor, *Sensor Actuat, B-Chem.* **69**, 193 (2000).

[8] E. J. Anglin, L. Cheng, W. R. Freeman, and M. J. Sailor, *Adv. Drug Deliv. Rev.* **60**, 1266 (2008).

[9] X. G. Zhang, *J. Elecrochem. Soc.* **151**, C69 (2004).

[10] J. Gao, T. Gao, Y. Y. Li, and M. J. Sailor, *Langmuir* **18**, 2229 (2002).

[11] D. Hunkel, R. Butz, R. Ares-Fisher, M. Marso, and H. Lüth *J. Lumines.* **80**, 133 (1999).

[12] M. Haurylau, A. R. Shroff, and P. M. Fauchet *Phys. Stat. Sol. A.* **202**, 1477 (2005).

[13] F. Cunin, T. A. Schmedake, J. R. Link, Y. Y. Li, J. Koh, S. N. Bhatia, and M. J. Sailor, *Nat. Mater.* **1**, 39 (2002).

[14] M. S. Yoon, K. H. Ahn, R. W. Cheung, H. Sohn, J. R. Link, F. Cunin, and M. J. Sailor, *Chem. Commun.* 680 (2003).

[15] S. Kim, C. Park, S. G. Lee, and H. Sohn, *J. Korean Phys. Soc.* **55**, 288 (2009).

Chapter Three
Optical Characterization of Distributed Bragg Reflector Porous Silicon and Band Filter Applications

3.1 Introduction

  In the previous chapter, we have been introduced the fabrication method of rugate PS having a current density of periodic sine waveform. In this chapter, we report the optical characteristics of Distributed Bragg Reflector (DBR) porous silicon (PS). This is another form of multilayers porous silicon with a square waveform. During electrochemical etching of silicon, the density of the generated PS can be continuously varied, making it possible to generate continuously varying refractive index (n) distributions in the direction perpendicular to the plane of the filter. Periodic layers of alternating high index n_1 (thickness t_1) and low index n_2 (thickness t_2) lead to the well known DBR. In the case of a multilayerd structure there is a periodic alternation of two current densities.

  DBR PS displays a plateau of high reflectivity, which can be viewed as 1D photonic band gap, centred at $\lambda_{bragg}= 2 (n_1t_1 + n_2t_2)$ [1]. This resulted in a mirror with high reflectivity in a specific narrow spectral region and displays a very sharp line in the optical reflectivity spectrum. DBR PS has been investigated for a variety of applications, such as chemical sensors [2], microcavity [3,4], and drug delivery [5], due to its high surface area, convenient surface chemistry, and optical signal transduction capability. In this study, we report about fabrication of DBR PS for full color stop band and band filter applications.

3.2 Experiments

DBR PS dielectric mirror first is electrochemically etched into the single Si (100) substrate (boron doped, polished on the (100) face, resistivity of 0.8-1.2 mΩ-cm, Siltronix, Inc.). The electrolyte is made by consists of a 1:3 by volume mixture of absolute ethanol (ACS reagent, Aldrich Chemicals) and aqueous 48% hydrofluoric acid (ACS reagent, Aldrich Chemicals). Etching is carried out in a Teflon cell by using a two-electrode configuration with a Pt mesh counter electrode. DBR PS sample is prepared by using a computer-generated periodic square wave current. The etching condition of silicon wafers were adjusted in a way controlled by tuning of etching time. The resulting free-standing DBR PS film for optical band filter application has been obtained from the silicon substrate by an applying of electropolishing current at 400 mA/cm^2 for 1.5 min in a solution of 48% aqueous HF and ethanol (3:1 by volume), and then at 24 mA/cm^2 for 1.5 min in a solution of 48% aqueous HF and ethanol (1:15 by volume).

The anodization current was supplied by a Keithley 2420 high-precision constant current source which is controlled by a computer to allow the formation of PS multilayers. Optical reflectivity spectra were measured using a tungsten-halogen lamp and an Ocean Optics S2000 CCD spectrometer fitted with a fiber optic input. The reflected light collected at the end of the fiber optic was positioned at the focal plane of the optical microscope. Surface and cross-sectional images of composite films were obtained by using a cold field emission scanning electron microscope (FE-SEM, S-4700, Hitachi).

3.3 Results and Discussion

DBR PS containing two distinct porosities was successfully prepared using a periodic galvanostatic electrochemical etch of crystalline silicon by applying a square wave current between 5 mA/cm^2 and 50 mA/cm^2. A DBR PS exhibits a high reflectivity band with the Bragg wavelength λ_{Bragg}, depending on the thickness of the layers (d_1, d_2) and the corresponding refractive indices (n_1, n_2). The mth order of the Bragg peak is given by:

$$m\,\lambda_{Bragg} = 2(\ d_1 n_1\ +\ d_2 n_2\ ).$$

Etching conditions of etched DBR PS samples are included in Table 1. This interface will have a different roughness at each current change. The important point is now to understand the evolution of the roughness as a function of the DBR PS thickness, when realising DBR layers. The roughness in every layer can just add to one another, or the applied current densities can lead eventually to their own roughness limit. The electrochemical process generates an optically uniform layer of DBR PS. The thickness and porosity of a given layer is controlled by the current density, the duration of the etch cycle, and the composition of the etchant solution. This appear a type of optical reflector that contain a continuous variation of refractive index, along the growth axis. The reflectance spectrum of such a filter shows a high reflectivity "stop band" around a characteristic wavelength. The multilayered photonic crystals of DBR PS exhibit a very sharp line in the optical reflectivity spectrum. This reflective wavelength can be controlled by tuning of etching time and can appear anywhere in the visible range depending on the square waveform. Reflectivity spectra of DBR PS samples are shown in Figure 1.

Number	Wavelength	Low current (time)	High current (time)	FWHM
1	518 nm	60 s	3 s	21
2	536 nm	65 s	3 s	20
3	557 nm	70 s	3 s	24
4	578 nm	75 s	3 s	19
5	589 nm	80 s	3 s	21
6	606 nm	85 s	3 s	22
7	622 nm	90 s	3 s	21
8	635 nm	95 s	3 s	18
9	657 nm	100 s	3 s	23
10	675 nm	80 s	4 s	24
11	692 nm	80 s	5 s	27
12	710 nm	80 s	6 s	24
13	722 nm	80 s	7 s	29
14	735 nm	82 s	7 s	32
15	747 nm	85 s	7 s	26
16	759 nm	90 s	7 s	30

Table 3.1. Etching conditions and reflection peak of DBR PS samples.

Figure 3.1. Reflection wavelength of DBR PS samples.
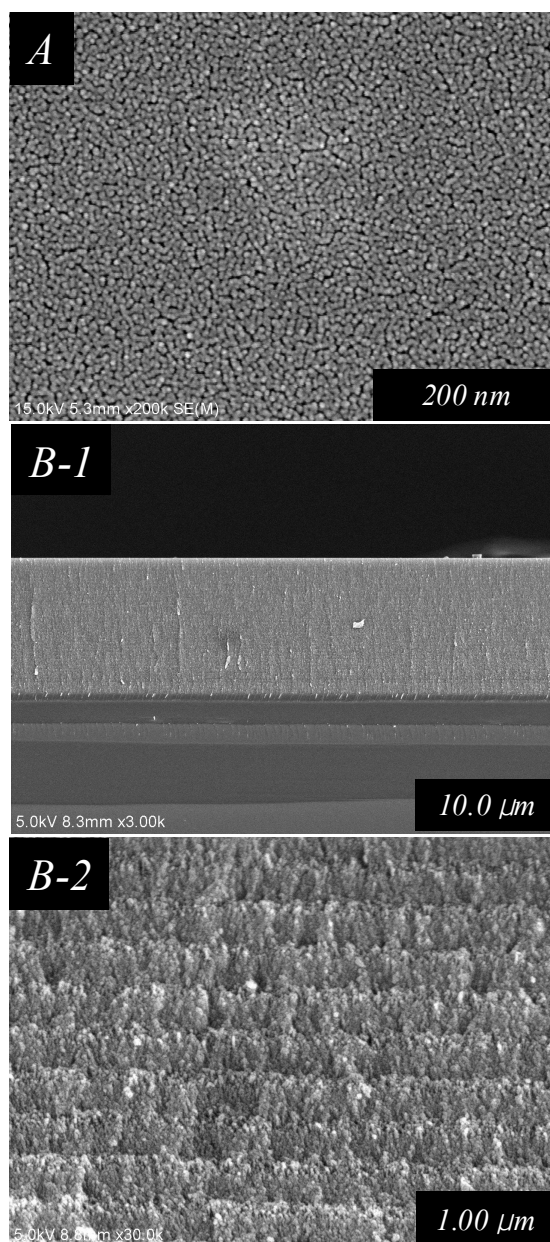
Figure 3.2. Surface (A) and cross-sectional (B-1,2) FE-SEM images of DBR PS.

Reflectivity spectra shown in Figure 1 indicates that the FWHM of these reflection bands is much narrower than that of fluorescence spectrum obtained from a fluorescent organic molecules or quantum dot. The reflection bands of DBR PS samples shown in Figure 1 have a FWHM of 20-30 nm. Location of reflection bands are appeared that shifted to longer wavelengths as increase etching time of current.

The cross-sectional and surface SEM image of DBR PS shown in Figure 2 illustrates that the multilayer of DBR PS exhibits a depth of few microns and a pore of few nano applying of square current density during the etching process results two distinct refractive indices in the contrast. The cross-sectional SEM image of DBR PS shown in Figure 2 (B-2) can observe two different PS layers.

DBR PS films have been removed from the silicon wafer by applying an electropolishing current. Reflectivity spectra of DBR PS and free-standing DBR PS film is shown in Figure 3 (A). The reflectivity of free-standing DBR PS film occurs at the identical location. Also, photographs showed in Figure 3 (B) exhibit electropolished free-standing DBR PS film.

In a basic demonstration for optical filter application, the reflection and transmission spectra of free-standing DBR PS film were shown in Figure 4 (A). Also, when the two free-standing DBR films overlap, transmission spectrum was superimposed.
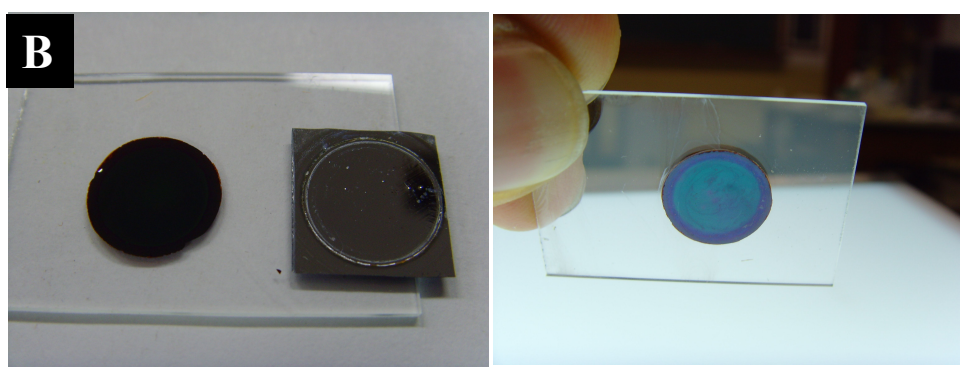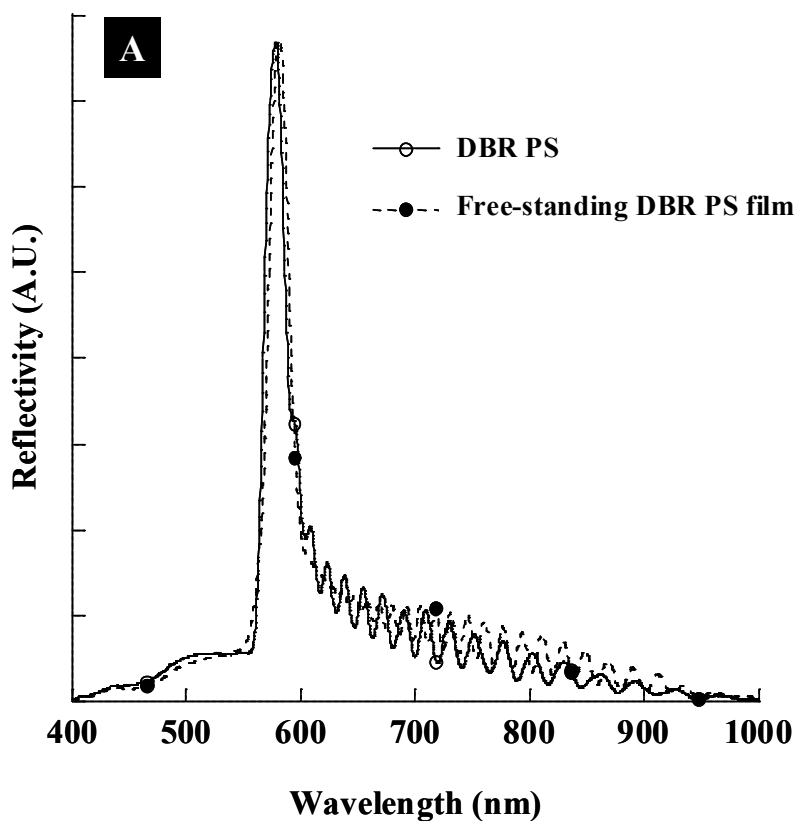
Figure 3.3. Reflection spectra (A) and photograph (B) of free-standing DBR PS
film.
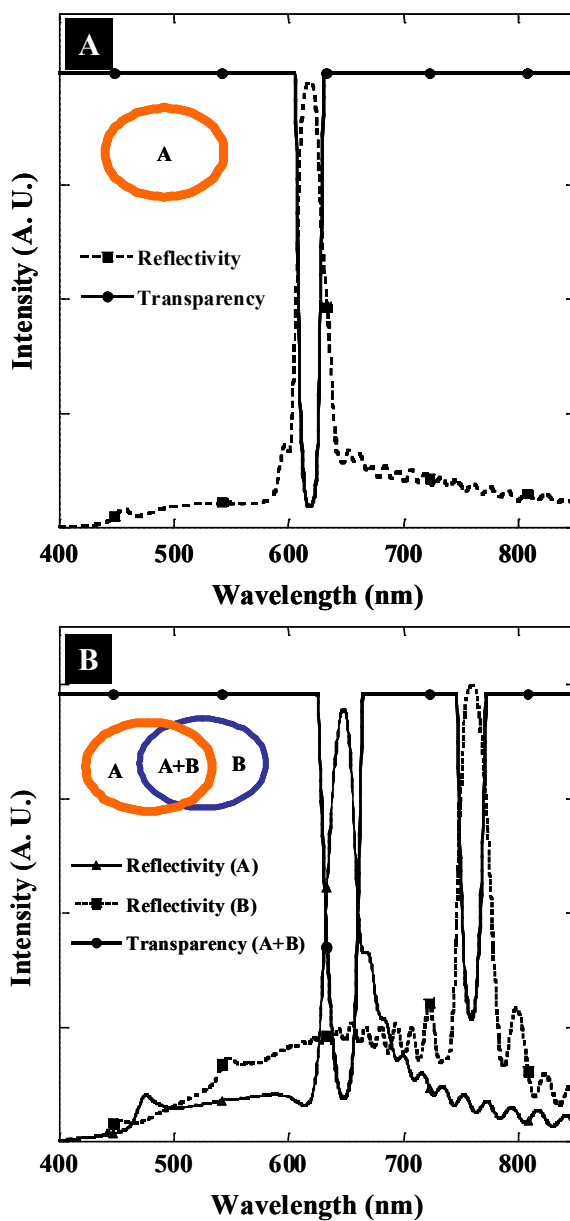
Figure 3.4. Optical filter application using transparency of DBR PS film.

3.4 Conclusion

DBR PS was prepared for the possible use of full-color reflector or filter. DBR PS exhibiting unique reflectivity was successfully obtained by an electrochemical etching of silicon wafer using square current waveform. The multilayered photonic crystals of DBR PS exhibited the reflection of a specific wavelength with high reflectivity in the optical reflectivity spectrum. This reflective wavelength can be controlled by tuning of etching time and can appear anywhere in the visible range depending on the square waveform. This might be a demonstration for the fabrication of specific reflectors or filters in full color.

3.5 References

[1] S. Ilyas, T. Böcking, K. Kilian, P. J. Reece, J. Gooding, K. Gaus, and M. Gal, *Opt. Mater.* **29**, 612 (2007).

[2] S. G. Kim, S. Kim, Y. C. Ko, S. Cho, and H. Sohn, *Colloid Surf. A-Physicochem. Eng. Asp.* **314**, 398 (2008).

[3] S. Chan, S. R. Horner, P. M. Fauchet, and B. L. Miller, *J. Am. Chem. Soc.* **123**, 11797 (2001).

[4] L. Pavesi, C. Mazzoleni, A. Tredicucci, and V. Pellegrini, *Appl. Phys, Lett.* **67**, 3280 (1995).

[5] Y. Koh, S. Jang, J. Kim, S. Kim, Y. C. Ko, S. Cho, and H. Sohn, *Colloid Surf. A-Physicochem. Eng. Asp.* **314**, 328 (2008).

Chapter Four

Fabrication and Characterization of Prismatic Band Filter Gradient Rugate Porous Silicon

4.1 Introduction

The development of a new technology to build one-dimensional photonic structures is of great interest because they are too complex to fabricate by using conventional lithographic methods. PS is an attractive material for photonic applications due to its high surface area, open pore structure, and optical signal transduction capability. A variety of passive devices, such as mirrors [1], filters [2], and microcavities [3,4], has already been employed by using PS which is based on a relatively simple electrochemical etching process. The first reports giving details of a new form of silicon appeared in 1956 when Uhlir described a study of the electropolishing of silicon in hydrofluoric acid [5]. Research on PS has been increased significantly since the discovery of efficient visible luminescence of PS by Canham suggesting the possibility of silicon based light sources [6].

One-dimensional photonic crystals of PS have also found application in chemical detection [7,8], remote sensing [9], and biomolecular screening [10]. PS is a nano-crystalline material that is generated by etching of bulk crystalline silicon in aqueous hydrofluoric acid (HF) [11]. Molpology and optical properties of PS are dependent on HF concentration, dopant type, density in the Si substrate, and applied current density [12,13]. Porous silicons containing gradient refractive index

have been recently developed [14,15]. The direction of the refractive index gradient is perpendicular to the optical. Here we report the optical characteristics and morphology of BFG rugate PS whose appearance is prismatic due to gradient refractive index. This is achieved by various porosity and depth of PS during the electrochemical fabrication process.

4.2 Experiments

4.2.1 Preparation of ruagte PS using asymmetric electrode configuration

BFG rugate PS dielectric mirror was prepared by using electrochemical etching of silicon wafer (boron doped, polished on the (100) face, resistivity of 0.8-1.2 m Ω-cm, Siltronix, Inc.), and using a computer-generated periodic sine wave current. The etching solution consists of a 1:3 by volume mixture of absolute ethanol (ACS reagent, Aldrich Chemicals) and aqueous 48% hydrofluoric acid (ACS reagent, Aldrich Chemicals). Etching is carried out in a Teflon cell by using a two-electrode configuration with Pt needle counter electrode. BFG rugate PS containing a distribution of pore sizes and film thickness was prepared by using the asymmetric electrode configuration as shown in Scheme 1.

4.2.2 Instrumentation and Data Acquisition

The anodization current was supplied by Keithley 2420 high-precision constant current source which is controlled by a computer to allow the formation of PS multilayers. Optical reflectivity spectra were measured using a tungsten-halogen lamp and an Ocean Optics S2000 CCD spectrometer fitted with a fiber optic input. The reflected light collection end of the fiber optic was positioned at the focal plane of the optical microscope. Scanning electron microscope (SEM) images were obtained by a cold field emission scanning electron microscope (FE-SEM, S-4700, Hitachi).
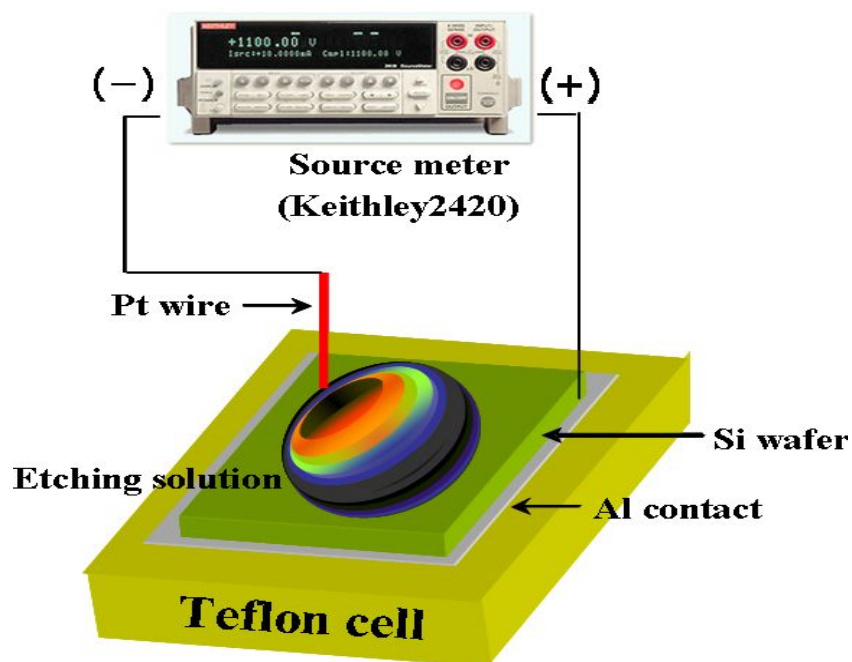
Scheme 4.1. Schematic diagram of the electrochemical cell and electrode arrangement used to generate pore gradients.

4.3 Results and Discussion

BFG rugate PS has been generated by an electrochemical etching of silicon wafer using an asymmetric electrode configuration in aqueous ethanolic HF solution. BFG PS prepared by using anisotropic etching conditions displays the anisotropic reflection bands whose reflection maximum varied spatially across the porous silicon. The waveform used in the present work, which is represented by Equation 1.

$$\mathbf{y}_i = A_i \left[\sin \left(k_i t \right) \right] + \boldsymbol{B} \quad \text{--------------} \quad (1)$$

Where y_i represents a temporal sine wave of amplitude, A_i ; frequency, k_i ; time, t ; applied current density, B. The values of k_i are from 0.39 Hz. The values of A_i and $\boldsymbol{B}$ are 11.55 and 63.05 mA with 205 repeats.

To have anisotropic distribution of pore sizes and film thickness in PS, Pt needle electrode is placed at the side of etching cell and Al plate electrode is located at the back side of the silicon wafer as shown in Scheme 1. With this asymmetric electrode arrangement, the porosity and the thickness of the film at any point depend on the magnitude of the etching current flowing through that point. The current at any point of silicon wafer depends on the resistance of the Si wafer between the electrolyte on one side and the Al plate electrode on the back side and varies as a function of distance from the Pt counter electrode due to solution resistance. Since the geometry is asymmetric, the current density decreases as the distance from the counter electrode increases. The asymmetric electrode configuration provides a current density gradient across the wafer that result in a distinct variation in the morphology of the pores and produces a BFG PS lens

showing asymmetric Newton's ring. Photograph and reflection spectra of BFG rugate PS are shown in Fig 1. The reflection spectra of BFG rugate PS are recorded by moving every 2 mm from the position closest to the Pt counter electrode on the silicon surface.
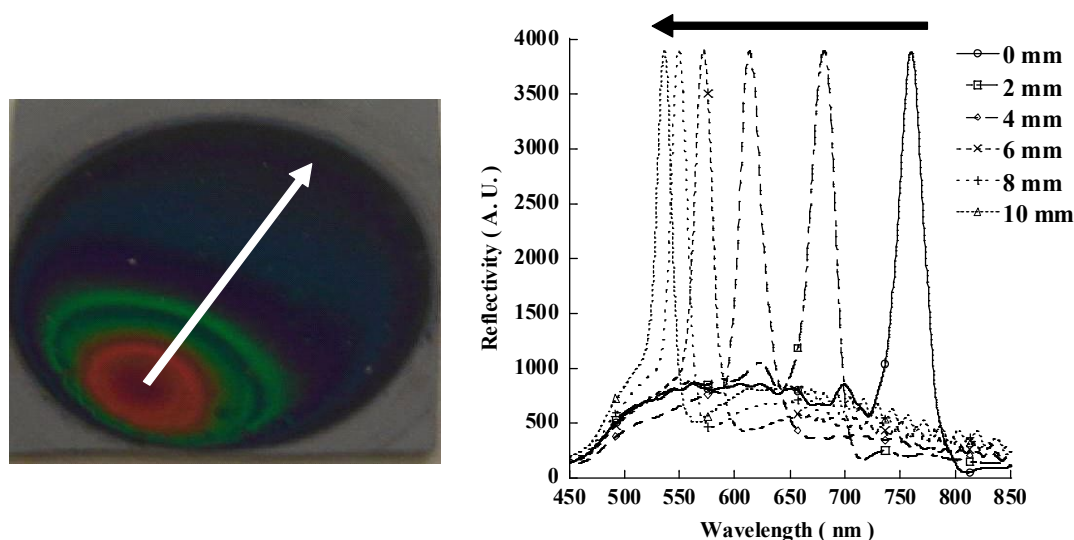
Figure 4.1. Photograph and reflection spectra of BFG rugate PS. The value position used refers to the distance from the position closest to the Pt counter electrode across the silicon wafer.

X	λ	$\Delta \lambda$[n-(n+1)]	F.W.H.M
(mm)	(nm)	(nm)	(nm)
0	759	0	28.78
2	680	79	27.67
4	612	68	25.15
6	569	43	23.37
8	548	21	19.89
10	535	13	18.25

Table 4.1. Data analysis of BFG rugate PS about the position of electrode.

Changes of reflective maxima and FWHM are summarized in Table 1. The reflection wavelength shifts exponentially to shorter wavelengths and FWHM is narrower across the silicon wafer. The BFG rugate PS displays a prismatic appearance due to the continuously changing refractive index distribution.

The cross-section and surface SEM image of BFG rugate PS are shown in Figure 2. The film thickness of BFG rugate PS becomes shorter as the distance from the position of Pt counter electrode increases.

Profilometry measurements shown in Figure 3 reveal that the thickness of the PS layer varies as a function of distance from the counter electrode. BFG rugate PS is thickest at the point directly under the counter electrode, consistent with that being the position of highest current density.
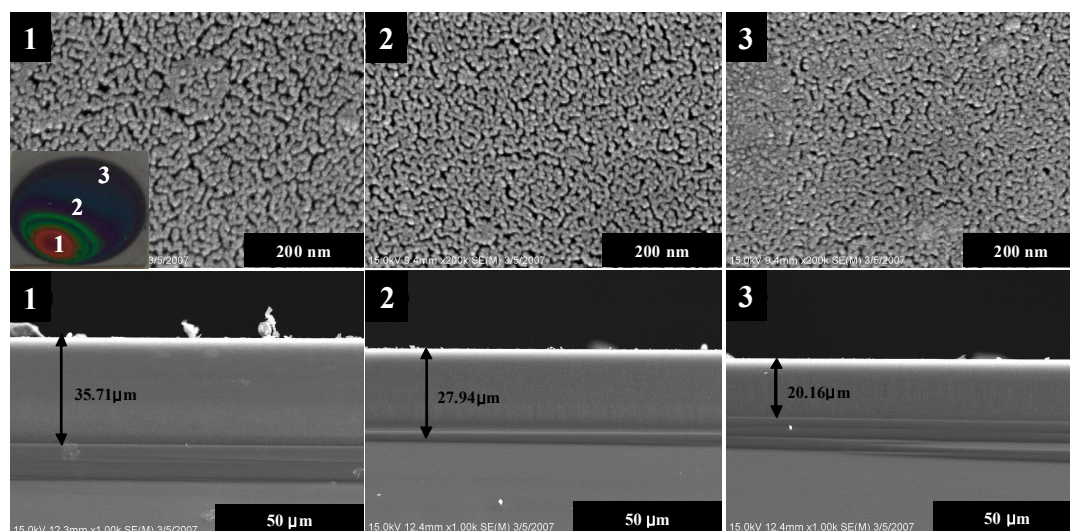
Figure 4.2. Surface and cross-section SEM images of BFG rugate PS. 0 mm (1), 5 mm (2), and 10 mm (3) refer to the distance from the position closest to the Pt counter electrode across the silicon wafer.
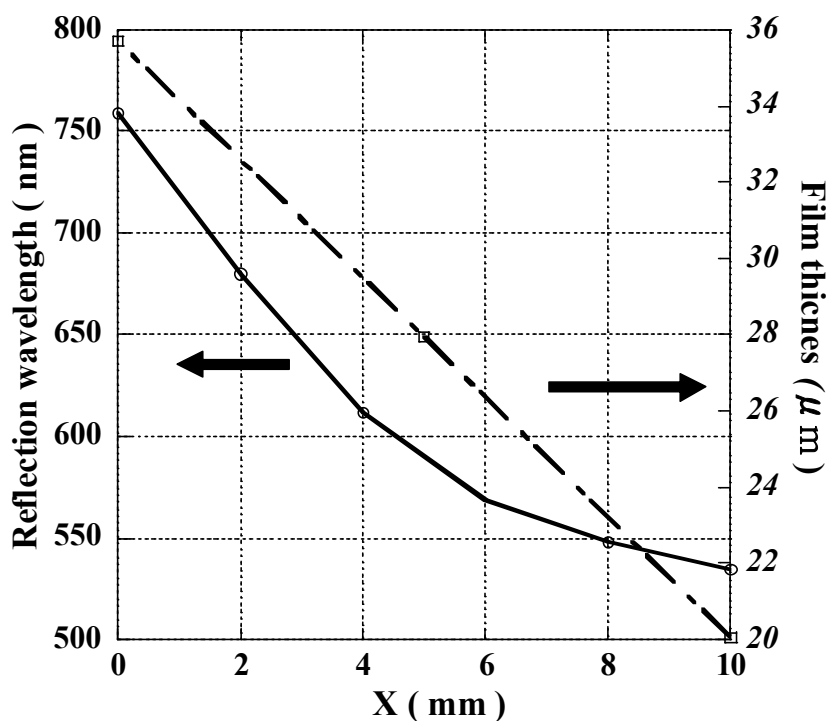
Figure 4.3. Profile of the change of reflection wavelength and film thickness of BFG rugate PS as a function of x represented to the distance from the position closest to the Pt counter electrode across the silicon wafer.

4.4 Conclusion

BFG rugate PS was prepared that contain a controlled distribution of pore sizes and film thickness using anisotropic etching conditions. In this work, BFG rugate PS displays a prismatic appearance due to the uneven distribution of current across the silicon wafer during the etching. The reflectivity of BFG rugate PS is shifted to shorter wavelengths and its bandwidth and film thickness become narrower and shorter across the wafer from the position of electrode. This might be a demonstration for the fabrication of specific reflectors or filters.

4.5 References

[1] W. H. Zheng, P. J. Reece, B. Q. Sun, and M. Gal, *Appl. Phys. Lett.* **84**, 3519 (2004).

[2] M. G. Berger, F. Arens-Fischer, M. Thönissen, M. Krüger, S. Billat, H. Lüth, S. Hilbrich, TW. heiβ, and P. Grosse, *Thin Solid Films* **297**, 237 (1997).

[3] S. Chan and P. M. Fauchet, *Opt. Mater.* **17**, 31 (2001).

[4] M. Ghulinyan, C. J. Oton, G. Bonetti, Z. Gaburro, and L. J. Pavesi, *J. Appl. Phys.* **93**, 9724 (2003).

[5] A. Uhlir, *Bell System Tech.* **35**, 333 (1956).

[6] L. T. Canham, *Appl. Phys. Lett.* **57**, 1046 (1990).

[7] H. Sohn, S. Letant, M. J. Sailor, and W. C. Trogler, *J. Am. Chem. Soc.* **122**, 5399 (2000).

[8] J. Gao, T. Cao, Y. Y. Li, and M. J. Sailor, *Langmuir* **18**, 2229 (2002).

[9] T. A. Schmedake, F. Cunin, J. R. Link, and M. J. Sailor, *Adv. Mater.* **14**, 1270 (2002).

[10] F. Cunin, T. A. Schmedake, J. R. Link, Y. Y. Li, J. Koh, S. N. Bhatia, and M. J. Sailor, *Nature Mater.* **1**, 39 (2002).

[11] H. Foll, J. Carstensen, M. Christophersen, and G. Hasse, *Phys. Status Solidi A* **182**, 7 (2000).

[12] K.-P. Dancil, S. D. P. Greiner, and M. J. Sailor, *J. Am. Chem. Soc.* **121**, 7925 (1999).

[13] S. Chan, P. M. Fauchet, Y. Li, L. J. Rothberh, and B. L. Miller, *Phys. Status Solidi A* **182**, 541 (2000).

[14] S. Ilyas and M. Gal, *Appl. Phys. Lett.* **89**, 211123 (2006).

[15] B. E. Collins, K.-P. S. Dancil, G. Abbi, and M. J. Sailor, *Adv. Funct. Mater.* **12**, 187 (2002).

Chapter Five

Fabrication of Multi-optical Filters Based on Encoded Rugate Porous Silicon and Its Application as Chemical Sensors

5.1 Introduction

Photonic crystals have been extensively studied in recent years because of their unique optical properties and the possibility of modulating the spectral resonance of optical spectrum. The development of a new technology to build a photonic structure is of great interest because it could be useful for a variety of applications such as chemical and biological sensors [1] or medical diagnostics [2,3]. Since the discovery of porous silicon (PS) from silicon wafer, research has been associated with emerging technologies, such as photonic crystals for optical band pass filters and micro chemical reaction applications in micro chemical reactors [4,5]. Their importance is due to biocompatibility [6] and bioresorbability [7]. In addition, PS has tunable pore sizes and volumes [8], high surface area [9], and optical signal transduction capability. In recent years, several possible applications for PS have been actively investigated [10]. Electrochemical etch is one of the powerful tools to provide a reflection band at a desired wavelength in the optical reflectivity spectrum. Multiple rugate filters were recently developed by applying a computer-generated pseudo-sinusoidal composite current-time waveform [11,12]. The refractive index varied sinusoidally in a photonic structure of rugate-structured PS.

However, rugate PS was limited about its chemical and mechanical stability for many applications because a free-standing film was very brittle [13]. To eliminate these issues, several researches have been recently investigated [14].

Here we have prepared a flexible rugate PS/polymer composite film containing a nanostructure with the complex photonic properties. Possible applications of these composite films such as tunable band-rejection filters and chemical sensors were reported.

5.2 Experiments

5.2.1 Preparation of multiple rugate PS

PS samples were prepared by electrochemical etch of heavily doped p^{++}-type silicon wafers (boron doped, polished on the <100> face, resistivity of 0.8 - 1.2 mΩ·cm, Siltronix, Inc.). The etching solution consisted of a 3:1 volume mixture of aqueous 48% hydrofluoric acid (ACS reagent, Aldrich Chemicals) and absolute ethanol (ACS reagent, Aldrich Chemicals). Galvanostatic etch was carried out in a Teflon cell by using a two-electrode configuration with a Pt mesh electrode. A sinusoidal current density waveform varying between 51.5 and 74.6 mA/cm^2 was applied. The anodization current was supplied by a Keithley 2420 high-precision constant current source which was controlled by a computer to allow the formation of PS multilayers. To prevent the photogeneration of carriers, the anodization was performed in the dark. All samples were then rinsed several times with ethanol and dried under Ar atmosphere prior to use.

5.2.2 Chemical modification of rugate PS film surface

The resulting rugate PS films were removed from the silicon substrate by an applying of electropolishing current at 380 mA/cm^2 for 2 min in a solution of 48% aqueous HF and ethanol (3:1 by volume), and then at 24 mA/cm^2 for 3 min in a solution of 48% aqueous HF and ethanol (1:15 by volume) to obtain a free-standing rugate PS. Three types of rugate PS film were prepared in this study. (1) Freshly etched rugate PS film was stored under argon atmosphere prior to use.

(2) Dodecyl-derivatized rugate PS film was prepared by the hydrosilation. Freshly etched rugate PS film was placed on quartz tube reactor in glove box under argon atmosphere. After 20 mL of 1-dodecene (ACS reagent, Aldrich Chemicals) was added, the reaction mixtures were irradiated under UV lamp (λem = 360 nm) for 10 h. Dodecyl-derivatized rugate PS film was rinsed several times with acetone and dried under argon at room temperature. (3) Oxidized rugate PS film was prepared by the thermal oxidation. Rugate PS film was thermally oxidized by using an electric muffle furnace at 300 ℃ for 3 h in ambient air condition and then allowed to cool to room temperature.

5.2.3 Preparation of multiple rugate PS/polymer composite film

In a typical preparation for the rugate PS/polystyrene composite film, 5 g of polystyrene (Aldrich, Mw = 280,000) were dissolved in 20 mL of THF (Fisher Scientific). The free-standing films were placed on 0.5 mL of polystyrene solution, pipeted onto the cover glass. The composite materials were dried to remove volatiles at room temperature for 1 h. After dryness, the composite films were peeled off from the cover glass.

5.2.4 Instrumentation and Data Acquisition

Optical reflectivity spectra were measured using a tungsten-halogen lamp and an Ocean Optics S2000 CCD spectrometer fitted with a fiber optic input. Surface and cross-sectional images of composite films were obtained by using a cold field emission scanning electron microscope (FE-SEM, S-4800, Hitachi). The surface properties of rugate PS were characterized by FT-IR instrument (Nicolet 5700).

5.3 Results and Discussion

5.3.1 Preparation and characterization of multi-optical rugate filter

Photonic crystals containing rugate structure resulted in a mirror with high reflectivity in a specific narrow spectral region. Multiple rugate PS were prepared by applying a computer-generated that the individual sine components were summed together to create a composite waveform. This reflection resonance could be tuned to appear anywhere in the visible to near-infrared spectral range, depending on the programmed etch waveform. The waveform used in the present work, which was represented by Equation 1.

$$ y_{comp} = A_1\sin(k_1t) + A_2\sin(k_2t) + ... + A_n\sin(k_it) + B \quad (1) $$

Where y_i represented a temporal sine wave of amplitude, A_i; frequency, k_i; time, t; applied current density, B. Equation 1, containing all the encoding information, can be converted to an analog current-time waveform for etching by using a computer-controlled digital galvanostat.

Multiple rugate structures were generated by using different parameters in Equation 1 and displayed the corresponding reflection resonances as shown in Figure 1. The values of A_i and B for every sine components were 11.55 and 63.05 mA, respectively. A composite waveform containing one to four frequency components was used. The values of k_i for each of the sine components varied from 0.38 to 0.44 Hz, with a spacing of 0.02 Hz between each sine component. Multiple encoded rugate PS etched with 0.44, 0.42, 0.40, and 0.38 Hz exhibited four sharp lines at 610, 660, 715, and 785 nm, respectively. Each of the main

peaks in the optical reflectivity spectrum was superimposed over each peak and corresponded to one of the sine components of the composite waveform, indicating that the reflectivity spectrum represented the Fourier transform of the composite current-time waveform.
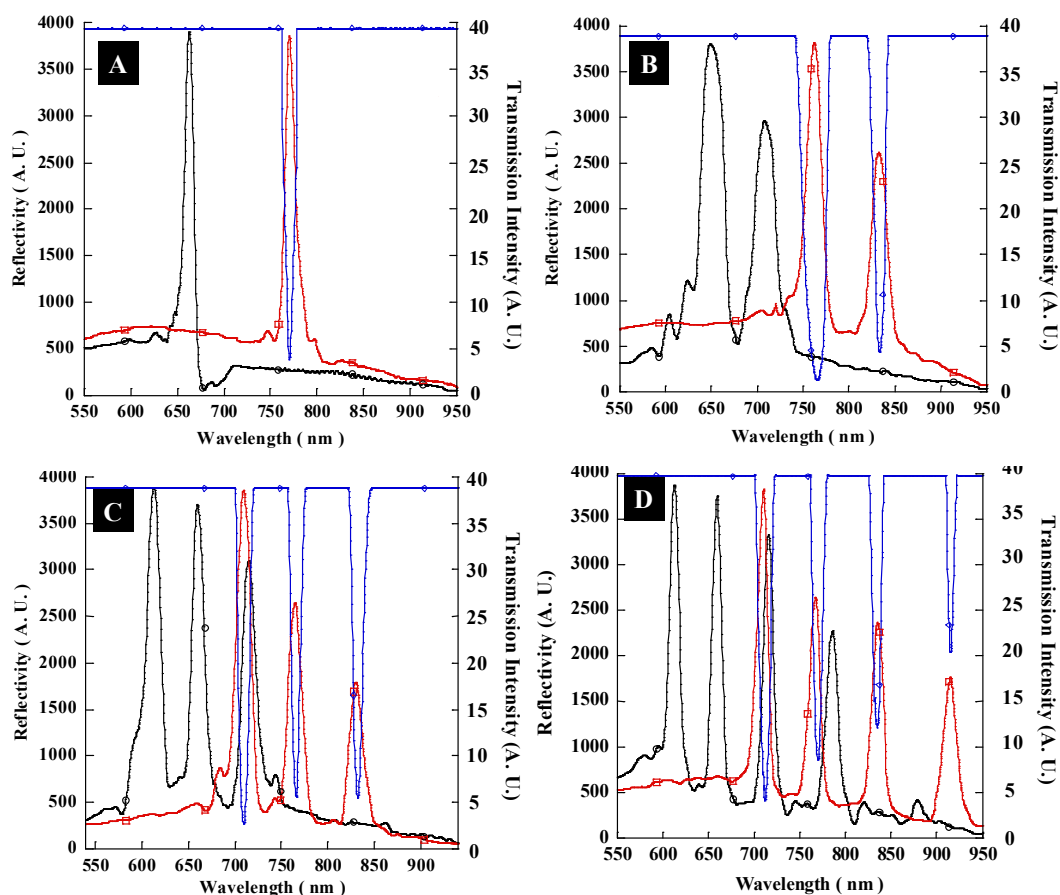
Figure 5.1. Reflection spectra of fresh rugate PS (black) and composite film (red) and transmission spectra of composite film (blue). The values of k_i for each of the sine components are (A) 0.42 Hz, (B) 0.40 and 0.42 Hz, (C) 0.40, 0.42, and 0.44 Hz, (D) 0.38, 0.40, 0.42, and 0.44 Hz. Reflection maxima of fresh rugate PS and composite film are 610, 660, 715, and 785 nm and 710, 760, 830, and 915 nm, respectively.

After the generation of optically encoded rugate PS, the resulting PS films were removed from the silicon substrate by applying an electropolishing current to obtain a free-standing rugate PS film. A pulse of current was sufficient to undercut the PS layer and lift it completely from the silicon substrate. Free-standing PS films were typically very brittle and shatter when subjected to minor shear stresses. After lift-off, the free-standing film was placed on a small drop of polystyrene mixture layered on top of the cover glass. Dryness at room temperature for 1 h produced a robust and stable composite material in which the PS matrix was covered with polystyrene. The composite films shown in Figures 2A and 2B were highly flexible at room temperature. Their mechanical stability improved significantly without apparent degradation in their optical reflection properties upon flexing. Reflection and transmission spectra of multiple encoded rugate PS/polystyrene composite films were shown in Figure 1. Multiple encoded composite films displayed four sharp resonances at 710, 760, 830, and 915 nm in the reflection and transmission spectra, respectively. The transmission resonances were located in the same physical locations placed the reflection resonance in the optical reflectivity spectrum. The reflection resonances of the composite films were shifted to longer wavelengths by 100 - 125 nm upon introduction of the polymer into the pores. Such a large red shift was the characteristic features of an increase in the average refractive index of the multilayer which was consistent with the replacement of a significant amount of empty pore volume with the polymers.

Surface and cross-sectional SEM image of optical filter were shown in Figure 2. The cross-sectional image of rugate PS etched with 0.42 Hz in Figure 2D illustrated that the rugate PS had a gradually modulated refractive index profile. The rugate PS exhibited a porosity depth profile that related directly to the current-time profile used in etch. They possessed a sinusoidally varying porosity

gradient in the direction perpendicular to the plane of the filter. Cross-sectional SEM image of multiple encoded rugate PS/polystyrene composite films etched with composite waveform were shown in Figure 2E and 2F, indicating that the PS layer and polymer layer exhibited a depth of 46.5 and 56.3 microns, respectively.
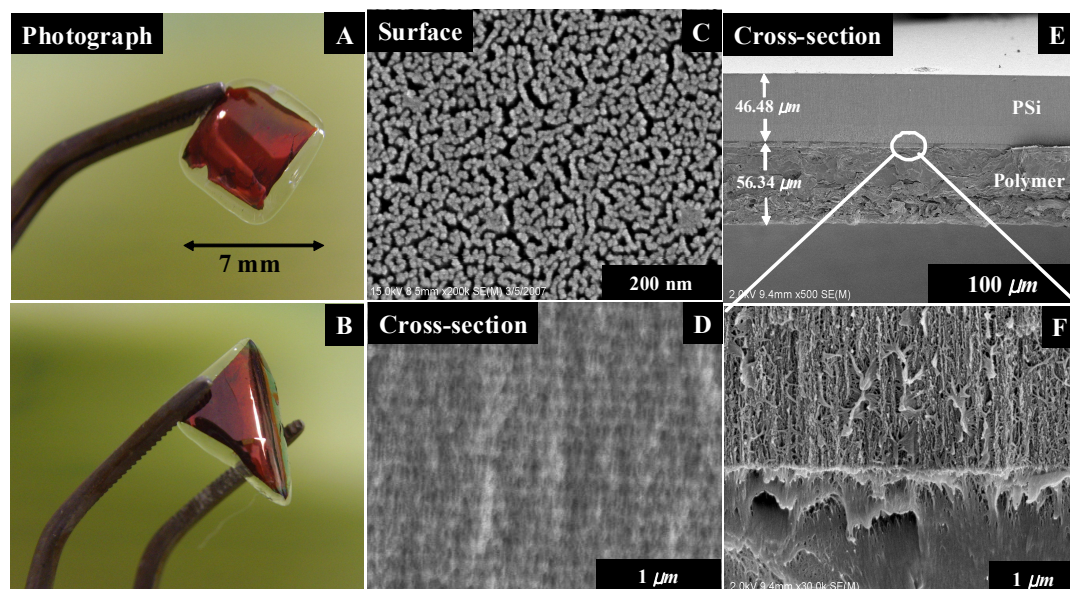
Figure 5.2. Photographs and FE-SEM images of rugate PS/polymer composite films.

5.3.2 Rugate PS/polymer composite film as a tunable band-rejection filter

The transmission spectrum of triple rugate PS/polymer composite film was shown in Figure 3 and displayed three sharp transmission resonances at 715, 776, and 849 nm. This composite film could be used as a tunable band-rejection filter upon exposing to the organic vapor. Transmission spectrum shown in Figure 3A illustrated that the transmission resonances were shifted to the longer wavelength due to an increase in the refractive indices of the porous medium, when the composite film was exposed to the air-saturated vapor of methanol (vapor pressure, 97.48 mmHg) and hexane (121.26 mmHg). The red-shifts of the first to third transmission resonances were 17, 19, and 24 nm in methanol and 51, 57, and 64 nm in hexane, respectively. Figure 3B displayed the shift of transmission resonances under the different vapor pressures of methanol. This result indicated that the transmission resonance was tunable by the control of a medium dose.
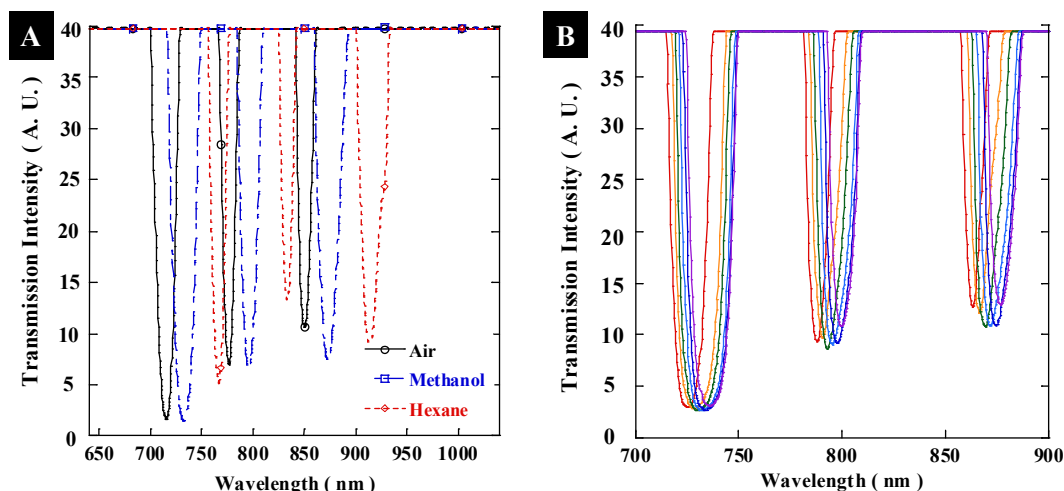
Figure 5.3. (A) Transmission resonance spectra under exposure to different media such as hexane (766, 833 and 913 nm) and methanol (732, 795 and 873 nm). (B) Transmission resonance spectra under different vapor pressures of methanol. The values of vapor pressure for each of the transmission spectrum are varied from 0 to 97.5 ppm, with a spacing of about 16 ppm between each spectrum.

5.3.3 Rugate PS/polymer composite films as chemical sensors

To know the responsibility of transmission resonance for the organic vapors, two different types of triple encoded rugate PS composite films were prepared by the modification of rugate PS surface. The PS composite films prepared by the thermal oxidation were hydrophilic materials due to the hydroxyl functionalities. The PS composite films prepared by the photolytic hydrosilation were hydrophobic materials because of the dodecyl functionalities. These samples had the different physical surface properties. The surface of rugate PS was characterized by FT-IR

measurement and shown in Figure 4. FT-IR spectrum of fresh rugate PS film displayed vibrational bands in the fingerprint region of the spectrum. υ(Si-H) and δ(Si-H) vibrations associated with surface Si-H species were observed at 2117 and 941 cm^{-1}, respectively. The oxidized form of rugate PS displayed the band characteristics of υ(OSi-H) and υ(Si-O) vibrational modes at 2270 and 1070 cm^{-1}, respectively. Rugate PS modified with 1-dodecene displayed the absorption band characteristic of the dodecyl group with vibrations assigned to C-H stretching modes at 2850-2960 cm^{-1}.
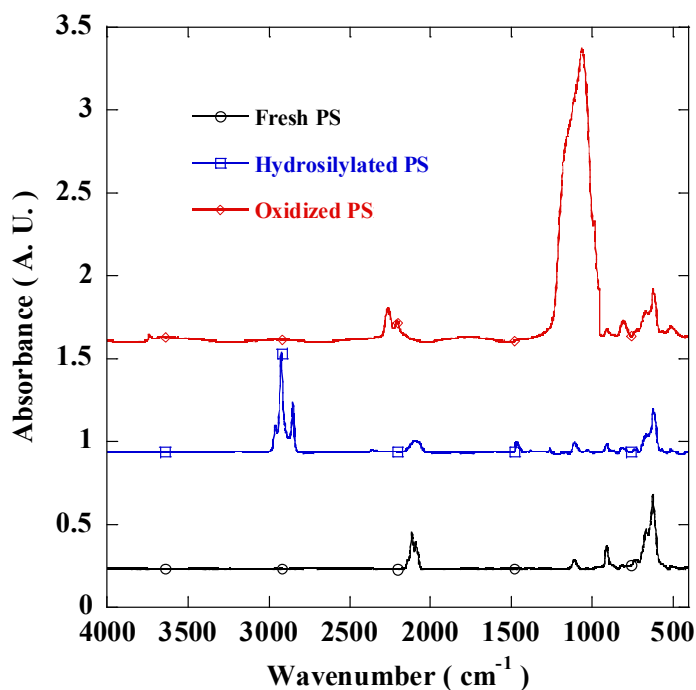
Figure 5.4. FT-IR spectra of fresh, dodecyl modified, and oxidized rugate PS.

The transmission spectra of hydroxyl and dodecyl terminated rugate PS composite films were shown in Figures 5A and 5B, respectively. Triple encoded rugate PS composite samples were placed in an exposure chamber fitted with an optical

window. The composite films were exposed to a flux of methanol or hexane in air with a flow rate of 5 L/min. Figure 5 showed the transmission spectra of composite films with three transmission bands while exposing to organic vapors. The transmission spectra from the composite films for the detection of volatile organic compounds were recorded just after exposure to the air-saturated vapor of each analyte. With the hydroxyl terminated composite films, capillary condensation caused three transmission bands to shift to longer wavelengths by 14, 16, and 23 nm for the first to third transmission bands under exposure to methanol vapor. However, little red shifts of transmission resonances were obtained with the dodecyl terminated composite films. The shifts of transmission resonances of triple encoded rugate PS composite film depended on both the surface functionalities of composite films and the properties of dose media. Composite films modified with dodecyl functionality were a porous hydrophobic material and had a much greater affinity for hydrophobic versus hydrophilic media, since the adsorption depended on the surface property of the composite films. However, the rugate PS modified with hydroxyl group had a greater affinity for hydrophilic media. This result indicated that the specificity of adsorption or capillary condensation at the PS surfaces depended dramatically on the surface chemistry.
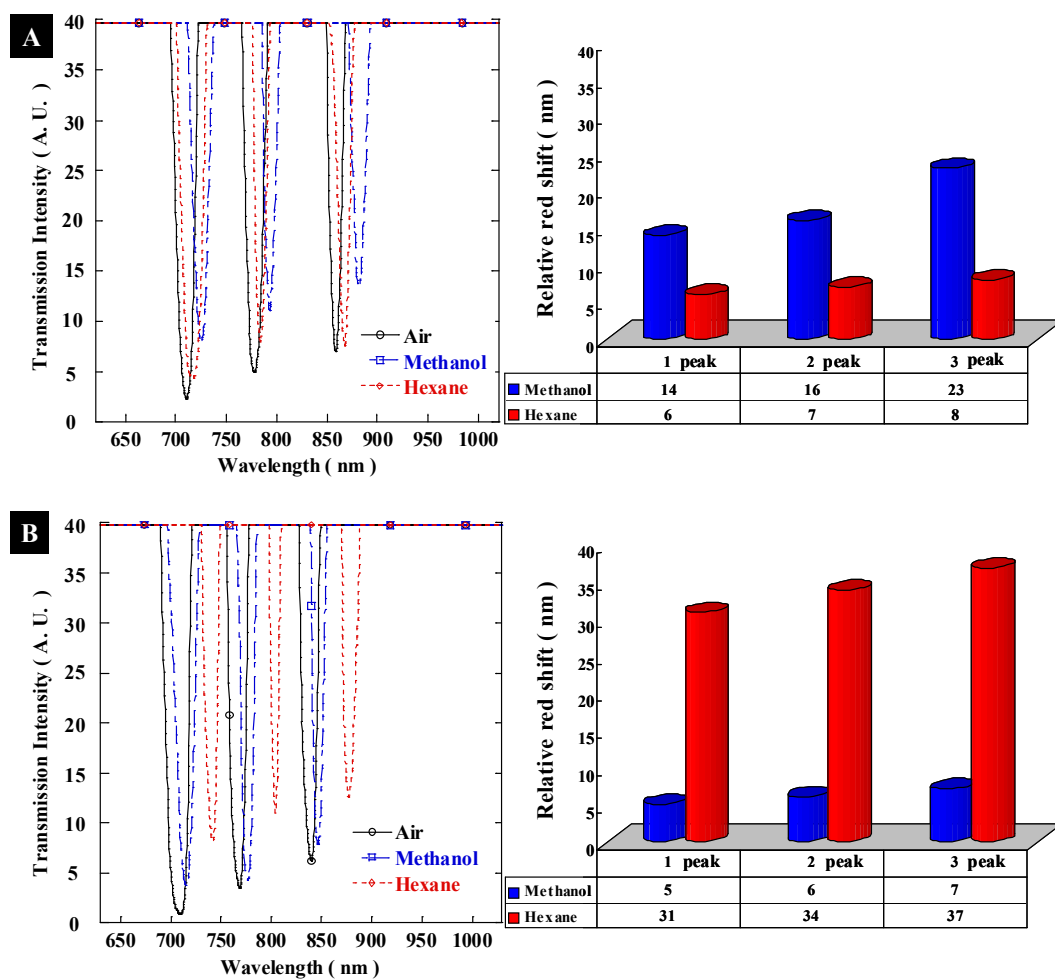
Figure 5.5. Transmission spectra and red-shifts of transmission resonances under exposure to different media. (A) Oxidized and (B) dodecyl modified composite films.

To investigate the response behavior of transmission resonances, the triple encoded rugate PS composite films were subjected to the repetitive exposure to methanol

vapors. Figure 6 displayed the change of transmission intensities at a fixed wavelengths obtained from transmission minima (726, 788, and 863 nm). Each exposure time of the methanol vapor was 10 s. The repetitive exposure exhibited a consistent result to show the degree of reproducibility. The transmission intensities at the fixed wavelengths were dramatically changed due to the red shift of transmission resonances after exposure to methanol vapor. A recovery response of shorter transmission wavelength to the methanol vapor was faster than that of longer transmission wavelength. The real-time measurement of transmission resonance upon exposure to the methanol vapor indicated that these composite films were robust and reusable and might be useful for an application as chemical sensors.
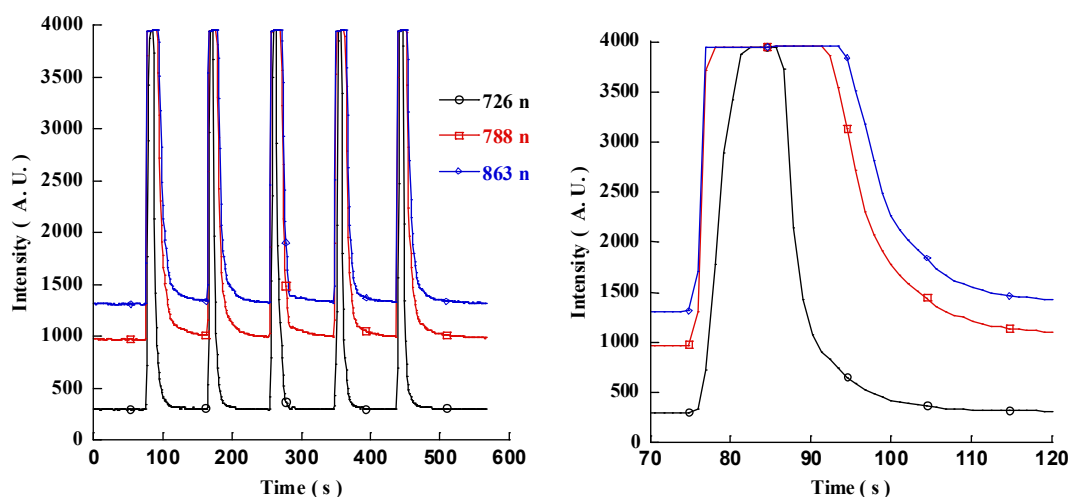
Figure 5.6. Real time responses of transmission resonances at three fixed wavelengths under exposure to methanol vapor.

5.4 Conclusions

Rugate PS/polymer composite films were successfully prepared and displayed sharp transmission resonances where the wavelengths were controllable. The transmission resonance of the composite film was tunable by the control of dose media and served as a band-rejection filter upon exposing to the organic vapor. The composite film was flexible and its mechanical stability was significantly improved without degradation in their optical transmission properties. The surface modification of this composite film indicated that the respond of transmission resonances depended on the surface properties of the composite films.

5.5 References

[1] H. Sohn, S. Letant, M. J. Sailor and W. C. Trogler, *J. Am. Chem. Soc*. **122**, 5399 (2000).

[2] Y. Y. Li, F. Cunin, J. R. Link, T. Gao, R. E. Betts, S. H, Reiver, V. Chin, S. N. Bhatia, and M. J. Sailor, *Science* **299**, 2045 (2003).

[3] X. Li, J. L. Coffer, Y. D. Chen, R. F. Pinizzotto, J. Newey, and L. T. Canham, *J. Am. Chem. Soc.* **120**, 11706 (1998).

[4] M. S. Yoon, K. H. Ahn, R. W. Cheung, H. Sohn, J. R. Link, F. Cunin, and M. J. Sailor, *Chem. Commun.* 680 (2003).

[5] J. Dorvee and M. J. Sailor, Phys. Stats. Sol. 202, 1619 (2005).

[6] V. Chin, B. E. Collins, M. J. Sailor, and S. N. Bhatia, *Adv. Mater.* **13**, 1877 (2001).

[7] L. T. Canham, *Adv. Mater.* **7**, 1033 (1995).

[8] B. E. Collins, K.-P. Dancil, G. Abbi, and M. J. Sailor, *Adv. Funct. Mater.* **12**, 187 (2002).

[9] X. G. Zhang, *J. Electrochem. Soc.* **151**, C69 (2004).

[10] F. Cunin, T. A. Schmedake, J. R. Link, Y. Y. Li, J. Koh, S. N. Bhatia, and M. J. Sailor, *Nat. Mater.* **1**, 39 (2002).

[11] J. Park, S. Cho, Y. C. Ko, and H. Sohn, *J. Korean Phys. Soc.* **50**, 695 (2007).

[12] S. Jang, J. Kim, Y. Koh, Y. C. Ko, H. -G. Woo, and H. Sohn, *J. Nanosci. Nanotechnol.* 7, 4049 (2007).

[13] M. Ghulinyan, C. J. Oton, G. Bonetti, Z. Gaburro, and L. Pavesi, *J. Appl. Phys.* **93**, 9724 (2003).

[14] J. Kim, Y. Koh, S. Jang, Y. C. Ko, H.-G. Woo, and H. Sohn, *J. Nanosci. Nanotechnol.* **7**, 4165 (2007).

Chapter Six
Targeted Delivery and Controlled Release of Camptothecin to Cancer Cells Using Covalent Attachment Method of Porous Silicon "Smart Particles"

6.1 Introduction

Nano-structured delivery systems based on photonic crystal is strongly affecting for the systemic delivery of therapeutic molecules and imaging agents for various biomedical applications, from cancer to cardiovascular diseases [1-3]. The goal of all sophisticated drug delivery systems is to deploy medications intact to specifically targeted parts of the body through a medium that can control the therapy's administration by means of either a physiological or chemical trigger. Inorganic nanostructured materials have gained considerable importance in several biotechnological applications related to drug delivery because inorganic materials exhibit more superior structural and chemical stability compared to organic materials. During the past decade, various drug delivery vehicles have been employed, such as microspheres, gelatin nanoparticles [4], polymer micelles [5], hydrogel-type materials [6], and PS [7]. These materials focused on formulating therapeutically active agents have all been shown to be effective in enhancing drug targeting specificity, lowering systemic drug toxicity, improving treatment absorption rates, and providing protection for pharmaceuticals against biochemical degradation. The PS prepared by an electrochemical etch of single crystal silicon possesses

several properties that make it advantageous as a drug delivery system including open pore photonic structure, a high surface area, and tunable pore sizes and volumes [8]. Chemical modification and permeation of the PS surface can also be achieved, providing many means to adjust the chemical stability of the material as well as to load a particular drug of interest [9]. The PS as porous matrices was employed to demonstrate in vivo release of the steroid dexamethasone [10], ibuprofen [11], doxorubicin [12], and many other drugs [13]. Current drug delivery system based on PS included that the free volume inside pores was loaded with a drug that would be released in the body by the dissolution of the matrix, however site-specific and/or time-controlled delivery of drug were not specified. As with all biodegradable drug delivery carriers, the toxicity of the degradation products is an important factor. Silicon is an essential trace element that is linked to the health of bone and connective tissues. The bio-available form of silicon consists of various oxo anions of orthosilicic acid (Si(OH)4), which are rapidly removed by the kidneys in the human body [14,15]. The low toxicity, degradation properties, and solubility of PS dioxide have generated much interest in its use in controlled drug deliver systems [16].

CPT, a pentacyclic alkaloid, isolated first by Wall and co-workers from the Chinese tree Camptotheca acuminata, shows potent cytotoxic activity against a range of tumor cell lines [17]. However, administration of this drug was accompanied by severe side effects, due to its poor water solubility. CPT polymeric drugs were reported to improve the therapeutic efficacy in the controlled release of drugs [18]. This paper focused on microparticle systems using multi-encoded rugate PSD having a photonic structure of rugate-structured PS by applying a computer-generated pseudo-sinusoidal composite current-time waveform using superposition method [19]. Multi-encoded rugate PSD smart particles were prepared

in micron size and chemically attached with anti-cancer agents, Camptothecin (CPT). The covalent method described here allows for drug release only when the covalent bonds are broken. We observe a significant, extended release of CPT that is covalently attached to the PSD matrix compared to CPT that is physically adsorbed into the PSD matrix and the optical interference spectrum from multilayers has been used to monitor release of a drug.

6.2 Experimental

6.2.1   Preparation of free-standing multi-encoded rugate PSD film

Multi-encoded rugate PS samples were prepared by electrochemical etch of heavily doped p^{++}-type silicon wafers (boron doped, polished on the (100) face, resistivity of 0.8-1.2 m$\Omega \cdot$cm, Siltronix, Inc.). The etching solution consisted of a 3:1 volume mixture of aqueous 48% hydrofluoric acid (ACS reagent, Aldrich Chemicals) and absolute ethanol (ACS reagent, Aldrich Chemicals). Typical etch parameters for rugate structure involved using a periodic sine wave current between 5.3 mAocm-2 and 120.8 mA$\cdot$cm^{-2} for 2000 s. The resulting multi-encoded rugate PS film was lift off from the silicon substrate by an applying of electropolishing current at 22 mA$\cdot$cm^{-2} for 150 s in a solution of 48% aqueous HF and ethanol (1:15 by volume) to obtain a free-standing multi-encoded rugate PS. The silicon surface was predominant hydride-terminated after the etching procedure. This surface was sensitive to oxidation and hydrolysis upon exposure to aqueous solution. Thermally oxidized multi-encoded rugate PSD films were obtained by heat treatment in a furnace (Thermolyne F6270-26 furnace equipped with controller) using the following parameters: initial ramp rate, 5 ℃/min to 300 ℃; hold time, 3 h; and passive cooling to ambient temperature.

6.2.2   Chemical attachment of CPT to multi-encoded rugate PSD surface and preparation of PSD-CPT smart particles

13.8 mg of (s)-(+)-camptothecin (CPT) (0.05 mmol, Aldrich Chemicals) was

dissolved in 10 mL of methylene chloride. The mixture solution was stirred for 30 min, and 4-di(methylamino)pyridine (DMAP) (0.1 mmol, Aldrich Chemicals) was added to the solution. The reaction mixture was allowed to stir at room temperature for 1 h. The resulting solution was added to the oxidized multi-encoded rugate PSD films and films were incubated for 72 h. Afterward the multi-encoded rugate PSD films were rinsed successively with toluene, acetone, and methylene chloride and subsequently dried under a stream of nitrogen. The multi-encoded rugate PSD films were made into particles by ultrasonic fracture in an organic solution and dried under an atmosphere.

6.2.3 Cell viability using cell culture

The MCF-7 cancer cells were grown in Dulbecco's Modified Eagle Medium (DMEM; GIBCO, Grand Island, N,Y, USA) containing 10% Fetal Bovine serum (FBS; GIBCO, Grand Island, N,Y, USA). Cells were cultured at 37 ℃ in an atmosphere of 5% CO2 and 100% humidity. The capacity of CPT to interfere with growth of the MCF-7 cancer cell line was determined using the MTT assay. Briefly, MCF-7 cancer cell was grown in 96 well (1×10^4 cells/well) and incubated in growth medium at 37 ℃ for 24 h the culture medium containing CPT at various concentrations. It followed by the addition of 100 uL of MTT (3-(4,5-dimethyl-2-thiazolyl)-2,5-diphenyl-tetrasolium bromide) solution (5 mg/mL), and incubation for 4 h in the 37 ℃. The supernatant was carefully removed from each well and 100 uL of DMSO (Dimethyl sulfoxide, ACS reagent, Aldrich Chemicals) was added to each well to dissolve the formazan crystals which were formed by the cellular reduction of MTT. The absorbance of each well was measured by a microplate reader using a test wavelength of 540 nm.

6.2.4 Instrumentation and Data Acquisition

Optical reflectivity spectra were measured using a tungsten-halogen lamp and an Ocean Optics S2000 CCD spectrometer fitted with a fiber optic input. The reflected light collection end of the fiber optic was positioned at the focal plane of the optical microscope. CPT released in pH 4, 7, and 9 aqueous buffer solution was measured by UV-vis spectrometer (UV-2401 PC, Shimazu). FT-IR spectra were acquired with a FT-IR (Nicolet 5700) instrument in the diffuse reflectance mode (Spectra-Tech diffuse reflectance attachment). Absorption spectra were reported in absorbance units. The quantity of CPT release from the derivatized multi-encoded rugate PSD smart particle was measured at the fixed absorption wavelength of 369 nm on a time scale, which was the absorption maximum of CPT. The morphology of PSD-CPT smart particles were observed with cold field emission scanning electron microscope (FE-SEM, S-4700, Hitachi).

6.3 Results and Discussion

PS were fabricated by electrochemical etching of highly doped p-type silicon wafer in an aqueous electrolyte containing HF and ethanol. Photonic crystals containing rugate structure resulted in a mirror with high reflectivity in a specific narrow spectral region. Multi-encoded rugate PS were prepared by applying a computer-generated that the individual sine components were summed together to create a composite waveform. This reflection resonance could be tuned to appear anywhere in the visible to near-infrared spectral range, depending on the programmed etch waveform. The waveform used in the present work, which was represented by Equation 1.

$$y_{comp} = A_1\sin(k_1t) + A_2\sin(k_2t) +....... + A_n\sin(k_it) + B \quad (1)$$

Where y_i represented a temporal sine wave of amplitude, A_i; frequency, k_i; time, t; applied current density, B. Equation 1, containing all the encoding information, can be converted to an analog current-time waveform for etching by using a computer-controlled digital galvanostat.

Multiple rugate structures were generated by using different parameters in Equation 1 and displayed the corresponding reflection resonances as shown in Figure 1. The values of A_i and B for every sine components were 5.3 and 120.8 mA, respectively. A composite waveform containing one to four frequency components was used. The values of k_i for each of the sine components varied from 0.30 to 0.42 Hz, with a spacing of 0.03 Hz between each sine component.

Multiple encoded rugate PS etched with 0.42, 0.39, 0.36, 0.33, and 0.30 Hz exhibited five sharp lines at 575, 613, 658, 714, and 781 nm, respectively. Each of

the main peaks in the optical reflectivity spectrum was superimposed over each peak and corresponded to one of the sine components of the composite waveform, indicating that the reflectivity spectrum represented the Fourier transform of the composite current-time waveform. After the generation of optically encoded rugate PS, the resulting PS films were removed from the silicon substrate by applying an electropolishing current to obtain a free-standing rugate PS film. The thermal oxidation of free-standing rugate PS films at 300 ℃ converted the hydride-terminated surface into hydroxyl terminated rugate PSD films. Rugate PSD films were reacted with CPT to give PSD-CPT films and then ultrasonicated to create particles. Particles with sizes ranging from several hundred nanometers to few hundred micrometers were generated depending on the duration of ultrasonication. The chemistry of functionalization was outlined in Scheme 1.
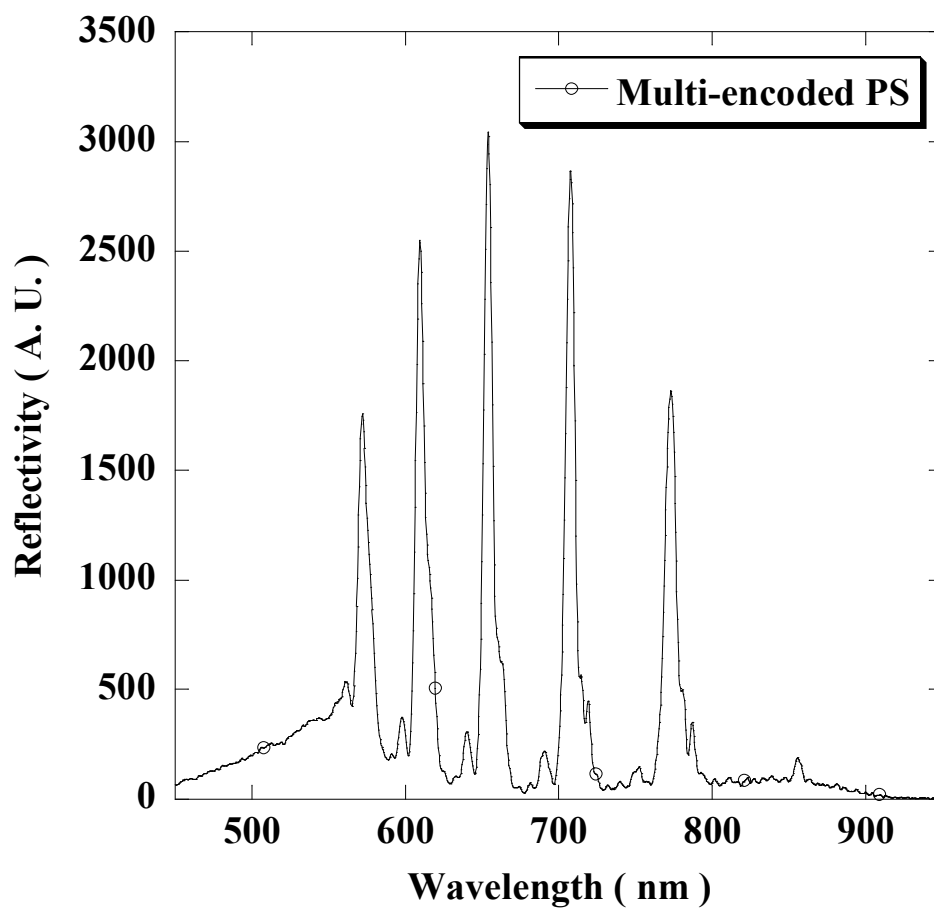
Figure 6.1. Reflectivity spectrum of multi-encoded rugate PS prepared by applying a computer-generated that the individual sine components were summed together to create a composite waveform.
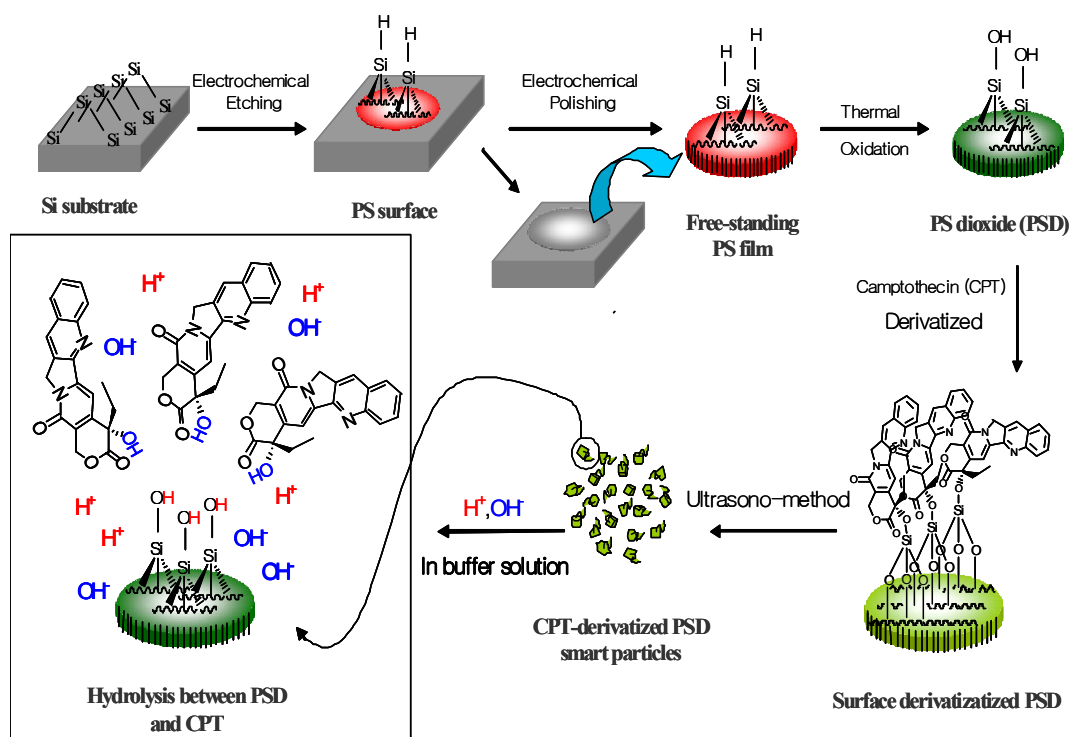
Scheme 6.1. Schematic process for multi-encoded rugate CPT-derivatized PSD smart particle.

Photograph of multi-encoded rugate PSD-CPT smart particles is shown in Figure 2A and illustrates that its color results from the reflection of the smart particles. Also, the surface morphology of multi-encoded PSD-CPT smart particles were obtained with cold FE-SEM and shown in Figure 2B. Size of multi-encoded PSD-CPT smart particles was about 30 ~ 60 micrometers. The surface image of multi-encoded PSD-CPT smart particles indicated that the pore size of particle retained a good porosity without destruction of porous structure during ultrasonication. The prepared PSD-CPT smart particles had cylindrical macropores with the average pore size of 100 nm.
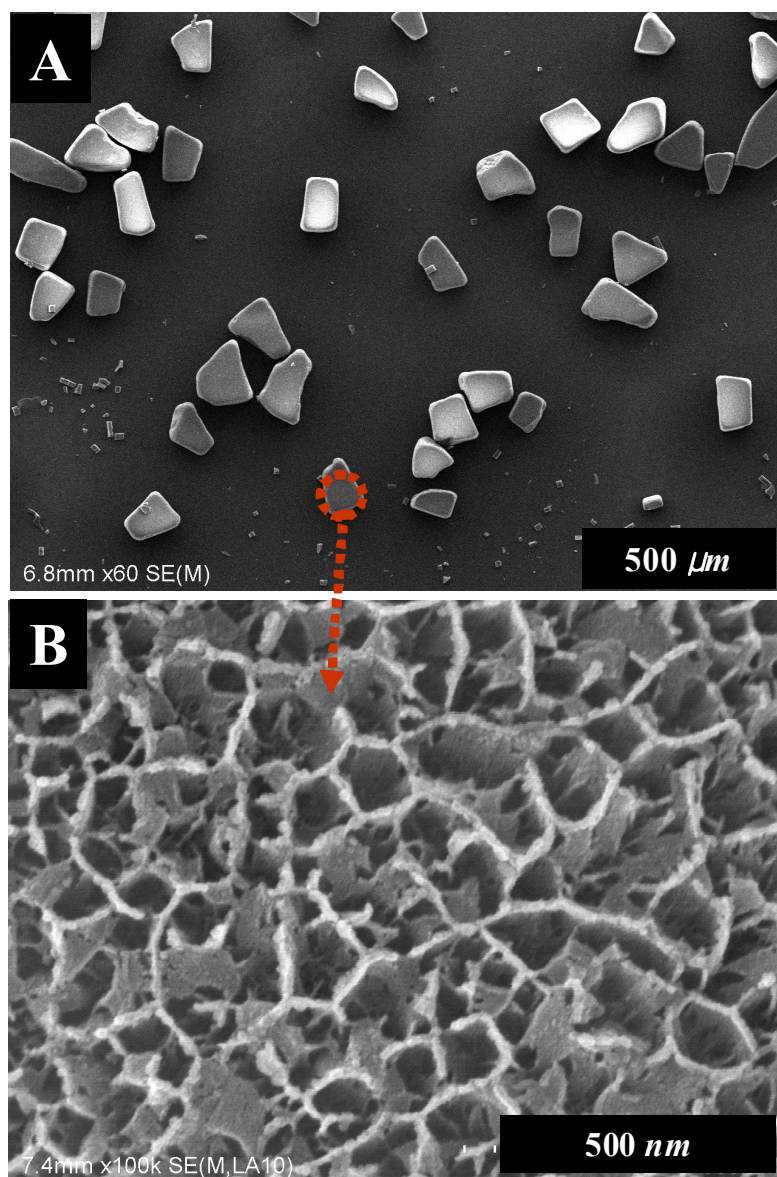
Figure 6.2. Surface FE-SEM images of multi-encoded rugate PSD-CPT smart particles.

   These step by step procedures were monitored by diffuse reflectance FT-IR spectroscopy as shown in Figure 3. Figure 3(solid line) showed that the FT-IR spectrum of freshly etched multi-encoded rugate PS displayed a characteristic broad band centered at 2100 and 900 cm^{-1} for the υ(Si-H) stretching vibration and δ (Si-H) bending vibration. After the thermal oxidation of multi-encoded rugate PS film, the presence of silicon oxide was determined by FT-IR measurement as shown in Figure 3(dashed line). Thermal oxidation of the porous silicon layer resulted significant loss of intensity of the υ(Si-H) modes in the infrared spectrum at 2150 cm-1, but vibrational bands due to oxygen-back-bonded silicon hydride, υ (OSi-H) and δ(OSi-H) modes, grew at 2300 and 850 cm^{-1}, respectively. Multiple silicon oxide species, Si-O-Si, displayed a strong, very broad absorption band between 1000 and 1250 cm^{-1}. Condensation of the Si-OH surface of PSD with CPT generated a surface-bound CPT. The FT-IR spectrum shown in Figure 3(dotted line) displayed additional bands characteristic of CPT (the aromatic C=C band of υ(C=C) at 1650 cm^{-1} and 1570 cm^{-1}, respectively. Surface derivatization led to complete disappearance of the OSi-H vibrational bands.

   Prepared multi-encoded rugate PSD-CPT smart particles were placed at the bottom of 3 mL quartz cuvette containing the buffer solution (pH 4, 7, and 9) of three types. The appearance of CPT in solution was determined by monitoring the UV absorbance band. Prepared PSD-CPT smart particles were stable in buffer solutions for several days without apparent degradation. To examine the drug delivery application, the release of CPT and the shift of reflection peak were simultaneously measured by the use of UV-vis and reflectance spectrometer. The release process of CPT from the PSD-CPT smart particles shown in Scheme 1 involved the hydrolysis by covalent attachment between PSD and CPT. Absorption measurement for the CPT release from the PSD-CPT smart particles in buffer

solution was achieved as a function of time at fixed wavelength of 369 nm which was the absorption maxima of CPT. The hydrolysis between PSD and CPT of smart particles as shown in Figure 4 becomes quickly saturated as the pH values of buffer solution increases.
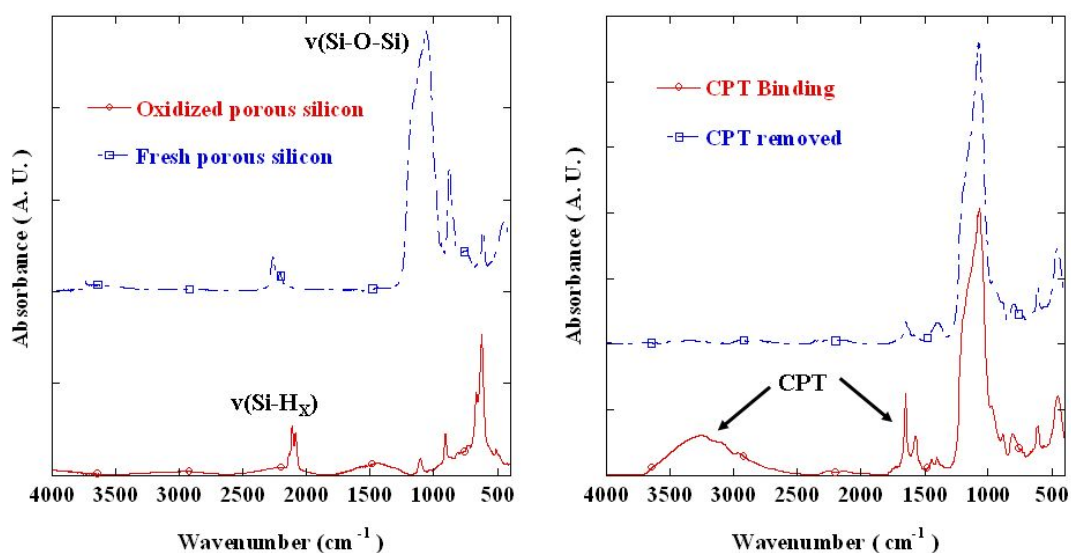
Figure 6.3. Transmission-mode FT-IR spectra of PS sample (left led line), PSD sample (left blue line), CPT-derivatized PSD sample (light led line), and CPT-removed PSD sample (light blue line).
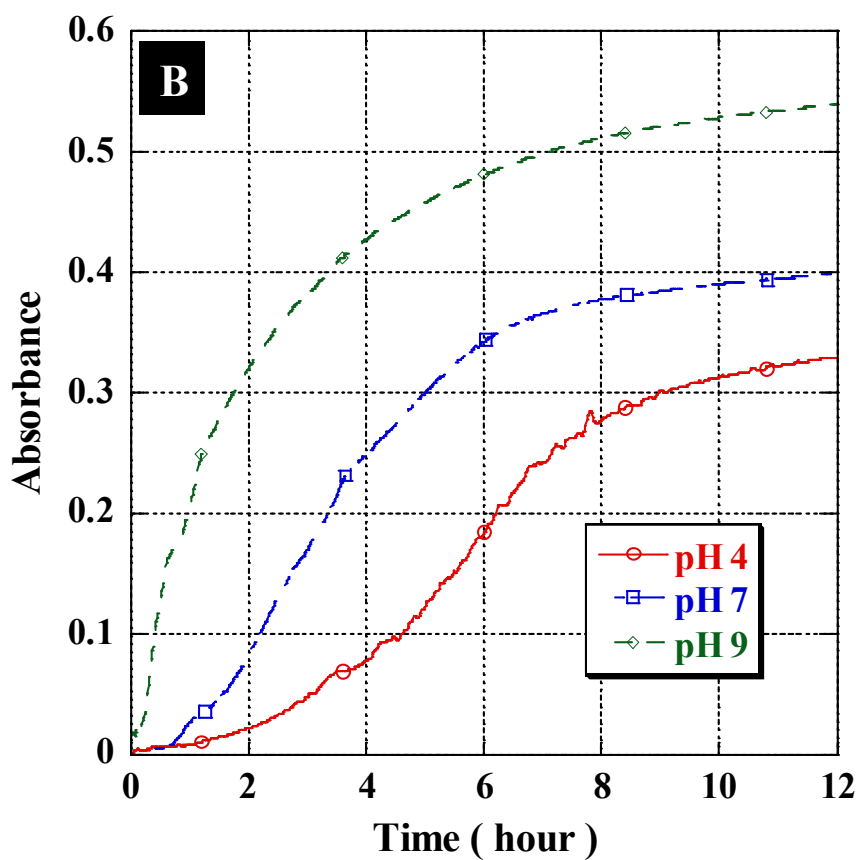
Figure 6.4. Percent of CPT appearing in buffer solution (pH 4, 7, and 9) as a function of time, measured by monitoring the UV-vis absorption band at 369 nm in the solution.

Figure 5 showed the change of reflection spectrum under the exposure of CPT loaded by covalent attachment to the CPT-PSD smart particles. As expected, exposition to each a buffer solution of CPT to the CPT-derivatized porous layer resulted in an decrease in the blue shift of reflection spectrum, indicative of a change in refractive index induced by covalent attachment of CPT into the CPT-PSD smart particles.

An MTT (3-(4,5-dimethyl-2-thiazolyl)-2,5-diphenyl-tetrasolium bromide) toxicity assay was used to test cell viability. Cells were exposed to free CPT, empty PSD smart particles, and PSD-CPT smart particles in which CPT was loaded by covalent attachment. The each of sample was added to MCF-7 cells and assessed for cytotoxicity 24 h after exposure as shown in Figure 6. The viability of cells exposed to PSD-CPT was significantly lower than cells exposed to empty PSD smart particles and somewhat higher than cells exposed to the same quantity of free CPT. It should be noted that PS is able to reduce MTT in the absence of cells, giving rise to an apparent lack of toxicity. The CPT is increasingly in clinical use and show great utility in the treatment of various cancers including primary and metastatic colon carcinoma, small cell lung carcinoma ovarian, breast, pancreatic, and stomach cancers. However, administration of this drug was accompanied by severe side effects, due to its poor water solubility. As mentioned above, PSD-CPT smart particles are decreased toxicity of CPT and are maintained their efficiency with drug materials.
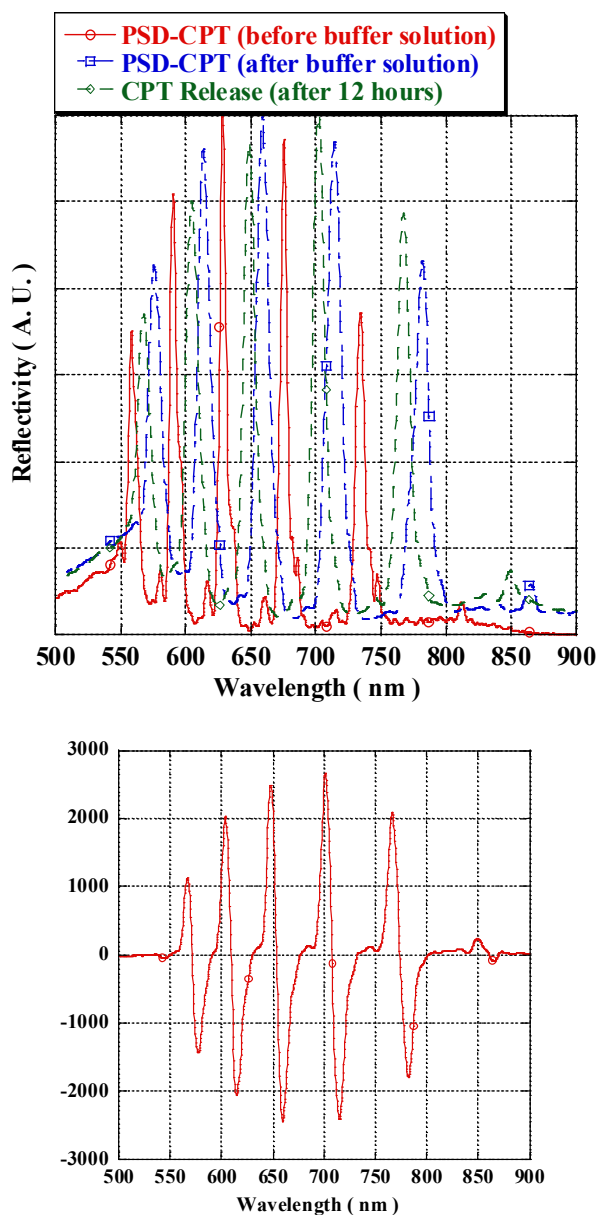
Figure 6.5. The change of reflection spectrum and differential signalunder the exposure of CPT loaded by covalent attachment to the CPT-PSD smart particles.
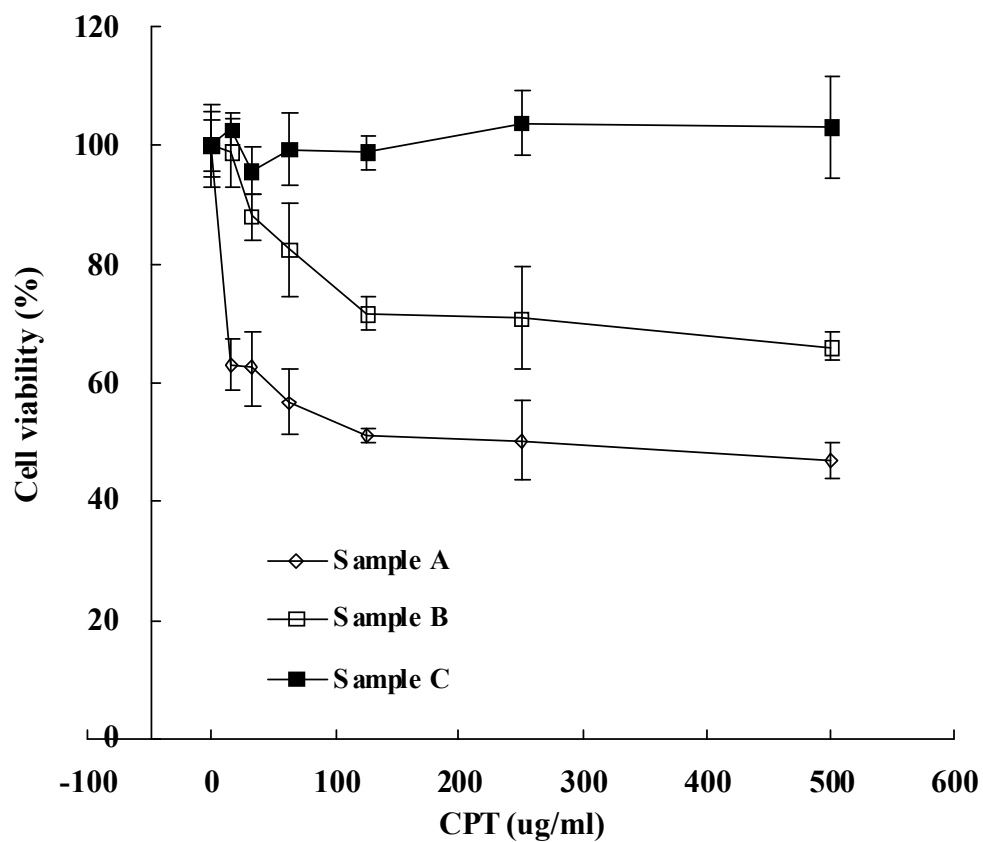
Figure 6.6. Viability of MCF-7 cells (MTT assay) after exposure to free CPT, CPT-PSD, and PSD.

6.4 Conclusion

The use of smart particles based on multi-encoded rugate PS has been demonstrated for the drug delivery application. Loading of CPT was achieved in PSD-CPT smart particles. Multi-encoded rugate films were removed from the silicon wafer by applying an electropolishing current to obtain free-standing multi-encoded rugate films. The thermal oxidation of free-standing multi-encoded rugate films converted the hydride-terminated surface into hydroxyl terminated PSD. PSD films were reacted with CPT and then ultrasonicated to create particles to give PSD-CPT smart particles. In this paper, targeted delivery of CPT using multi-encoded rugate PSD smart particles can be accomplished by covalent attachment. The covalent attachment method was tested with the anticancer drug CPT, and release of the active drug was verified by the MTT cellular viability assay. This method allows the grafted molecule to be released only when the covalent bonds are broken or when the matrix is degraded.

6.5 Reference

[1] R. Shinha, G. J. Kim, S. Nie, and D. M. Shin, *Mol. Cancer Ther.* **5**, 1909 (2006).

[2] I. I. Slowing, J. L. Vivero-Escoto, C.-W. Wu, and V. S.-Y Lin, Adv. *Drug Deliv. Rev.* **60**, 1278 (2008).

[3] G. A. Hughes, *Nanomedicine* **1**, 22 (2005).

[4] L. E. van Vlerken, Z. F. Duan, M. V. Seiden, and M. M. Amiji, *Cancer Res.* **67**, 4843 (2007).

[5] V. Torchilin, *Pharm. Res.* **24**, 1 (2007).

[6] K. M. Tynera, S. R. Schiffmanb, and E. P. Giannelisb, *J. Control. Release* **95**, 501 (2004).

[7] Y. Y. Li, F. Cunin, J. R. Link, T. Gao, R. E. Betts, S. H. Reiver, V. Chin, S. N. Bhatia, and M. J. Sailor, *Science* **299**, 2045 (2003).

[8] E. J. Anglin, L. Cheng, W. R. Freeman, and M. J. Sailor, *Adv. Drug Deliv. Rev.* **60**, 1266 (2008).

[9] S. D. Alvarez , A. M. Derfus, M. P. Schwartz, S. N. Bhatia, and M. J. Sailor, *Biomaterials* **30**, 26 (2009).

[10] E. J. Anglin, M. P. Schwartz, V. P. Ng, L. A. Perelman, and M. J. Sailor, *Langmuir* **20**, 11264 (2004).

[11] C. Charnay, S. Begu, C. Tourne-Peteilh, L. Nicole, D. A. Lerner, and J. M. Devoisselle, *Eur. J. Pharm. Biopharm.* **57**, 533 (2004).

[12] L. Vaccari, D. Canton, N. Zaffaroni, R. Villa, M. Tormen, and E. di Fabrizio, *Microelectron. Eng.* **83**, 1598 (2006).

[13] J. Salonen, A. M. Kaukonen, J. Hirvonen, and V. P. Lehto, *J. Pharm. Sci.* **97**, 632 (2008).

[14] S. H. C. Anderon, H. Elliott, D. J. Wallis, L. T. Canham, and J. J. Powell,

Phys. Status Solidi A **197**, 331 (2003).

[15] L. T. Canham, C. L. Reeves, D. O. King, P. J. Branfileld, J. G. Crabb, and M. C. L. Ward, *Adv. Mater.* **8**, 850 (1996).

[16] E. C. Wu, J.-H. Park, J. Park, E. Segal, and F. Cunin, *ACS Nano* **2**, 2401 (2006).

[17] M. E. Wall, M. C. Wani, K. H. Cook, A. T. McPhail, and G. A. Sim, *J. Am. Chem. Soc.* **88**, 3888 (1966).

[18] N.-J. Lee, S.-J. Lee, S.-H. Kim, Y.-S. Kang, S.-B. Moon, H. Sohn, K.-T. Kang, and E. A. Theodorakis, *Eur. Polym. J.* **40**, 1291 (2004).

[19] J. Kim, S. Jang, Y. Koh, C. Park, H.-G. Woo, S. Kim, and H. Sohn, *J. Nanosci. Nanotechnol.* **8**, 4951 (2008).

Part II.

Photoanode Structured Porous Polymer Replica based on Porous Silicon and Its Applications

Chapter Seven

Fabrication and Optical Characterization of Rugate-structured Polymer Replicas

7.1 Introduction

The development of new methods to build photonic structures in a device is of great interest, since conventional lithographic method is too complex to fabricate. An electrochemical etch is one of lithographic methods to fabricate a photonic structures into the materials. Since the discovery of porous silicon [1], multilayer-structured PS has been intensively investigated for a variety of applications such as chemical [2,3] and biological sensors [4], medical diagnostics [5], optical band pass filters [6], micro chemical reactors [7], and micro fuel cells [8,9]. Its importance is due to very high surface area as well as their unique photonic properties.

Multilayered PS is an attractive candidate for building photonic structure, because the porosity and average pore size can be tuned by adjusting the electrochemical preparation conditions that allow the construction of photonic crystals [10,11]. Multilayer PS such as DBR PS [12] or rugate PS [13] exhibit unique optical properties providing a reflection band at specific wavelength in the optical reflectivity spectrum. However porous silicons are limited by their chemical and mechanical stability for many applications, because these films are very brittle [14].

In addition, they are not suitable for the application of biological sensors *in vivo* due to the presence of silicon metal of the PS films. To overcome these issues, polymer materials showing identical optical properties might be an alternative [15,16].

In the present work, we have prepared polystyrene replicas showing rugate photonic structure by casting of polystyrene solution onto an oxidized rugate PS films, where the PS films are used as templates for building nanostructured materials. Replication process and photonic features of the polymer replicas are presented. This provides the means for the construction of complex photonic structures of polymers that are compatible with harsh environments and improves chemical and mechanical stability.

7.2 Experimental

7.2.1 Preparation of rugate PS Samples

Rugate PS samples were prepared by an electrochemical etch of heavily doped p^{++}-type silicon wafers (boron doped, <100> oriented, resistivity of 0.8-1.2mΩ-cm, Siltronix, Inc.). The etching solution consisted of a 3:1 volume mixture of aqueous 48% hydrofluoric acid (ACS reagent, Aldrich Chemicals) and absolute ethanol (ACS reagent, Aldrich Chemicals). Rugate PS samples were prepared by using a computer-generated sinusoidal current waveform with limits of 11.5 to 34.6 mA/cm^2, 100 repeats, and periods on the order of 8 sec depending on the desired wavelength of maximum reflectivity. The porous layers generated in the electrochemical etch were smooth enough to create high-quality 1D photonic crystals. Free-standing rugate PS films were obtained from the silicon substrate by an applying of electropolishing current at 460 mA/cm^2 for 2 min in an ethanoic 37.5% aqueous HF solution, and then at 22 mA/cm^2 for 2 min in an ethanoic 3.3% aqueous HF solution.

7.2.2 Preparation of Photonic Polymer Replicas

Preparation of Photonic Polymer Replicas. Free-standing rugate PS films were thermally oxidized in the furnace at 450 ℃ for 2 h. In a typical preparation, 4 g of polystyrene (Aldrich, Mw = 280,000) are dissolved in 20 mL of toluene (Fisher Scientific). The toluene solution was cast into the porous SiO$_2$ films and the samples were annealed in an oven at 95 ℃ for 20 min. Then oxidized rugate PS

matrix from the composite films were removed in aqueous 8% HF solution for 12 h. After the removal of the oxidized rugate PS template by chemical dissolution, the polymer castings replicate the photonic features and the nanostructure of the master.
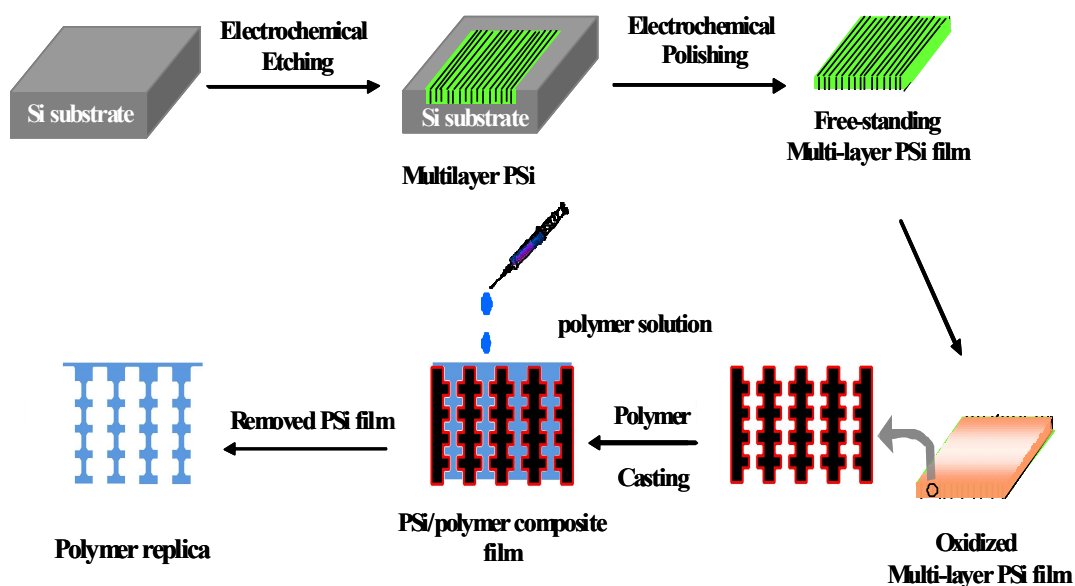
Scheme 7.1. Preparation method of polymer replica containingphotonic structure.

7.2.3 Instrumentation and Data Acquisition

The anodization current was supplied by a Keithley 2420 high-precision constant current source which was controlled by a computer to allow the formation of PS multilayers. Optical reflectivity spectra were measured using a tungsten-halogen

lamp and an Ocean Optics S2000 CCD spectrometer fitted with a fiber optic input. The reflected light collection end of the fiber optic was positioned at the focal plane of the optical microscope. The morphology of rugate PS film and polymer replica were observed with cold field emission scanning electron microscope (FE-SEM, S-4700, Hitachi). The surface characterization of fresh and oxidized rugate PS samples for chemical properties was achieved by fourier-transform infrared (FT-IR, Nicolet 5700, Thermo Electron Co.). Rugate PS film and polymer replica were characterized by X-ray diffractometer (XRD, D/MAX-3C, Riguku Co.) with CuK radiation (0.15406 nm). The XRD patterns were collected in the 2 theta range of 3-90° at room temperature.

7.3 Results and Discussion

Multilayered porous silicon has been successfully prepared using a periodic galvanostatic electrochemical etch of crystalline silicon by applying a sine wave current. The applied current density is modulated with a pseudo sine wave to generate a periodically varying porosity gradient. Rugate PS samples display a very sharp reflection line at 585 nm without sidelobes around the reflectance peak in the optical reflectivity spectrum as shown in Figure 1. The spectral band of rugate PS sample has a FWHM of about 17 nm, which is much narrower than that of fluorescence spectrum obtained from a fluorescent organic molecules or quantum dot [17].
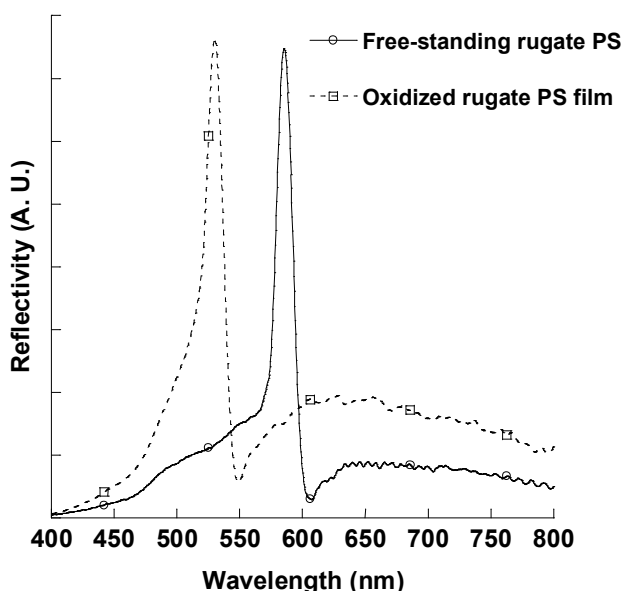
Figure 7.1. Optical reflectivity spectra of free-standing and oxidized rugate PS film.

An electrochemical etching offers the opportunity to modulate the porosity in depth and allows the fabrication of structures with any refractive index profile. When the current is gradually modulated, a smooth index profile of rugate PS can be achieved. An effective refractive index of rugate PS depends directly on porosity. The shape, size, and orientation of pores of PS layers depend on surface orientation and the dopant level of the crystalline silicon substrate as well as the applied current density, the temperature, and the concentration of the HF etching solution. The pore size of p-type PS can be increased by increasing the concentration of the dopant and decreasing the aqueous HF concentration. High current densities result in the desired well-defined cylindrical macropores, rather than the random orientation of highly interconnected micropores. The surface and cross-sectional FE-SEM images of rugate PS shown in Figure 2 illustrate that the thickness of rugate PS is about 37.5 μm. FE-SEM image of rugate PS displays a sinusoidally varying porosity gradient in the direction perpendicular to the plane of the filter. FE-SEM image of rugate PS indicates that the prepared rugate PS has cylindrical mesopores with the average pore size of 10 nm.
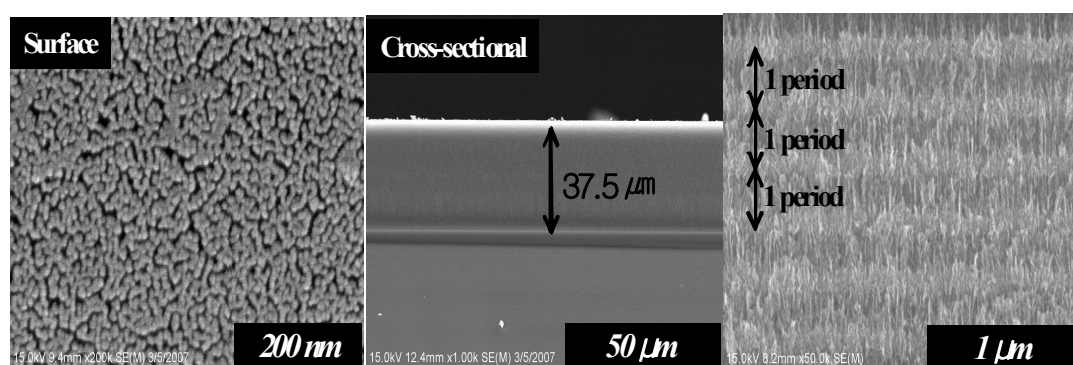
Figure 7.2. Surface and cross-section SEM images of rugate PS.

The waveform used in the present work involves a sine component, which is represented by

$$\mathbf{y}_i = A_i \left[\sin \left(k_i t \right) \right] + \boldsymbol{B} \quad \text{--------------} \quad (1)$$

where $\mathbf{y}_i$ represents a temporal sine wave of amplitude A_i, frequency k_i, time t, and an applied current density $\boldsymbol{B}$. The position of reflection band depends on the frequency. In this work, the value of A_i and $\boldsymbol{B}$ was 11.55 and 23.05 mA, respectively. When the frequency was 0.125 Hz, a sharp reflection line at 585 nm was obtained.

The resulting rugate PS films can be lifted off from the silicon substrate to obtain a free-standing rugate PS films by an applying of lift-off current in a solution of HF and ethanol. The reflectivity of free-standing rugate PS film occurs at the identical location. Free-standing rugate PS films are very brittle when these films are subjected to minor shear stresses. Thermal oxidation of these films is carried out in the furnace at 450℃ for 2 h. The reflection spectrum for the oxidized rugate PS film exhibits its reflectivity at 531 nm, shifted to shorter wavelengths by 54 nm due to the decrease of an average refractive index from silicon to silicon dioxide.

After the thermal oxidation of rugate PS film, the presence of silicon oxide has been determined by FT-IR measurement as shown in Figure 3. The FT-IR spectrum of fresh rugate PS film exhibits vibrational bands in the fingerprint region of the spectrum. ∪ (Si-H) and δ (Si-H) vibrations associated with surface Si-H species are also apparent at 2117 and 941 cm^{-1}, respectively. However, the oxidized rugate PS film exhibits vibrational bands characteristic of ∪ (OSi-H), δ (OSi-H), and ∪ (Si-O) vibratioal modes are observed at 2270, 881, and 1070 cm^{-1}, respectively.
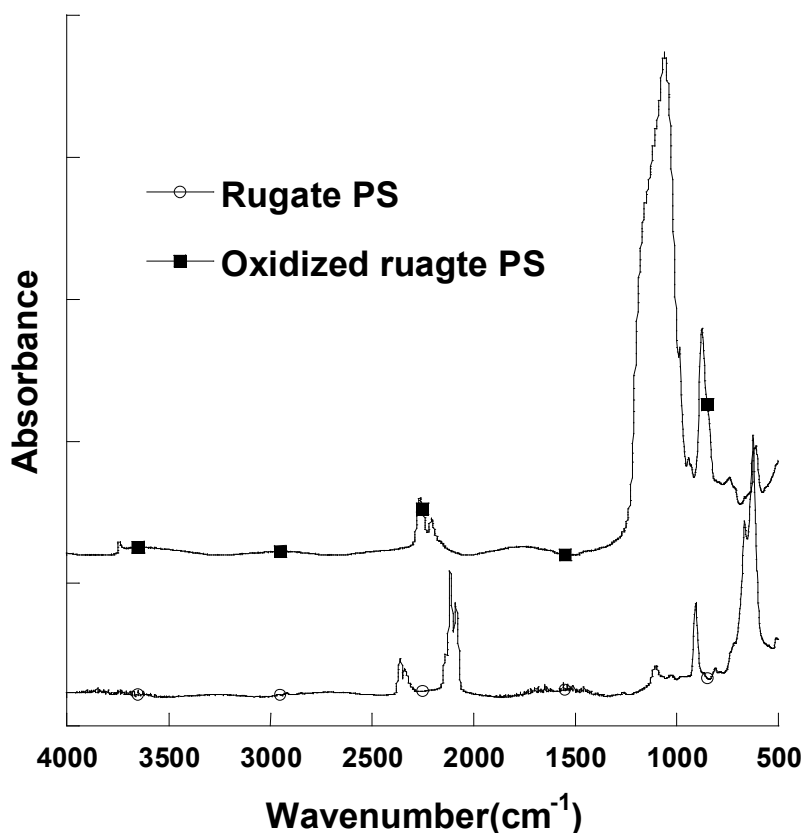
Figure 7.3. FT-IR spectra of free-standing and oxidized rugate PS film.

Polystyrene has been dissolved in toluene and cast on the top surface of oxidized rugate PS film. After drying out in ambient atmosphere, the resulting composite film has been annealed in an oven at 95 ℃ to fill the pores with the polymer. The reflection band of oxidized rugate PS/polystyrene composite film appears at 569 nm, shifted to longer wavelengths by 38 nm upon introduction of the polymer into the pores. Such a large red shift is due to an increase in the average refractive index of the multilayers, indicating the replacement of a

significant amount of empty pore volume with the polymers. Since one side of oxidized rugate PS films are coated with the polymers, the oxidized rugate PS matrix from the composite films can be easly removed in dilute aqueous HF solution. After removal of oxidized rugate PS from the composite film, the polymer replica has been successfully obtained and exhibits its reflection band at 534 nm, shifted to shorter wavelengths by 35 nm as shown in Figure 4. This blue shift indicates that the removal of oxidized rugate PS template by chemical dissolution results the decrease of refractive index.
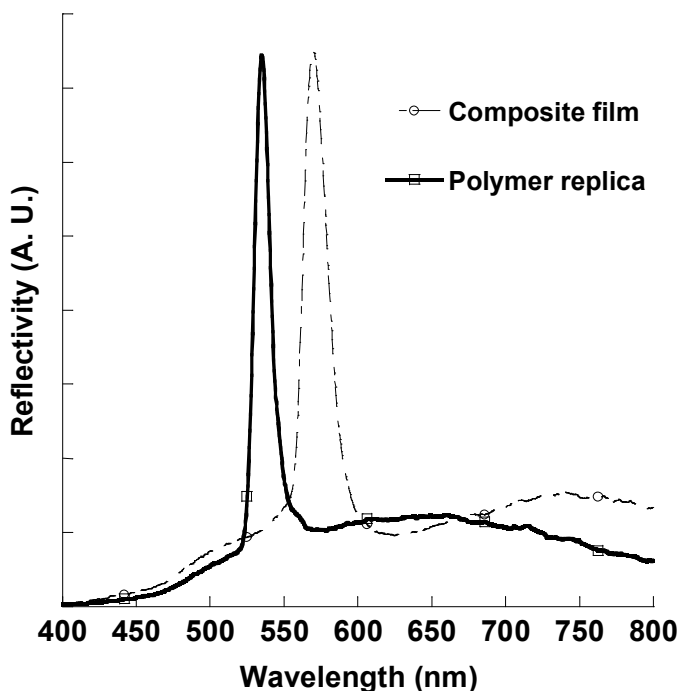
Figure 7.4. Optical reflectivity spectra of rugate PS/polymer composite film and polymer replica.

To determine the presence of silicon, XRD measurement for the rugate PS film

and polymer replica film has been investigated. Figure 5 shows the X-ray
diffraction pattern of samples prepared. The peak at about 69°, which can be seen
in Figure 5 (top), is attributed to the diffraction from the crystalline silicon of the
rugate PS film. However, the X-ray diffraction pattern of the polymer replica in
Figure 5 (bottom) indicates that the oxidized rugate PS template has been
completely removed from the composite films and no crystalline silicons are
remaining.
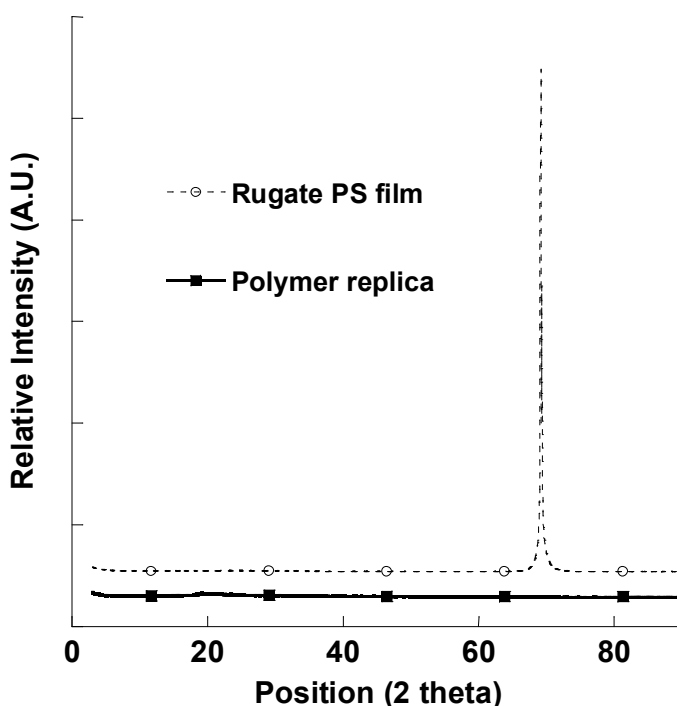
Figure 7.5. X-ray diffraction patterns of rugate PS film and photonic polymer
replica.

Photograph of rugate-structured polymer replica is shown in Figure 6 and
illustrates that its green color results from the reflection of the polymer replica.

This polystyrene replica exhibits a sharp reflection peak in the reflectivity spectrum and replicates the photonic feature of rugate PS master. The polymer replica is also highly flexible and displays significantly improved mechanical stability without apparent degradation. Its optical property is retained upon flexing.

Figure 7.6. Photograph of polymer replica showing a reflection band at 534 nm.
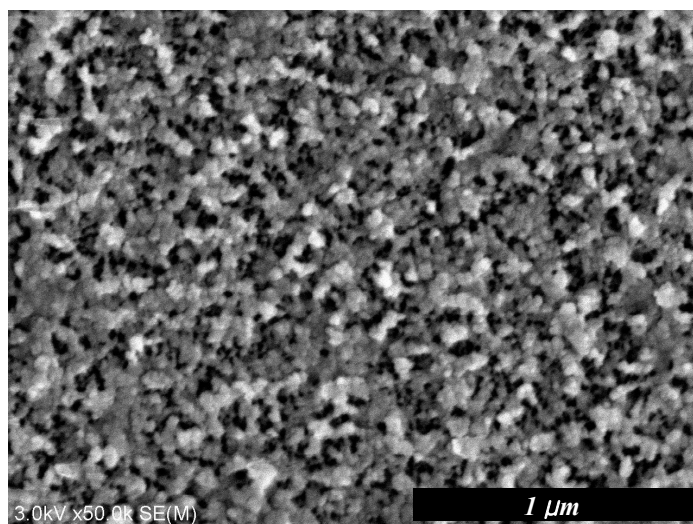
Figure 7.7. SEM image of polymer replica having photonic structure.

The surface morphology of polymer replica is obtained with cold FE-SEM and shown in Figure 7. FE-SEM image of rugate-structured polymer replica indicates that the surface of polymer film has a negative structure of rugate PS. Therefore, the polymer castings replicate the photonic feature and the nanostructure of rugate PS master.

It is interesting to note that the photonic band widths of replicas are about 14 nm which is much narrower than that of rugate PS master and the polymer replicas reported previously (ca.50 nm) [18]. These polymer replicas are stable in aqueous solutions for several days without any degradation and could be useful for a possible applications such as vapor senor, deformable and tunable optical filters, and bioresorbable materials.

7.4 Conclusion

The rugate-structured photonic polymer replica showing a reflectivity at 534 nm has been prepared by casting of polymer solution onto an oxidized porous silicon multilayer and then the chemical dissolution of oxidized rugate PS template from the polystyrene composite film. The photonic polymer replicas are robust and flexible. They exhibit an excellent reflectivity in reflection spectrum. The photonic band gaps of replicas are narrower than that of typical semiconductor quantum dots. X-ray diffraction pattern and SEM images indicate that the polymer replica replicates the photonic feature and the nanostructure of rugate PS master. The methods have been provided for the construction of photonic structures with polymers.

7.5 Reference

[1] A. Uhlir, *Bell System Tech.* **35**, 333 (1956).

[2] H. Sohn, S. Letant, M. J. Sailor, and W. C. Trogler, *J. Am. Chem. Soc.* **122**, 5399 (2000).

[3] J. M. Lauerhaass, and M. J. Sailor, *Science* **261**, 1567 (1993).

[4] V. S. Lin, K. Motesharei, K. S. Dancil, M. J. Sailor, and M. R. Ghadiri, *Science* 278, 840 (1997).

[5] M. Simion, I. Kleps, T. Neghina, A. Angelescu, M. Miu, A. Bragaru, M. Danila, E. Condac, M. Costache, and L. Savu, *J. Alloy. Compd.* 434, 830 (2007).

[6] S. Ilyas, T. Böcking, K. Kilian, P. J. Reece, J. Gooding, K. Gaus, and M. Gal, *Opt. Mater.* **29**, 619 (2007).

[7] M. A. Khan, M. S. Haque, H. A. Naseem, W. D. Brown, and A. P. Malshe, *Thin Solid Films* **332**, 93 (1998).

[8] S. E. Létant, S. Content, T. T. Tan, F. Zenhausern, and M. J. Sailor, *Sensor. Actuat. B- Chem.* **69**, 193 (2000).

[9] L. Zhai, A. J. Nolte, R. E. Cohen, and M. F. Rubner, *Macromolecules* **37**, 6113 (2004).

[10] P. C. Searson, J. M. Macaulay, and F. M. Ross, *J. Appl. Phys.* **72**, 253 (1992).

[11] C. Levy-Clement, A. Lagoubi, and M. Tomkiewucz, *J. Electrochem. Soc.* **141**, 958 (1994).

[12] B. J. Lee, S. Jang, and H. Sohn *Solid State Phenom.* **124**, 491 (2007).

[13] J. Park, S. Cho, Y. C. Ko, and H. Sohn, *J. Korean Phys. Soc.* **50**, 695 (2007).

[14] M. J. Sailor and J. R. Link, *Chem. Commum.* 1375 (2005).

[15] Y. Y. Li, V. S. Kollengode, and M. J. Sailor, *Adv. Mater.* **17**, 1249 (2005).

[16] M. S. Yoon, K. H. Ahn, R. W. Cheung, H. Sohn, J. R. Link, F. Cunin, and M. J. Sailor, *Chem. Commun.* 680 (2003).

[17] D. J. Lockwood, A. Wang, and B. Bryskiewicz, *Solid State Commun.* **89**, 587 (1994).

[18] Y. Y. Li, F. Cunin, J. R. Link, T. Gao, R. E. Betts, S. H, Reiver, V. Chin, S. N. Bhatia, and M. J. Sailor, *Science* **299**, 2045 (2003).

Chapter Eight
Photonic Polymer Replicas Based on Distributed Bragg Reflector Porous Silicon Template

8.1 Introduction

The development of new technology, which can achieve at nanometer scale, to build such a device is of great interest, because it is too complex to fabricate by using conventional lithographic method. Synthesis of nanostructured materials has emerged as a useful and versatile technique to provide the use of encoded materials for chemical and biological sensors [1]. high throughput screening, and controlled release drug delivery [2]. Multilayered PS is an attractive candidate for building nanostructured composite materials because the porosity and average pore size can be tuned by adjusting the electrochemical preparation conditions that allow the construction of photonic crystals [3,4]. DBR PS exhibits unique optical properties providing the reflection of a specific wavelength in the optical reflectivity spectrum. DBR PS has been typically prepared by applying a computer generated pseudo-square current waveform to the etch cell which results two distinct indices and exhibits photonic structure of Bragg filters [5-8]. The resulting DBR PS films can be lifted off from the silicon substrate to obtain a free-standing DBR PS films. For many applications, PS is limited by its chemical and mechanical stability because these free-standing films are very brittle. The use of flexible DBR PS/polymer composite materials [9] overcomes these issues and improves chemical and mechanical stability. However, these composite materials are not suitable for

the application of biological sensors *in vivo* due to the presence of silicon metal of the PS films. Therefore, biocompatible polymers having specific optical characteristics would be ideal for these applications. Here, we have prepared polystyrene replicas showing DBR photonic structure by casting of polystyrene solution onto an oxidized DBR PS. This provides the means for the construction of complex photonic structures with polymers.

8.2 Experimental

8.2.1 Preparation of DBR PS

DBR PS samples are prepared by electrochemical etch of heavily doped p^{++}-type silicon wafers (boron doped, polished on the (100) face, resistivity of 0.8-1.2mΩ-cm, Siltronix, Inc.). The etching solution consisted of a 3:1 volume mixture of aqueous 48% hydrofluoric acid (ACS reagent, Aldrich Chemicals) and absolute ethanol (ACS reagent, Aldrich Chemicals). DBR PS samples are prepared by using a computer-generated periodic square wave current. DBR PS samples exhibiting its reflectance at 557 nm have been prepared by using 5 mA-cm^{-2} for 82 s and 50 mA-cm^{-2} for 7 s with 20 repeats. The resulting DBR PS films have been obtained from the silicon substrate by an applying of electropolishing current at 490 mA-cm^{-2} for 2.5 min in a solution of 48% aqueous HF and ethanol (3:1 by volume), and then at 28 mA-cm^{-2} for 2.5 min in a solution of 48% aqueous HF and ethanol (1:30 by volume) to obtain a free-standing DBR PS films.

8.2.2 Preparation of Photonic Polymer Replicas

Free-standing DBR PS films are thermally oxidized in the furnace at 400 ℃ for 3 h. In a typical preparation, 4 g of polystyrene (Aldrich, Mw = 280,000) are dissolved in 20 mL of toluene (Fisher Scientific). The toluene solution has been cast on the top surface of oxidized DBR PS films. The resulting composite films have been annealed at 95 ℃ for 20 min. Then oxidized DBR PS matrix from the composite films has been removed in aqueous 8% HF solution.

8.2.3 Instrumentation and Data Acquisition

Optical reflectivity spectra were measured using a tungsten-halogen lamp and an Ocean Optics S2000 CCD spectrometer fitted with a fiber optic input. The reflected light collection end of the fiber optic was positioned at the focal plane of the optical microscope. Scanning electron microscope (SEM) images were obtained by a cold field emission scanning electron microscope (FE-SEM, S-4700, Hitachi). The surface characterization of oxidized DBR PS samples for chemical properties was achieved by fourier-transform infrared (FT-IR, Nicolet 5700). The presence of silicon has been determined by X-ray diffractometer (XRD, D/MAX-3C, Riguku Co.).

8.3 Results and Discussion

Multilayered porous silicon containing two distinct porosities has been successfully prepared by using a periodic galvanostatic electrochemical etch of crystalline silicon. The wavelength of a peak in the reflectivity spectrum is given by the following equation:

$$m\,\lambda_{Bragg} = 2n_i d_i$$

where m is the spectral order of the optical fringe, λ the wavelength, n_i the refractive index of the film, and d_i its thickness. DBR PS samples display a very sharp line at 557 nm with sidelobes around the reflectance peak in the optical reflectivity spectrum as shown in Figure 1. The spectral bands of DBR PS samples have a full-width at half-maximum (FWHM) of about 20 nm, whereas the narrowest quantum dot spectrum reported at this wavelength has a FWHM of 20 nm [10]. Free-standing DBR PS film has been obtained from the silicon substrate by an applying of electropolishing current in a solution of HF and ethanol. The reflectivity of free-standing DBR PS film occurs at the identical location. This film is thermally oxidized in the furnace at 450℃ for 2 h. The reflection spectrum for the oxidized DBR PS film shown in Figure 1 exhibits its reflectivity at 658 nm, shifted to shorter wavelengths by 54 nm due to the decrease of an average refractive index from silicon to silicon dioxide.
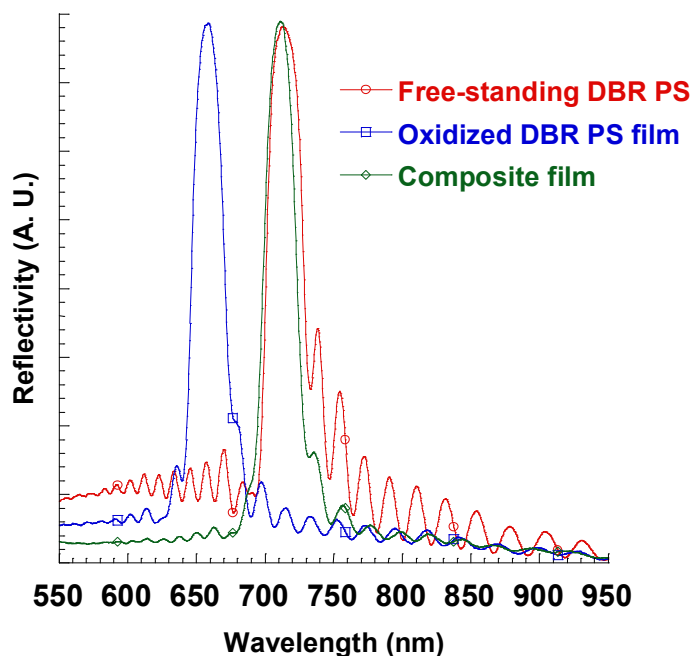
Figure 8.1. Optical reflectivity spectrum of free-standing DBR PS film, oxidized DBR PS film and DBR PS/polymer composite film

After the thermal oxidation of DBR PS film, the presence of silicon oxide has been determined by FT-IR measurement. The FT-IR spectrum of the oxidized DBR PS displays an absorption band assigned to Si-O stretching modes at 1200 cm^{-1}. Polystyrene has been dissolved in toluene and cast on the top surface of oxidized DBR PS film. After drying out in ambient atmosphere, the resulting composite film has been annealed to fill the pores with the polymer. The reflection band for oxidized DBR PS/polystyrene composite film appears at 711 nm, shifted to longer wavelengths by 53 nm upon introduction of the polymer. Such a large red shift is due to an increase in the average refractive index of the multilayers, indicating the replacement of a significant amount of empty pore volume with polymer. After

removal of oxidized DBR PS from the composite film, the polymer replica has been successfully obtained and exhibits its reflection band at 654 nm, shifted to shorter wavelengths by 57 nm as shown in Figure 2.
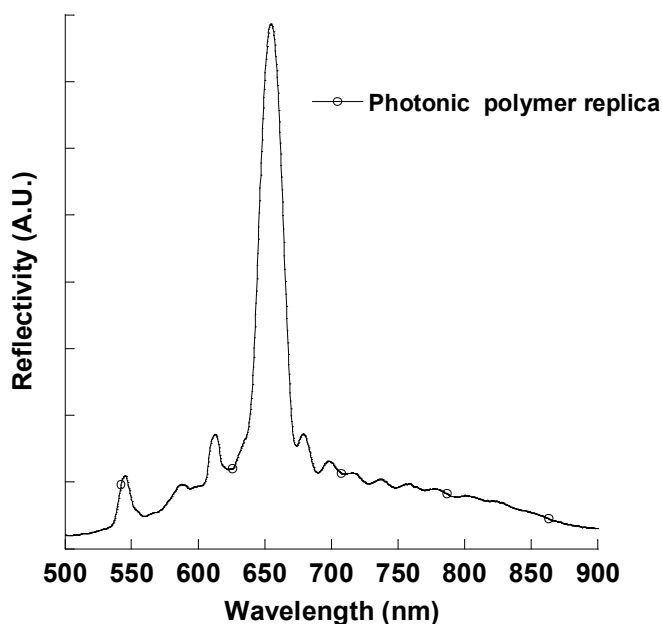
Figure 8.2. Optical reflectivity spectrum of photonic polymer replica based on DBR PS film.

This blue shift indicates that the removal of oxidized DBR PS template by chemical dissolution results the decrease of refractive index. XRD measurement indicates that the oxidized DBR PS has been completely removed from the composite films shown in Figure 3 [11].
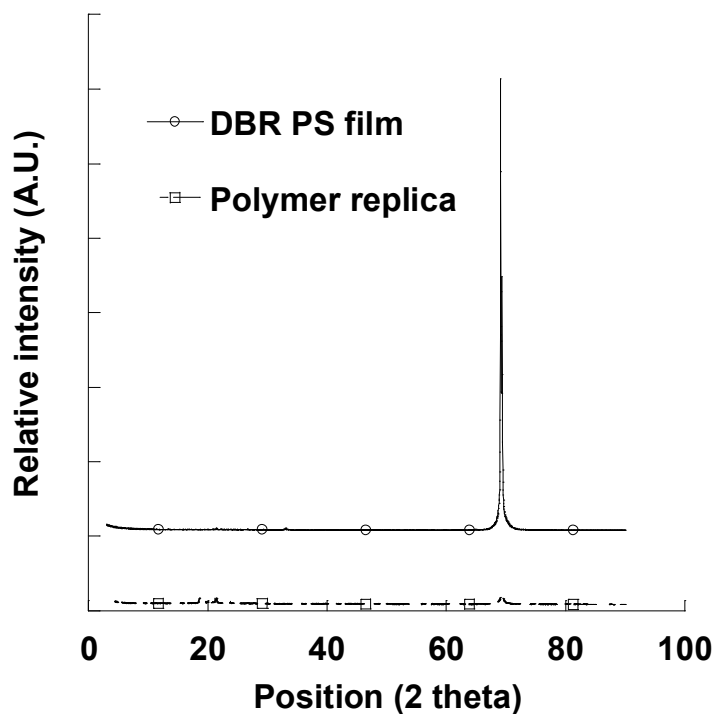
Figure 8.3. X-ray diffraction spectrum of DBR PS film and photonic polymer replica.

These polystyrene replicas exhibit a sharp reflection peak in the reflectivity spectrum and replicate the photonic feature and the nanostructure of DBR PS master. Optical characteristics of photonic polymer replicas indicate that the surface of polymer film has a negative structure of DBR PS. Photograph and FE-SEM image of DBR-structured polymer replicas are shown in Figure 4 and Figure 5.

Figure 8.4. Photograph of photonic polymer replica.
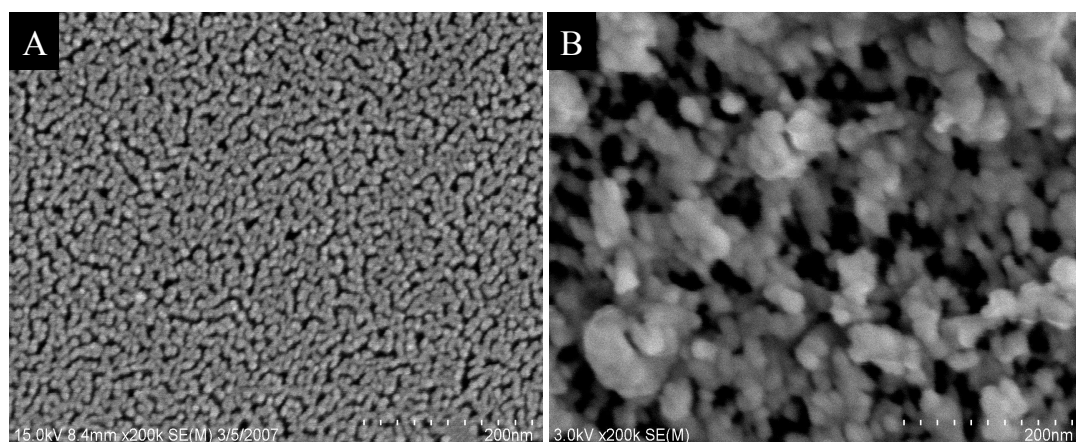
Figure 8.5. Surface SEM image of DBR PS (A) and polymer replica (B).

The photonic band gap of replica is 20 nm, which is narrower than that of DBR PS master and the polymer replicas from rugate PS master reported previously (ca.50 nm) [2]. These polymer replicas are stable in aqueous solutions for several days without any degradation and could be useful for a possible applications such as vapor senor, deformable and tunable optical filters, and bioresorbable materials.

8.4 Conclusion

The photonic polymer replicas showing a reflectivity at 654 nm have been prepared by the chemical dissolution of oxidized DBR PS template from the polystyrene composite film. The photonic band gaps of DBR-structured polymer replicas are narrower than that of polymer replicas from rugate PS master. The photonic polymer replicas are flexible and exhibit an excellent reflectivity in reflection spectrum. The methods have been provided for the construction of photonic structures with polymers.

8.5 Reference

[1] K. S. Dancil, D. P. Greiner, and M. J. Sailor, *J. Am. Chem. Soc.* **121**, 792 (1999).

[2] Y. Y. Li, F. Cunin, J. R. Link, T. Gao, R. E. Betts, S. H, Reiver, V. Chin, S. N. Bhatia, and M. J. Sailor, *Science* **299**, 2045 (2003).

[3] M. Qian, X. Q. Bao, L. W. Wang, X. Lu, J. Shao, and X. S. Chen, *J. Cryst. Growth* **292**, 347 (2006).

[4] V. Svrcek, T. Sasaki, Y. Shimizu, and N. Koshizaki, *Chem. Phys. Lett.* **429**, 483 (2006).

[5] B. J. Lee, S. G. Kim, and H. Sohn, *Key Eng. Mater.* **321**, 53 (2006).

[6] M. Cazzanelli, C. Vinegoni, and L. Pavesi, *J. Appl. Phys.* **85**, 1760 (1999).

[7] V. Lehmann, R. Stengl, H. Reisinger, R. Detemple, and W. Theiss, *Appl. Phys. Lett.* **78**, 589 (2001).

[8] C. Mazzoleni and L. Pavesi, *Appl. Phys Lett.* **67**, 2983 (1995).

[9] Y. Y. Li, V. S. Kollengode, and M. J. Sailor, *Adv. Mater.* **17**, 1249 (2005).

[10] M. Bruchez, M. Moronne, P. Gin, S. Weiss, and A. P. Alivisatos, *Science* **281**, 2013 (1998).

[11] V. Setzu, G. Lerondel, and R. Romestain, *J. Appl. Phys.* **84**, 3219 (1998).

Chapter Nine
Photonic Polymer Replicas Containing CdSe Nanoparticles Based on Porous Silicon

9.1 Introduction

The fabrication of new functional materials tailored with novel physical and chemical properties represents one of the most crucial challenges in modern materials science. Nanocomposite materials based on polymers composed with inorganic nanoparticles are particularly attractive [1]. Especially, the addition of semiconductor nanoparticles to polymer materials has led to markedly enhanced control of a wide range of technically important material properties from optoelectronic to mechanical properties [2]. The nano-crystal/polymer composites have the combined advantages of inorganic and organic materials, high quantum yields and flexible possibilities. However, studies on the optical properties of those nano-crystal/polymer composite materials are very limited.

Since the discovery of luminescence properties for PS in 1990 [3], it has been investigated for a variety of applications, such as chemical and biological sensors [4-6], medical diagnostics [7], optical band pass filters [8], micro chemical reactors [9, 10], and micro fuel cells [11, 12]. Its importance is due to its very high surface area and its unique photonic properties. PS is an attractive candidate for building photonic structures because the porosity and average pore size can be tuned by adjusting the electrochemical preparation conditions that allow the construction of photonic crystals. Optical devices based on multi-structured PS have

been brought to the attention of scientists [13-15]. However, porous silicons are limited by their chemical and mechanical stability for many applications, because these films are very brittle. To overcome these issues, polymer materials showing identical optical properties might be an alternative.

Fluorescent molecules and quantum dots have received much attention for use in high-throughput screening and bioassay applications [16-26]. These functional materials are related to photonic crystal structures nanoimprinted in a photoluminescent nanocomposite material based on polymer and highly luminescent semiconductor nanocrystals [27]. Composite materials containing inorganic nanocrystals are suitable for flexible and innovative fabrication processes, allowing for the micro- and nanometric patterning required for the manufacture of original devices for photonic and optoelectronic applications.

Recently, we introduced a fabrication method for photonic polymer replicas having the negative structure of multilayer PS [28]. This provides the means to construct complex photonic structures of polymers that are compatible with harsh environments and to improve chemical and mechanical stability. In this report, we describe a method for fabricating photonic polymer replicas containing CdSe nanoparticles. The photonic polymer replica with CdSe nanoparticles embedded in a polymer matrix exhibits both sharp reflection and a photoluminescence band. The replication process and the photonic features of the polymer replicas are described.

9.2 Experimental

9.2.1 Preparation of DBR PS

The PS samples were prepared by electrochemically etching heavily-doped p^{++}-type silicon wafers (boron doped, polished on the <100> face, resistivity of 0.8-1.2 mΩ·cm, Siltronix, Inc.). The etching solution consisted of a 3:1 volume mixture of 48% aqueous hydrofluoric acid (ACS reagent, Aldrich Chemicals) and absolute ethanol (ACS reagent, Aldrich Chemicals). A galvanostatic etch was carried out in a Teflon cell by applying 20 cycles of a two-electrode configuration with a Pt mesh electrode. DBR PS was prepared by using periodic square wave currents between 5 mA·cm^{-2} for 75 s and 50 mA·cm^{-2} for 2 s. The anodization current was supplied by a Keithley 2420 high-precision constant current source controlled by a computer to allow the formation of PS multilayers. To prevent the photogeneration of carriers, we performed the anodization in the dark. All the samples were then rinsed several times with ethanol and dried were under an Ar atmosphere prior to use. Free-standing PS films were obtained from the silicon substrate by applying as electropolishing current of 360 mA·cm^{-2} for 1 min in an ethanoic 37.5% aqueous HF solution and of 24 mA·cm^{-2} for 2 min in an ethanoic 3.3 % aqueous HF solution.

9.2.2 Synthesis of CdSe Nanoparticles

For the synthesis of CdSe nanoparticles, a mixture of 0.2 mmol of cadmium oxide (ACS reagent, Aldrich Chemicals), 0.8 mmol of stearic acid (ACS reagent,

Aldrich Chemicals), and 2 g of 1-octadecene (ODE, ACS reagent, Aldrich Chemicals) in a 25-mL three-neck flask was heated to about 200 ℃ to obtain a colorless clear solution. After this solution had been cooled to room temperature, 1.5 g of octadecylamine (ODA, ACS reagent, Aldrich Chemicals) and 0.5 g of trioctylphosphine oxide (TOPO, ACS reagent, Aldrich Chemicals) were added to the flask. Under argon flow, this mixture was reheated to 280 ℃. At this temperature, a selenium solution made by dissolving 2 mmol of Se in 0.472 g of tributylphosphine (TBP, ACS reagent, Aldrich Chemicals) and further diluting with 1.37 g of 1-octadecene was quickly achieved. The crystal growth temperature was then reduced to 250 ℃. Separation of the unreacted cadmium precursor from the nanocrystals was performed by repeated extraction of the reaction mixtures dissolved in hexane. An equal volume of methanol was used as an extraction solvent. The nanocrystals remained in the hexane/1-octadecene phase, and the unreacted precursors and excess amines were extracted into the methanol layer.
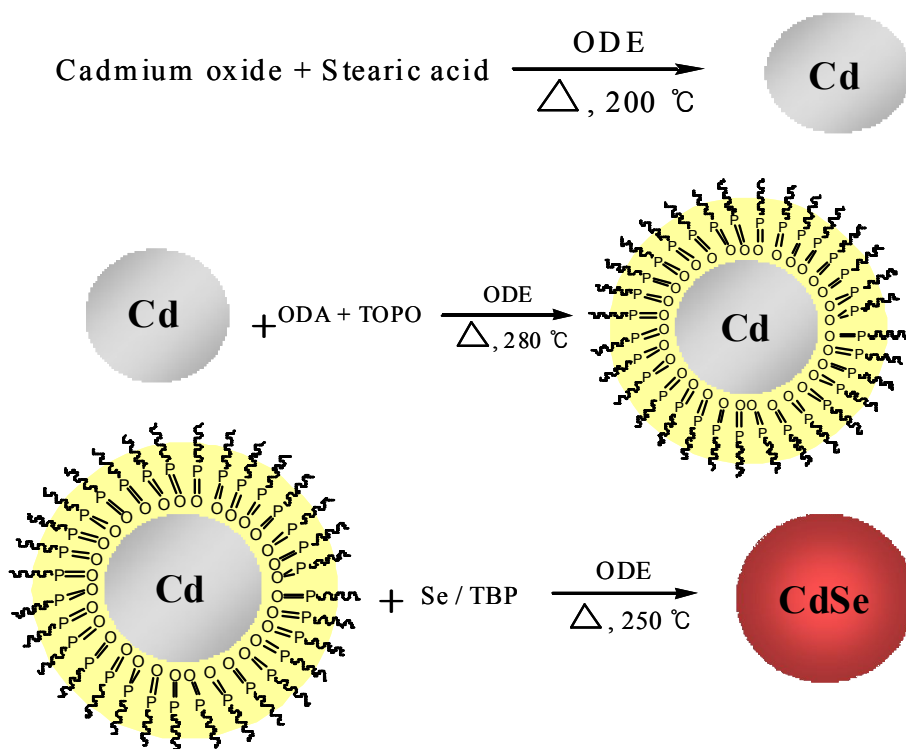
Scheme 9.1. Synthesis scheme of CdSe nanoparticles.

9.2.3 Photonic Polymer Replicas Containing CdSe Nanoparticles

Preparation of Photonic Polymer Replicas Containing CdSe Nanoparticles: Prepared free-standing DBR PS films were thermally oxidized in a furnace at 300℃ for 3 hrs. For the replicating solution, 3 g of PMMA (polymethylmethacrylate, Aldrich, Mw = 120,000) and prepared CdSe nanoparticles were dissolved in 20 mL of toluene (Fisher Scientific). The resulting mixtures were cast onto porous SiO_2 film and the samples were annealed in an oven at 95℃ for 1 hr. Then, the oxidized DBR PS matrix was removed from the composite films in 0.1 M aqueous NaOH for 3 hrs. After the removal of the oxidized DBR PS template by chemical dissolution, the polymer castings replicate the photonic features and the nanostructure of the master.

9.2.4 Instrumentation and Data Acquisition

UV-vis absorption and fluorescence emission spectra of CdSe nanoparticles were obtained using a Perkin-Elmer LS 50B luminescence spectrometer and Hewlett-Packard 8452A diode array spectrometer. The particle size of the CdSe particles was determined by using dynamic light scattering measurements (Particle Size Analyzer, Microtrac: UPA150). The optical reflectivity spectra were measured using a tungsten-halogen lamp and an Ocean Optics S2000 CCD spectrometer fitted with a fiber optic input. The reflected light collected at the end of the fiber optic was positioned at the focal plane of an optical microscope. FT-IR spectra were acquired with a Nicolet model 5700 FT-IR instrument in the diffuse reflectance mode (Spectra-Tech diffuse reflectance attachment). The FT-IR sample compartment

was purged with nitrogen before each acquisition. A DBR PS/polymer composite film and polymer replica were characterized by using an X-ray diffractometer (XRD, D/MAX-3C, Riguku Co.) with CuKα radiation (0.15406 nm). The XRD patterns were collected in the 2 theta range of 3 - 90° at room temperature.

9.3 Result and Discussion

Figure 1 shows both the absorption and the fluorescence spectra of the synthesized CdSe nanoparticles. The inset is a photograph of CdSe nanoparticles in a hexane solution under the illumination of an UV lamp. The absorption and the fluorescence spectra of CdSe nanoparticles exhibit peaks at 546 nm and 555 nm, respectively. The spectral band of the CdSe nanoparticles has a FWHM of 23 nm. The size distribution of CdSe nanoparticles, determined by using dynamic light scattering measurements, consisted of particles with diameter on the order of 11-13 nm (Figure 2).
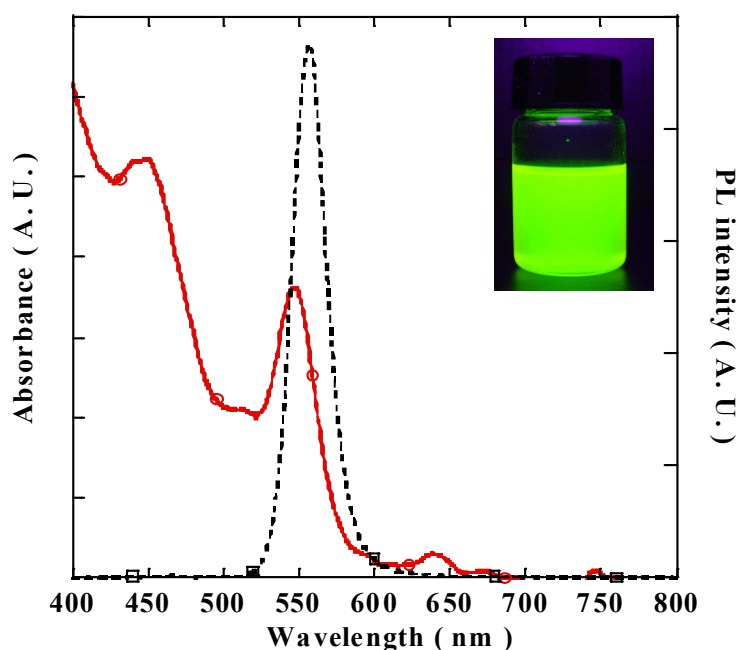
Figure 9.1. Absorption and fluorescence spectra of CdSe nanoparticles and photograph of the CdSe nanoparticle solution under an UV lamp.
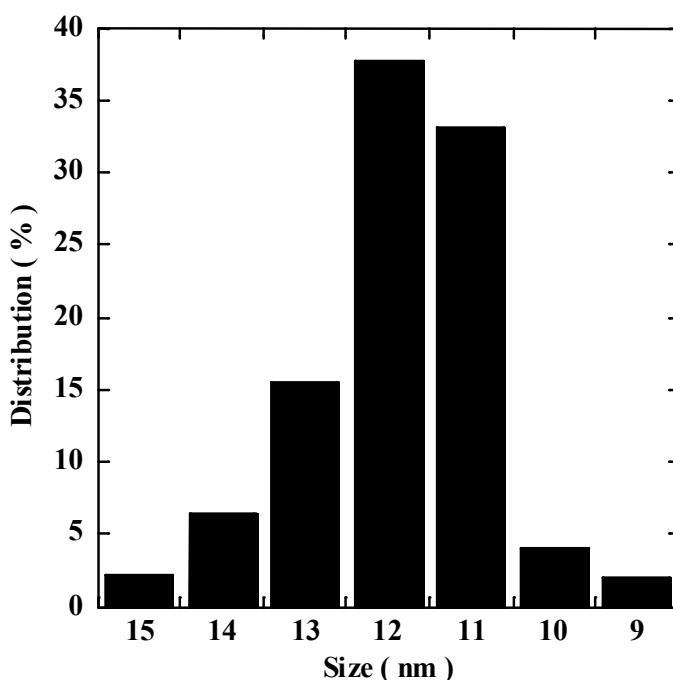
Figure 9.2. Size distribution histograms of CdSe nanoparticles.

DBR PS exhibits a high reflectivity band with a Bragg wavelength λ_{Bragg} that depends on the thicknesses of the layers (d_1, d_2) and the corresponding refractive indices (n_1, n_2). The mth order of the Bragg peak is given by

$$m \, \lambda_{Bragg} = 2(d_1 \, n_1 + d_2 \, n_2).$$

Typical etch parameters for the DBR PS structure involve a periodic square wave current between low and high current densities. The applied current densities for the fabrication of DBR PS varied between 5 and 50 mA·cm^{-2}. The dissolution times for a $\lambda/4$ layer of a Bragg structure were typically 75 s for low current and 2 s for high current. The reflection band had a narrow FWHM of 20 nm at 617

nm, as shown in Figure 3. The resulting DBR PS films were lifted off from the silicon substrates to obtain free-standing DBR PS films by applying of lift-off current in a solution of HF and ethanol. The reflection band of free-standing DBR PS film was placed at an identical location. The free-standing DBR PS films were very brittle when they were subjected to minor shear stresses. Thermal oxidation of these films was carried out in a furnace at 300 ℃ for 3 hrs. The reflection spectrum for the oxidized DBR PS film displayed reflectivity at 575 nm, which were shifted to shorter wavelengths by 42 nm, due to a decrease of the average refractive index from that for silicon to that for silicon dioxide.
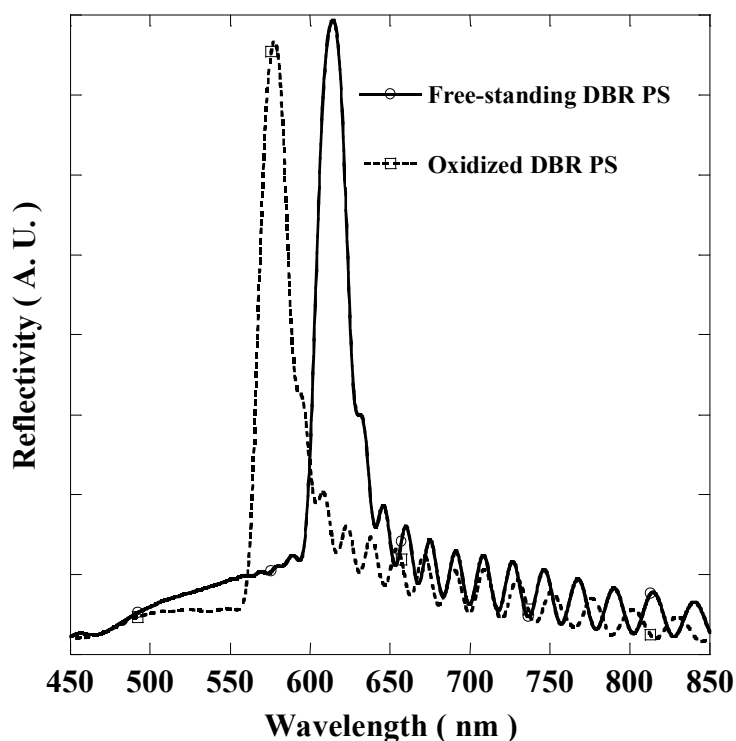
Figure 9.3. Optical reflectivity spectra of free-standing and of oxidized DBR PS films.

After the thermal oxidation of the DBR PS film, the presence of silicon oxide
was determined by using FT-IR measurement, as shown in Figure 4. The FT-IR
spectrum of a fresh DBR PS film displayed vibrational bands in the fingerprint
region of the spectrum. $\cup$(Si-H) and δ(Si-H) vibrations associated with surface
Si-H species were also apparent at 2117 and 941 cm^{-1}, respectively. The oxidized
DBR PS film exhibited vibrational bands characteristic of the $\cup$(OSi-H), δ
(OSi-H), and $\cup$(Si-O) vibrational modes were observed at 2270, 881, and 1070
cm^{-1}, respectively.
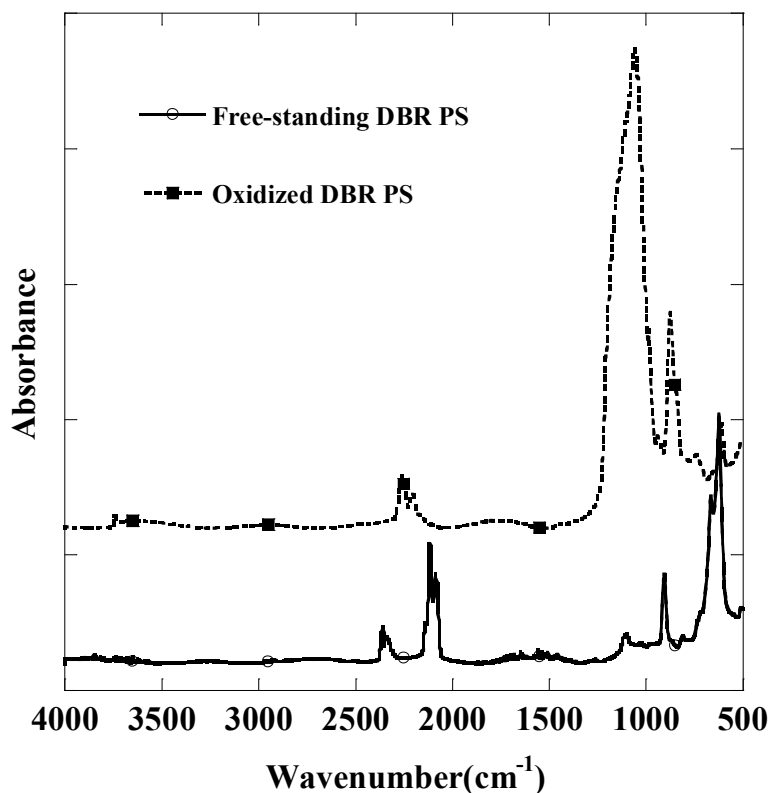
Figure 9.4. FT-IR spectra of free-standing and of oxidized DBR PS films.

The PMMA solution containing CdSe nanoparticles was cast on the top surface of the oxidized DBR PS film. After drying in an ambient atmosphere, the resulting composite film was annealed in an oven at 95℃ to fill the pores with the polymer. Since one side of the oxidized DBR PS films were coated with the polymer, the oxidized DBR PS matrix from the composite films could be removed in a dilute aqueous NaOH solution. To determine the absence of silicon, we performed XRD measurements for the DBR PS film and the polymer replica film. Fig. 5 shows the X-ray diffraction patterns of the prepared samples. The peak at about 69°, which can be seen in Figure 5 (top), was attributed to the diffraction from crystalline silicon in the DBR PS film. However, the X-ray diffraction pattern of the polymer replica in Figure 5 (bottom) indicates that the oxidized DBR PS template was completely removed from the composite films and that no crystalline silicon was remaining.
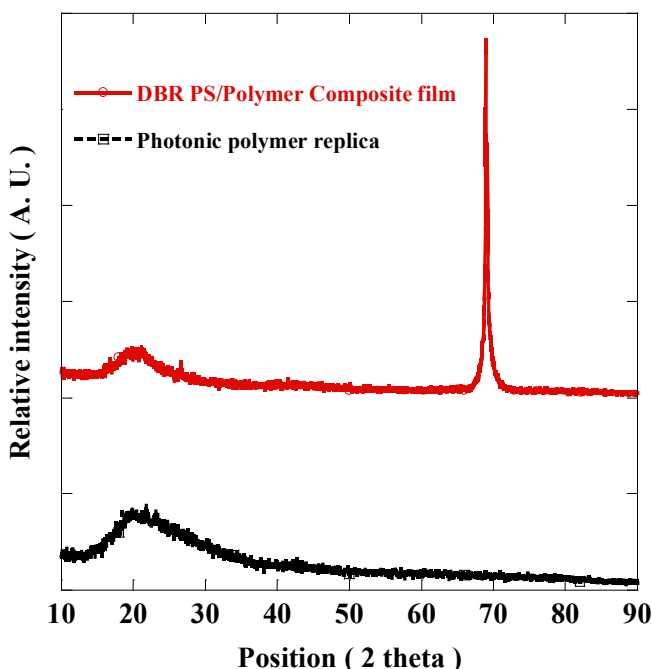
Figure 9.5. X-ray diffraction patterns of a DBR PS/polymer composite film and of its photonic polymer replica.

After removal of the oxidized DBR PS from the composite film, the polymer replica exhibited a reflection band at 571 nm and an emission band at 560 nm when excited at 380 nm, as shown in Figure 6 (A). A photograph of the photonic polymer replica containing CdSe nanoparticles is shown in Figure 6 (B, top) and its exhibits a green color due to the reflection of the polymer replica. This polymer replica exhibits a sharp reflection peak in the reflectivity spectrum and replicates the photonic feature of DBR PS master. The polymer replica was also highly flexible and displayed a significantly improved mechanical stability without apparent degradation. Its optical properties were retained upon flexing. Also, the photograph

of the polymer replica under an UV lamp, shown in Figure 6 (B, bottom), illustrates that its green color results from the photoluminescence of the polymer replica. This method provides a general means of fabricating a photonic polymer replica embedded with nanocrystal particles by using a porous-silicon multilayer and polymer materials. The nanocomposite polymer replicas possessed stable spectral features and increased stability to corrosion.
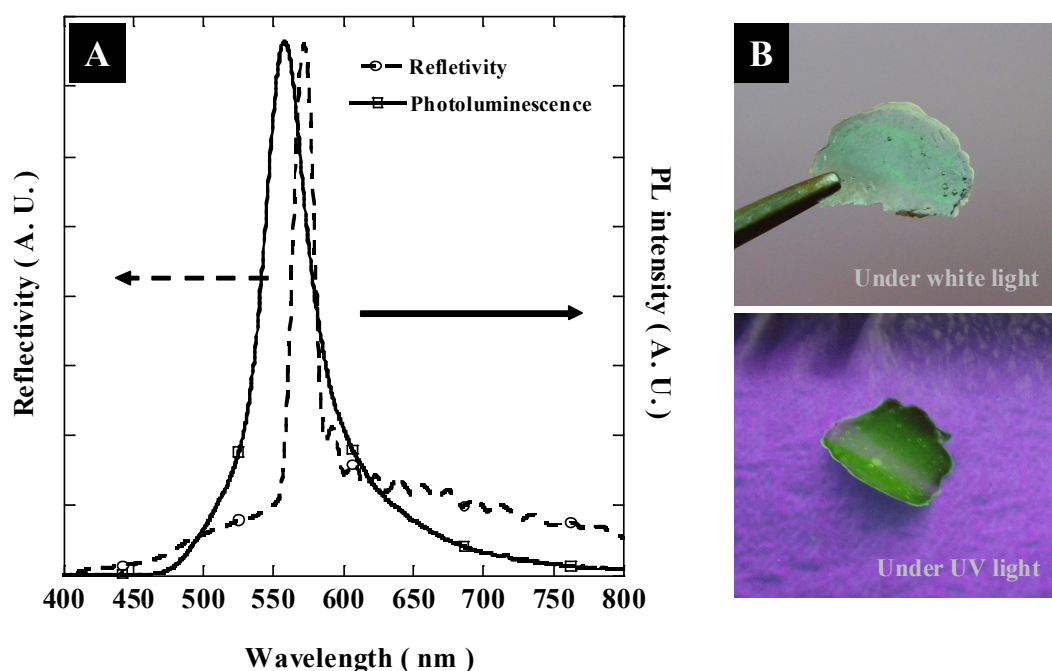
Figure 9.6. (A) PL and reflectivity spectra of the photonic polymer replica containing CdSe nanoparticles, (B) Photograph of the photonic polymer replica, showing a green light reflection (top) under white light and a green light emission (bottom) under an UV lamp.

9.4 Conclusion

Bragg-structured photonic polymer replicas showing reflectivity at 571 nm and photoluminescence at 560 nm were prepared by casting a polymer solution containing CdSe nanoparticles onto an oxidized porous silicon multilayer and then chemically dissolving the oxidized DBR PS template from the PMMA composite film. The photonic polymer replicas were robust and flexible. They exhibited excellent reflectivity in the reflection spectrum and photoluminescence from the CdSe nanoparticles. The X-ray diffraction pattern indicates that the polymer replica replicates the photonic features and the nanostructure of rugate PS master. Thus, replicating methods based on DBR PS have been provided for the construction of photonic structures with polymers.

9.5 Reference

[1] A. C. Balazs, T. Emrick, and T. P. Russell, *Science* **314**, 1107 (2006).

[2] E. T. Thostenson, C. Y. Li, and T. W. Chou, *Compos. Sci. Technol.* **65**, 491 (2005).

[3] L.T. Canham, *J. Appl. Phys. Lett.* **57**, 1046 (1990).

[4] H. Sohn, S. Letant , M. J. Sailor, and C. Trogler, *J. Am. Chem. Soc.* **122**, 5399 (2000).

[5] C. Pacholski, M. Sartor, M. J. Sailor, F. Cunin, and G. M. Miskelly, *J. Am. Chem. Soc.* **127**, 11636 (2005).

[6] V. S. Lin, K. Motesharei, K. S. Dancil, M. J. Sailor, and M. R. Ghadiri, *Science* **278**, 840 (1997).

[7] Y. Y. Li, F. Cunin, J. R. Link, T. Gao, R. E. Betts, S. H, Reiver, V. Chin, S. N. Bhatia, and M. J. Sailor, *Science* **299**, 2045 (2003).

[8] S. Ilyas, T. Böcking, K. Kilian, P. J. Reece, J. Gooding, K. Gaus, and M. Gal, *Opt. Mater.* **29**, 619 (2007).

[9] M. S. Yoon, K. H. Ahn, R. W. Cheung, H. Sohn, J. R. Link, F. Cunin, and M. J. Sailor, *Chem. Commun.* 680 (2003).

[10] C. A. Canaria, M. Huang, Y. Cho, J. L. Heinrich, L. I. Lee, M. J. Shane, R. C. Smith, M. J. Sailor, and G. M. Miskelly, *Adv. Funct. Mater.* **12**, 495 (2002).

[11] C. C. Striemer and P. M. Fauchet, *Phys. Stat. Sol.* **197**, 502 (2003).

[12] S. E. Létant, S. Content, T. T. Tan, F. Zenhausern, and M. J. Sailor, *Sensor. Actuat. B- Chem.* **69**, 193 (2000).

[13] F. Cunin, T. A. Schmedake, J. R. Link, Y. Y. Li, J. Koh, S. N. Bhatia, and M. J. Sailor, *Nat. Mater.* **1**, 39 (2002).

[14] J. Park, S. Cho, Y. C. Ko, and H. Sohn, *J. Korean Phys. Soc.* **50**, 695

(2007).

[15] S. Jang, Y. Koh, J. Kim, and H. Sohn, *J. Korean Phys. Soc.* **52**, 212 (2008).

[16] V. H. Colvin, M. C. Schlamp, and A. P. Alivisatos, *Nature* **370**, 354 (1994).

[17] M. Nirmal, B. O. Dabbousi, M. G. Bawendi, J. J. Macklin, J. K. Trautman, T.D. Harris, and F. E. Brus, *Nature* **383**, 802 (1996).

[18] M. A. Hines and P. GnyotSionnest, *J. Phys. Chem.* **100**, 468 (1996).

[19] M. Kuno, J. K. Fee, B. O. Dabbousi, F. V. Mikulec, and M. G. Bawendi, *J. Chem. Phys.* **106**, 9869 (1997).

[20] B. O. Dabbousi, J. RodiriguezViejo, F. V. Mikulec, J. R. Heine, H. Mattoussi, R. Ober, K. F. Jensen, and M. G. Bawendi, *J. Phys. Chem.* **101**, 9463 (1997).

[21] F. V. Mikulec, M. Kuno, M. Bennati, D. A. Hall, R. G. Griffin, and M. G. Bawendi, *J. Am. Chem. Soc.* **122**, 2532 (2000).

[22] C. B. Murray, C. R. Kagan, and M. G. Bawendi, *Science* **270**, 1335 (1995).

[23] J. R. Heath, R. S. Williams, J. J. Shiang, S. J. Wind, J. Chu, C. Demic, W. Chen, C. L. Stanis, and J. J. Bucchignano, *J. Phys. Chem.* **100**, 3144 (1996).

[24] C. P. Collier, R. J. Saykally, J. J. Shing, S. E. Henrichs, and J. R. Heath, *Science* **277**, 1978 (1997).

[25] C. A. Mirkin, R. L. Letsinger, R. C. Mucic, and J. J. Storhoff, *Nature* **382**, 607 (1996).

[26] A. P. Alivisatos, K. P. Johnsson, X. G. Peng, T. E. Wilson, C. J. Loweth, M. P. Bruchez, and P. G. Schultz, *Nature* **382**, 609 (1996).

[27] M. Tamborra and M. Striccoli, *Small* **3**, 822 (2007).

[28] J. Kim, Y. Koh, S. Jang, Y. C. Ko, H.-G. Woo, and H. Sohn, *J. Nanosci. Nanotechnol.* **7**, 4165 (2007).

Chapter Ten

Reflective and Magnetic Properties of Photonic Polymer Composite Materials Based on Porous Silicon and Magnetite Nanoparticles

10.1 Introduction

The fabrication of new multi-functional materials represents one of the most crucial challenges in modern materials science because these materials have improved combinations of physical and chemical properties as compared to their component materials. The Nano-crystal/polymer composites materials, based on polymers composed with nanoparticles, are particularly attractive due to the combined advantages of inorganic and organic materials, high yields and flexible possibilities [1,2]. The addition of nanoparticles to polymer materials has led to markedly enhanced control of a wide range of technically important material properties, from optoelectronic to mechanical properties [3].

The composite materials made from nanosized magnetic particles and polymers are the most interesting and challenging areas of current scientific research. Magnetic materials such as magnetites have been studied or used for a wide range of applications including magnetic recording, media, ferro-fluids, magnetic cell separation, MRI contrast agents, and environmental remediation [4,5]. However, incoporated studies on the optical and magnetic properties of those nano-crystal/polymer composite materials are very limited.

PS has been investigated for a variety of applications such as chemical and biological sensors, medical diagnostics, optical band pass filters, micro chemical reactors, and micro fuel cells [6-11]. Its importance is due to very high surface area as well as their unique photonic properties. PS was an attractive candidate for building photonic structure, because the porosity and average pore size can be tuned by adjusting the electrochemical preparation conditions that allow the construction of photonic crystals [12]. Also, the rugate PS is a kind of interference filter characterized by a continuous sinusoidal index variation in the direction perpendicular to the film plane. It shows a high reflectivity in a specific range of wavelength [13-14]. By adjusting the electrochemical etching conditions, such as the alternating current density, time and HF concentration, the morphology and the porosity of PS multilayer can be easily controlled. However PS is limited by their chemical and mechanical stability for many applications, because these films are very brittle [15]. To overcome these issues, polymer materials showing identical optical properties might be an alternative [16-18].

Photonic polymer composite materials are related on the optical characterization of photonic crystal structures nanoimprinted in a magnetic composite material based on polymer and magnetite nanocrystals. The blending of molten polymers and inorganic nanoparticles can yield a new class of materials where nanoscale magnetic particles are dispersed within the polymer matrix. Optical polymer materials containing magnetic nanocrystals are suitable for flexible and innovative new technique devices in photonic and magneto-optic applications.

Recently, we have been introduced the fabrication method of photonic polymer replicas having a negative structure of multilayer PS [19,20]. This provides the means for the construction of complex photonic structures of polymers that are compatible with harsh environments and improves chemical and mechanical stability.

In this report, we describe a method for the fabrication of photonic polymer composite materials containing reflective and magnetic properties. This photonic polymer composite material with magnetite nanoparticles embedded in polymer matrix exhibits both extraordinary reflection band and magnetic property. These functional composite materials are suitable for flexible and innovative fabrication processes, allowing for replicating required for the manufacture of original devices in photonic and optoelectronic applications.

10.2 Experimental

10.2.1 Preparation of Rugate PS

Samples were prepared by an electrochemical etch of heavily doped p^{++}-type silicon wafers (boron doped, <100> oriented, resistivity of 0.8-1.2 mΩ-cm, Siltronix, Inc.). The etching solution consisted of a 3:1 volume mixture of aqueous 48% hydrofluoric acid (ACS reagent, Aldrich Chemicals) and absolute ethanol (ACS reagent, Aldrich Chemicals). Rugate PS samples were prepared by using a computer-generated sinusoidal current waveform with limits of 11.5 to 34.6 mA/cm^2, 100 repeats, and periods on the order of 41 Hz depending on the desired wavelength of maximum reflectivity. The anodization current was supplied by a Keithley 2420 high-precision constant current source which was controlled by a computer to allow the formation of PS multilayers. To prevent the photogeneration of carriers, the anodization was performed in the dark. All samples were then rinsed several times with ethanol and dried under Ar atmosphere prior to use. Free-standing rugate PS films were obtained from the silicon substrate by an applying of electropolishing current at 360 mA/cm^2 for 1 min in an ethanoic 37.5% aqueous HF solution, and then at 24 mA/cm^2 for 2 min in ethanoic 3.3% aqueous HF solution.

10.2.2 Synthesis of Magnetite Nanoparticles

Typical synthesis of magnetite nanocrystals, a solution of 10 mmol FeCl$_3$·6H$_2$O in 100 mL 2-pyrrolidone was first purged with nitrogen to remove oxygen and

then heated to the boiling point of 2-pyrrolidone. Samples were taken after the mixture was refluxed for 12 h, and then cooled to room temperature. A threefold volume of methanol/diethyl ether (1:3) was added to precipitate the nanoparticles [21].
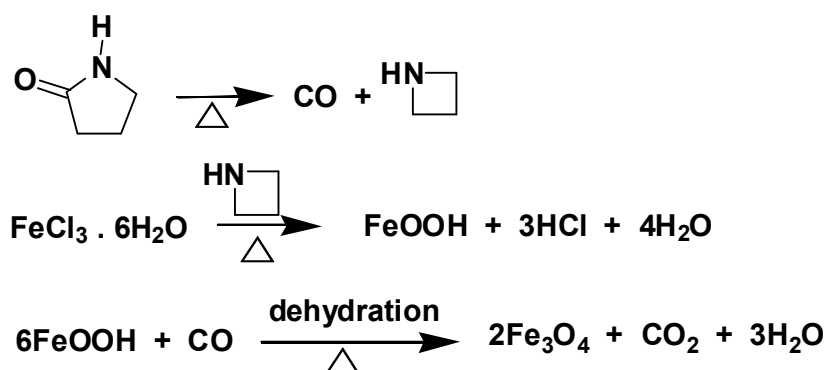
Scheme 10.1. Synthesis scheme of magnetite nanoparticles (Fe$_3$O$_4$).

10.2.3 Preparation of Photonic Polymer Composite Materials

Free-standing rugate PS films were thermally oxidized in the furnace at 300 ℃ for 3 hrs. For the replicating solution, 3 g of polystyrene (Aldrich, Mw = 280,000) and prepared magnetite nanoparticles were dissolved in 20 mL of toluene (Fisher Scientific). Resulted mixture solutions were cast onto the porous SiO$_2$ films and the samples were annealed in an oven at 95 ℃ for 1 hr. Then oxidized rugate PS matrix from the composite films were removed in aqueous 8% HF solution for 12 h. After the removal of the oxidized rugate PS template by chemical dissolution, the polymer castings replicate the photonic features and the nanostructure of the master.

10.2.4 Instrumentation and Data Acquisition

The anodization current was supplied by a Keithley 2420 high-precision constant current source which was controlled by a computer to allow the formation of PS multilayers. Optical reflectivity spectra were measured using a tungsten-halogen lamp and an Ocean Optics S2000 CCD spectrometer fitted with a fiber optic input. The reflected light collection end of the fiber optic was positioned at the focal plane of the optical microscope. TEM images of the sythesised magnetite nanoparticles were obtained using a Tecnai F20 transmission electron microscope. Samples for TEM analysis were prepared by dip-coating a solution of a sample on formvar/carbon-film Cu grids (20 mesh, 3 mm). The average particle size and distribution were determined based on the measurement of at least 100 particles. The morphology of rugate PS film and photonic polymer composite material were observed with cold field emission scanning electron microscope (FE-SEM, S-4700, Hitachi). Magnetic properties of polymer replica containing magnetite nanoparticles were investigated using a Quantum Design MPMS5 SQUID magnetometer with fields up to 6000 Oe at 300 K.

10.3 Results and Discussion

Figure 1(A) showed TEM image of the synthesized magnetite nanoparticles. The particle size was measured to be approximately 10 nm. Figure 1(B and C) illustrated selected lattice fringes and area electron diffraction (SAED) pattern of magnetite nanoparticle. The nanoparticles appeared to be of uniform size but there are large numbers of particles that were aggregated. Selected lattice fringes and area electron diffraction showed a diffraction pattern consistent with a crystalline magnetite nanoparticle structure.
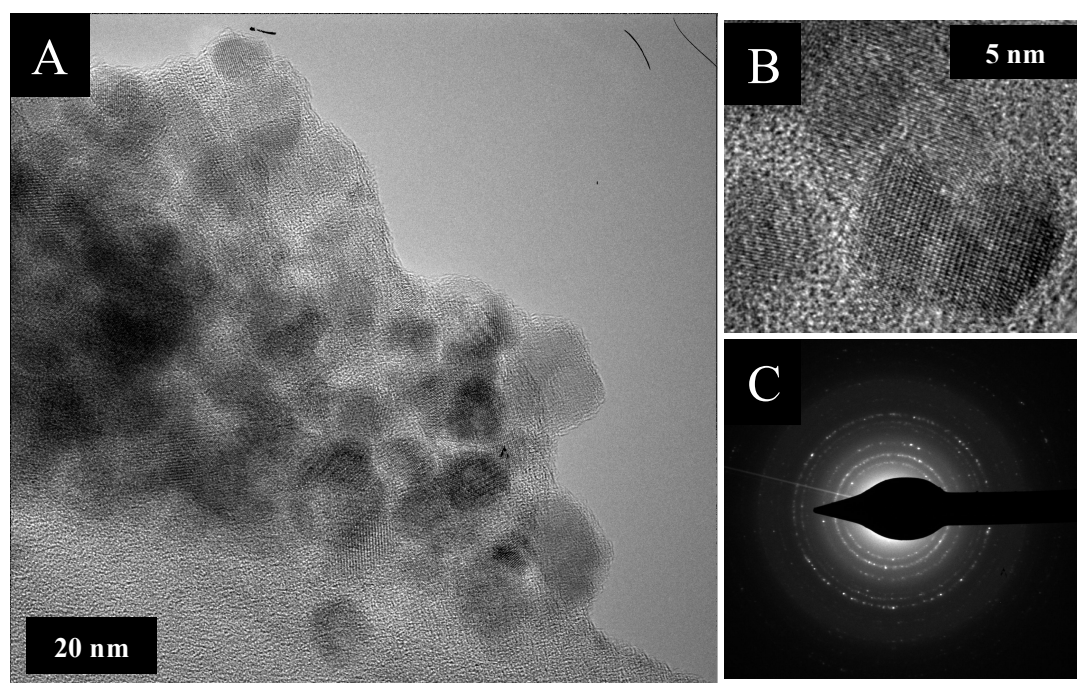

Figure 10.1. TEM image of magnetite nanoparticles (Fe$_3$O$_4$).

Rugate PS was successfully prepared using a periodic galvanostatic electrochemical etch of crystalline silicon by applying a sine wave current. The applied current density was modulated with a pseudo sine wave to generate a periodically varying porosity gradient. Rugate PS samples displayed a very sharp reflection line at 667 nm without sidelobes around the reflectance peak in the optical reflectivity spectrum as shown in Figure 2. The spectral band of rugate PS sample had a FWHM of about 15 nm, which was much narrower than that of fluorescence spectrum obtained from a fluorescent organic molecules or quantum dot.22 FE-SEM image of rugate PS as shown in Figure 3(A) indicated that the prepared rugate PS had cylindrical mesopores with the average pore size of 10 nm.

The resulting rugate PS films were lifted off from the silicon substrate to obtain a free-standing rugate PS film by an applying of lift-off current. Free-standing rugate PS films were very brittle when these films are subjected to minor shear stresses. Thermal oxidation of these films was carried out in the furnace. The reflection band of the oxidized rugate PS film displayed its reflectivity at 608 nm shifted to shorter wavelengths by 59 nm due to the decrease of an average refractive index from silicon to silicon dioxide as shown in Figure 2. Polystyrene solution containing magnetic magnetite nanocrystals cast on the top surface of oxidized rugate PS film. After drying out in ambient atmosphere, the resulting composite film was annealed in an oven to fill the pores with the polymer. The reflection band of oxidized rugate PS/polystyrene composite film appeared at 680 nm, shifts to longer wavelengths by 72 nm upon introduction of the polymer into the pores. Such a large red shift was due to an increase in the average refractive index of the multilayers, indicating the replacement of a significant amount of empty pore volume with the polymers as shown in Figure 2. Since one side of oxidized rugate PS films were coated with the polymers containing magnetic

magnetite nanocrystals, the oxidized rugate PS matrix from the composite films could be easily removed in dilute aqueous HF solution. After removal of oxidized rugate PS from the composite film, the polymer replicas containing magnetite nanoparticles were successfully obtained and exhibited a sharp reflection resonance at 612 nm with FWHM of 18 nm in the reflectivity spectrum, shifted to shorter wavelengths by 68 nm from the composite film as shown in Figure 2. Photonic polymer replica containing magnetite nanoparticles replicated the photonic feature of rugate PS master. This blue shift indicates that the removal of oxidized rugate PS template by chemical dissolution results the decrease of refractive index.
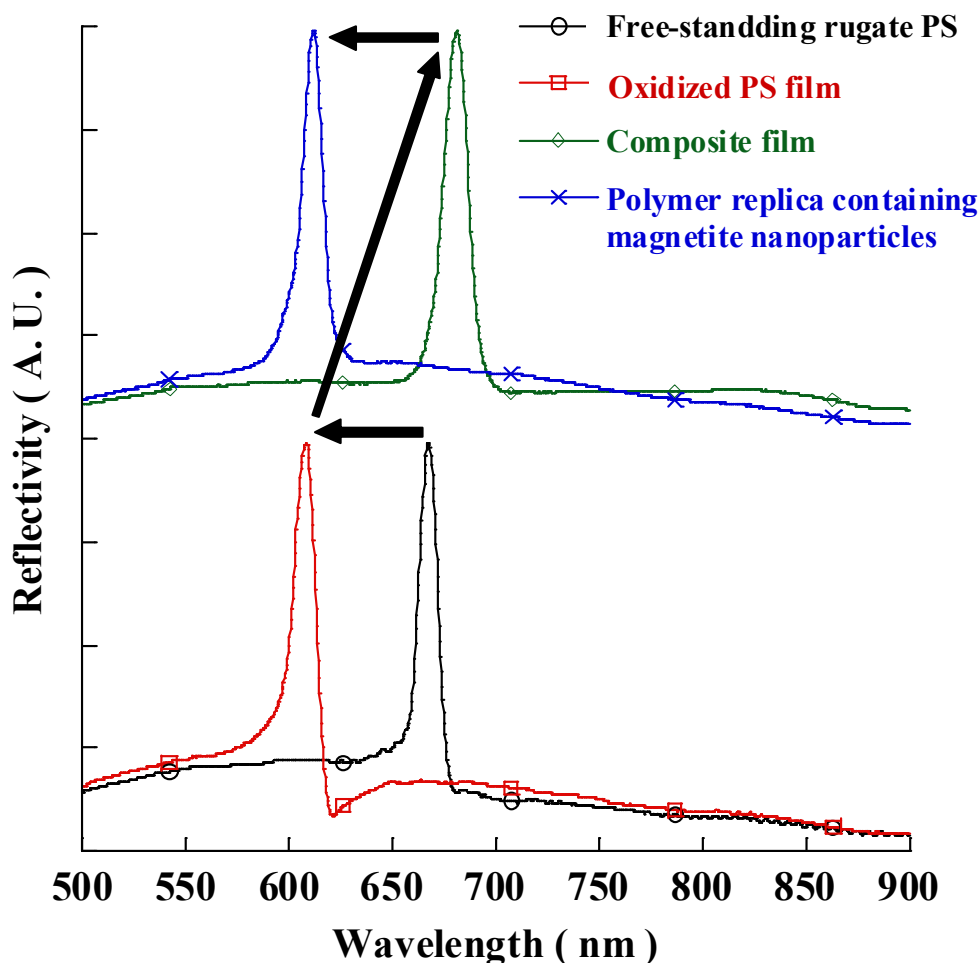
Figure 10.2. Optical reflectivity spectra of free-standing rugate PS film, oxidized rugate PS, oxidized rugate PS/polymer composite film, and polymer replica containing magnetite nanoparticles during the fabrication process.

The surface morphology of photonic polymer replica containing magnetite nanoparticles were obtained with cold FE-SEM and shown in Figure 3(B). FE-SEM image of rugate-structured photonic polymer replica containing magnetite

nanoparticles indicated that the surface of polymer film had a negative structure of rugate PS. Therefore, the polymer replica containing magnetite nanoparticles replicated the nanostructure of rugate PS master.
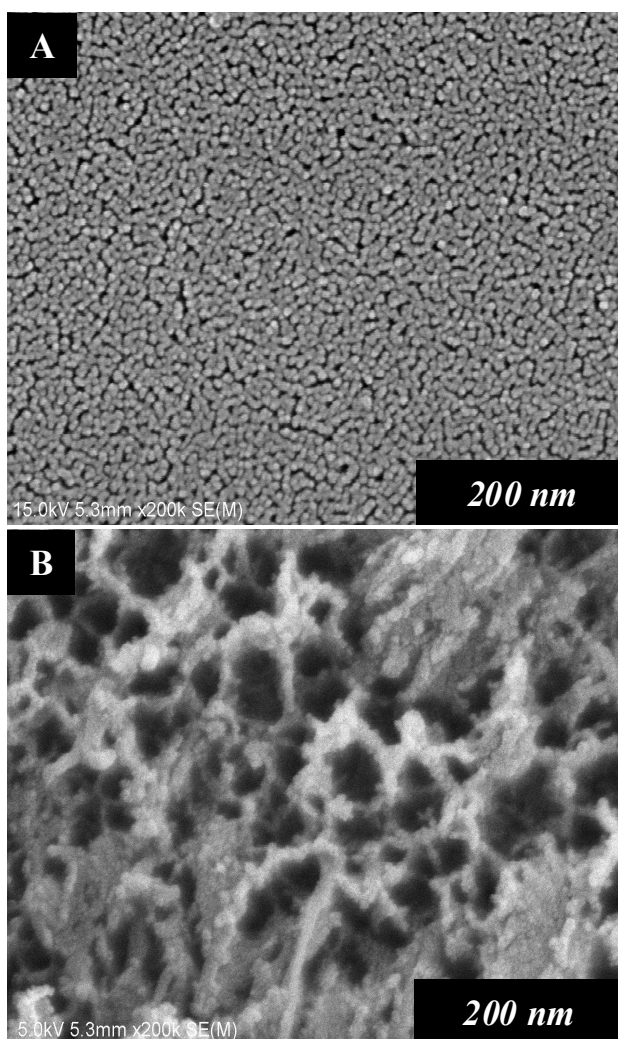
Figure 10.3. SEM image of rugate PS and polymer replica containing magnetite nanoparticles.

Photonic polymer replicas containing magnetite nanoparticles replicated a photonic feature of rugate PS in the reflectivity spectrum as well as a magnetic property of magnetite nanoparticles in SQUID magnetometry. Photograph of photonic polymer replica containing magnetite nanoparticles was shown in Figure 4(A) and illustrated that its red color resulted from the reflection of the polymer replica. The photonic polymer replica containing magnetite nanoparticles were also highly flexible and displayed significantly improved mechanical stability without apparent degradation of optical characteristics. Its optical property was retained upon flexing. The magnetic properties of the polymer replicas containing magnetite nanoparticles were studied at room temperature by SQUID magnetometry as shown in Figure 4(B). It was reported that the saturation magnetization were 59 emu/g for 12 nm magnetite nanoparticles.[21] The saturation magnetization was depended on the size of magnetite nanoparticles as well as the concentration of magnetite nanoparticles in the polymer matrix. The saturation magnetization of the polymer replica containing magnetite nanoparticles was very lower than that of the pure magnetite nanoparticles due to the lower concentration of magnetite nanoparticles in the polymer matrix. Quantification of the amount of magnetite nanoparticles infused into polymer matrix and the optimum condition of magnetite loading as MRI contrast agents is currently under investigation.

This method provided a general means of fabricating photonic polymer replica embedded magnetic magnetite nanoparticles from a porous-silicon multilayer and polymer materials. These polymer replicas are stable in aqueous solutions for several days and could be useful for a wide range of applications including magnetic recording, media, ferro-fluids, magnetic cell separation, MRI contrast agents, and environmental remediation.
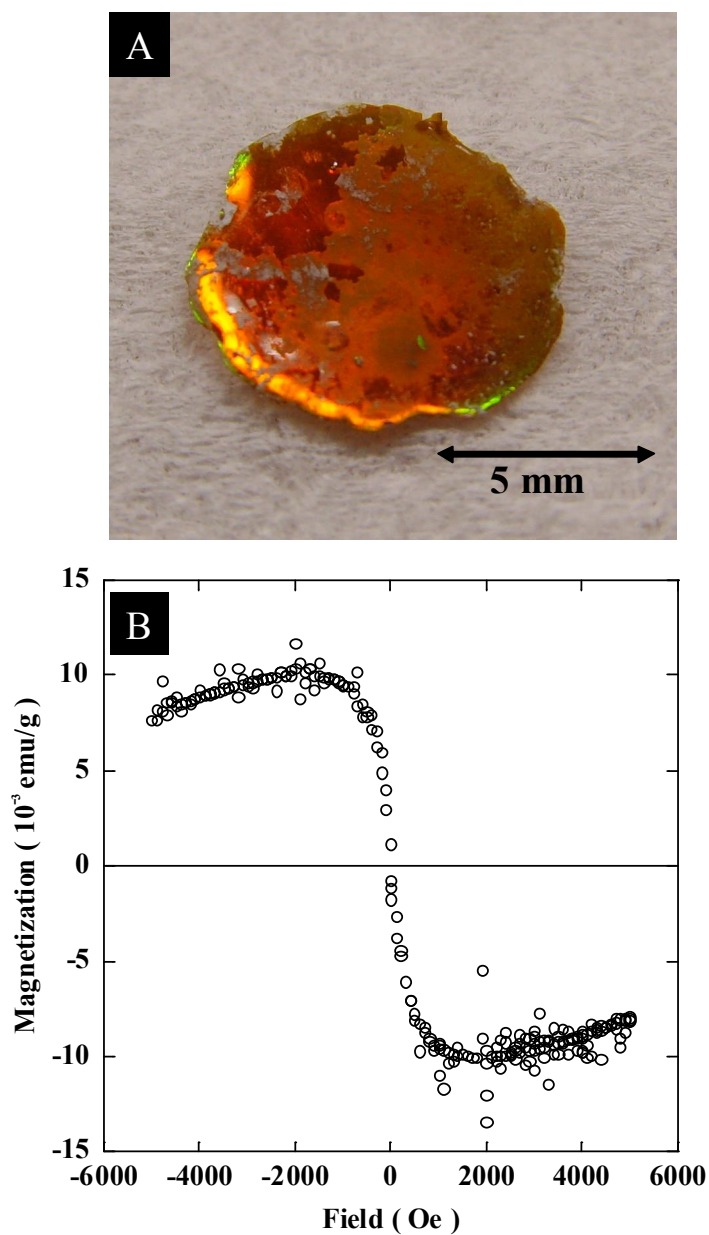
Figure 10.4. Photograph (A) and magnetization curves (B) of polymer replica containing magnetite nanoparticles.

10.4 Conclusion

The polymer replica containing magnetite nanoparticles showing a reflectivity at 612 nm and magnetic property was prepared by casting of polymer solution containing magnetic nanocrystals onto an oxidized porous silicon multilayer and then followed by the chemical dissolution of oxidized rugate PS template from the composite PS film. The polymer replica containing magnetite nanoparticles were robust and flexible. They exhibited an excellent reflectivity in reflection spectrum and displayed a magnetic property. SEM images indicate that the polymer replica replicated the photonic feature and the nanostructure of rugate PS master.

10.5 Reference

[1] A. C. Balazs, T. Emrick, and T. P. Russell, *Science* **314**, 1107 (2006).

[2] M. Tamborra, M. Striccoli, M. L. Curri, J. A. Alducin, D. Mecerreyes, J. A. Pomposo, N. Kehagias, V. Reboud, C. M. S. Torres, and A. Agostiano, *Small* **3**, 822 (2007).

[3] E. T. Thostenson, C. Y. Li, and T. W. Chou, *Compos. Sci. Technol.* **65**, 491 (2005).

[4] Q. X. Liu, Z. H. Xu, J. A. Finch, and R. Egerton, *Chem. Mater.* **10**, 3936 (1998).

[5] X. Wang, J. Liu, X. Feng, M. Guo, and D. Sun, *Mater. Chem. Phys.* **112**, 319 (2008).

[6] H. Sohn, S. Letant, M. J. Sailor, and C. Trogler, *J. Am. Chem. Soc.* **122**, 5399 (2000).

[7] C. A. Canaria, M. Huang, Y. Cho, J. L. Heinrich, L. I. Lee, M. J. Shane, R. C. Smith, M. J. Sailor, and G. M. Miskelly, *Adv. Funct. Mater.* **12**, 495 (2002).

[8] V. S. Lin, K. Motesharei, K. S. Dancil, M. J. Sailor, and M. R. Ghadiri, *Science* **278**, 840 (1997).

[9] C. Pacholski, M. Sartor, M. J. Sailor, F. Cunin, and G. M. Miskelly, *J. Am. Chem. Soc.* **127**, 11636 (2005).

[10] S. Jang, J. Kim, Y. Koh, Y. C. Ko, H.-G. Woo and H. Sohn, *J. Nanosci. Nanotechnol.* **7**, 4049 (2007).

[11] S. Jang, Y. Koh, J. Kim, J. Park, C. Park, S. J. Kim, S. Cho, Y. C. Ko and H. Sohn, *Mater. Lett.* **62**, 552 (2008).

[12] B. E. Collins, K. S. Dancil, G. Abbi, and M. J. Sailor, *Adv. Funct. Mater.* **12**, 187 (2002).

[13] F. Cunin, T. A. Schmedake, J. R. Link, Y. Y. Li, J. Koh, S. N. Bhatia, and M. J. Sailor, *Nat. Mater.* **1**, 39 (2002).

[14] S. Ilyas, and M. Gal, J. Mater. *Sci.-Mater. Electron.* **18**, S61 (2007).

[15] M. Ghulinyan, C. J. Oton, G. Bonetti, Z. Gaburro, and L. Pavesi, *J. Appl. Phys.* **93**, 9724 (2003).

[16] M. S. Yoon, K. H. Ahn, R. W. Cheung, H. Sohn, J. R. Link, F. Cunin, and M. J. Sailor, *Chem. Commun.* 680 (2003).

[17] Y. Y. Li, V. S. Kollengode, and M. J. Sailor, *Adv. Mater.* **17**, 1249 (2005).

[18] Y. Y. Li, F. Cunin, J. R. Link, T. Gao, R. E. Betts, S. H, Reiver, V. Chin, S. N. Bhatia, and M. J. Sailor, *Science* **299**, 2045 (2003).

[19] J. Kim, Y. Koh, S. Jang, Y. C. Ko, H.-G. Woo, and H. Sohn, *J. Nanosci. Nanotechnol.* **7**, 4165 (2007).

[20] J. Kim, C. Park, S. J. Kim, J. Park, Y. C. Ko, H.-G. Woo, and H. Sohn, *B. Kor. Chem. Soc.* **28**, 2079 (2007).

[21] Z. Li, Q. Sun, and M. Gao, *Angew. Chem. Int. Ed.* **44**, 123 (2005).

[22] M. Bruchez, M. Moronne, P. Gin, S. Weiss, and A. P. Alivisatos, *Science* **281**, 2013 (1998).

Chapter Eleven

# Novel Photoanode-structured Multiple Porous Polymer Replicas: A New Polymer-based Biosensor

11.1 Introduction

Photonic crystals containing a tunable nanostructure have attracted a considerable amount of attention owing to their unique optical properties, especially their photonic bandgaps [1]. The development of new methods to build photonic bandgap structures in a device is of great interest, as the fabrication of these structures using conventional lithographic methods is highly complex [2]. To achieve these issues, a replication is an excellent method for creating nanostructure by using porous materials such as self-assembled molecules [3], porous alumina [4], porous silicon (PS) [5], etc.

PS has been intensively investigated for a variety of applications, such as chemical [6] and biological sensors [7], optical band pass filters [8], and drug delivery [9], due to its high surface area, convenient surface chemistry, and optical signal transduction capability. Multi-encoded rugate (MER) PS has emerged as an attractive material since it displays both photonic structures and multi-optical codes [10-13]. However, PS is limited in its chemical and mechanical stability in many applications because a free-standing PS film is typically very brittle and shatters when subjected to minor shear stresses [14-15]. To eliminate these issues, polymer nanostructured materials may be an alternative for applications in photonics and

optical data storage. Since the discovery of polymer replicas by Sailor et al., PS templates have been used for producing drug delivery materials [5].

In the present work, porous polystyrene replicas (PPR) showing many independent optical codes were prepared by the casting of a polystyrene solution onto an oxidized MER PS film. These PPR may offer the potential application for the detection of biomolecules. The preparation of the multi-code PPR follows the sequence shown in Scheme 1.
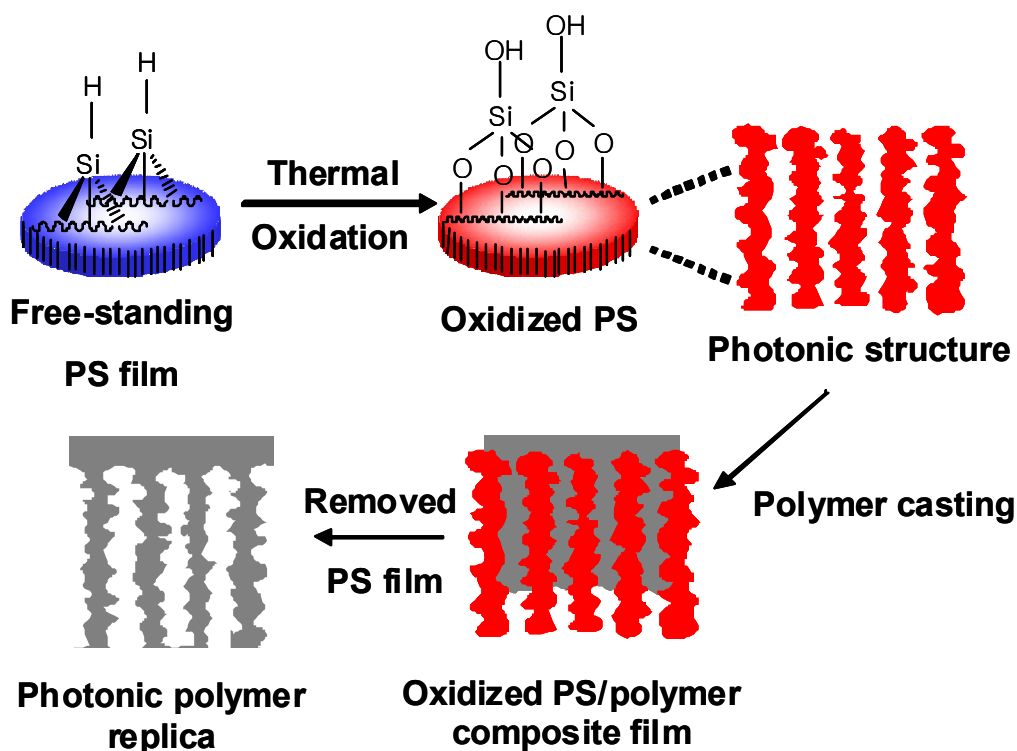
Scheme 11.1. The preparation process of the multi-code PPR.

11.2 Experiments

11.2.1 Materials

Biotinyl-L-lysine (98%, Aldrich Chemicals), phosphate buffer solution (PBS, ACS reagent, Aldrich Chemicals), HF (ACS reagent, Aldrich Chemicals), absolute ethanol (ACS reagent, Aldrich Chemicals), polystyrene (Aldrich, Mw = 280,000), toluene (Fisher Scientific), and avidin (Aldrich Chemicals) were used without further purification.

11.2.2 Preparation of MER PS

Samples were prepared by electrochemical etching of heavily doped p^{++}-type silicon wafers (boron-doped, polished on the <100> face, resistivity of 0.8 - 1.2 m $\Omega \circ cm$, Siltronix, Inc.). The etching solution consisted of a 3:1 v/v mixture of aqueous 48% hydrofluoric acid and absolute ethanol. Galvanostatic etching was carried out in a Teflon cell by using a two-electrode configuration with a Pt mesh electrode. A sinusoidal current density waveform varying between 51.5 and 74.6 $mAcm^{-2}$ was applied. The anodization current was supplied by a Keithley 2420 high-precision constant current source which was controlled by a computer to allow the formation of PS multilayers. The hertz values for each of the sine components varied from 0.36 to 0.42 Hz, with a spacing of 0.02 Hz between each sine component.

11.2.3 Preparation of photonic polymer replicas

The resulting MER PS film was removed from the silicon substrate by applying an electropolishing current at 400 mA·cm^{-2} for 2 min in a solution of 48% aqueous HF and ethanol (3:1 v/v) and then at 22 mA·cm^{-2} for 2 min in a solution of 48% aqueous HF and ethanol (1:15 v/v) to obtain a free-standing MER PS. MER PS films were thermally oxidized in a furnace at 350 ℃ for 5 h. In a typical preparation process, 4 g of polystyrene was dissolved in 20 mL of toluene. The toluene solution was cast into the porous SiO$_2$ films and the samples were annealed in an oven at 110 ℃ for 1 h. The oxidized MER PS matrix from the composite films was then removed in aqueous 8% HF solution for 12 h. After the removal of the oxidized MER PS template by chemical dissolution, the polymer castings replicate the photonic features and the nanostructure of the master.

11.2.4 Instrumentation and data acquisition

The anodization current was supplied by a Keithley 2420 high-precision constant current source which was controlled by a computer to allow the formation of PS multilayers. Optical reflectivity spectra were measured using a tungsten-halogen lamp and an Ocean Optics S2000 CCD spectrometer fitted with a fiber optic input. The reflected light collection end of the fiber optic was positioned at the focal plane of the optical microscope. The morphologies of MER PS film and polymer replica were observed using a cold field emission scanning electron microscope (FE-SEM, S-4700, Hitachi). Surface characterization of fresh and oxidized MER PS samples for chemical properties was conducted using a Fourier-transform infrared

device (FT-IR, Nicolet 5700, Thermo Electron Co.). The MER PS film and polymer replica were characterized by X-ray diffractometry (XRD, D/MAX-3C, Riguku Co.) with CuKα radiation (0.15406 nm). The XRD patterns were collected in the 2 theta range of 3-90° at room temperature.

11.3 Results and Discussion

Electrochemical etching offers the opportunity to modulate the porosity in depth and facilitates the fabrication of structures with any refractive index profile. MER PS was prepared by applying a computer-generated composite waveform in which the individual sine components were summed together. The MER PS samples displayed very sharp reflection lines corresponding to reflection resonances in the optical spectrum. After the generation of MER PS, the resulting PS films were removed from the silicon substrate by an applying of electropolishing current to obtain a free-standing MER PS film. Thermal oxidation of these films was then carried out. The reflection spectra of the oxidized MER PS films are shown in Figure 1 (dashed line).
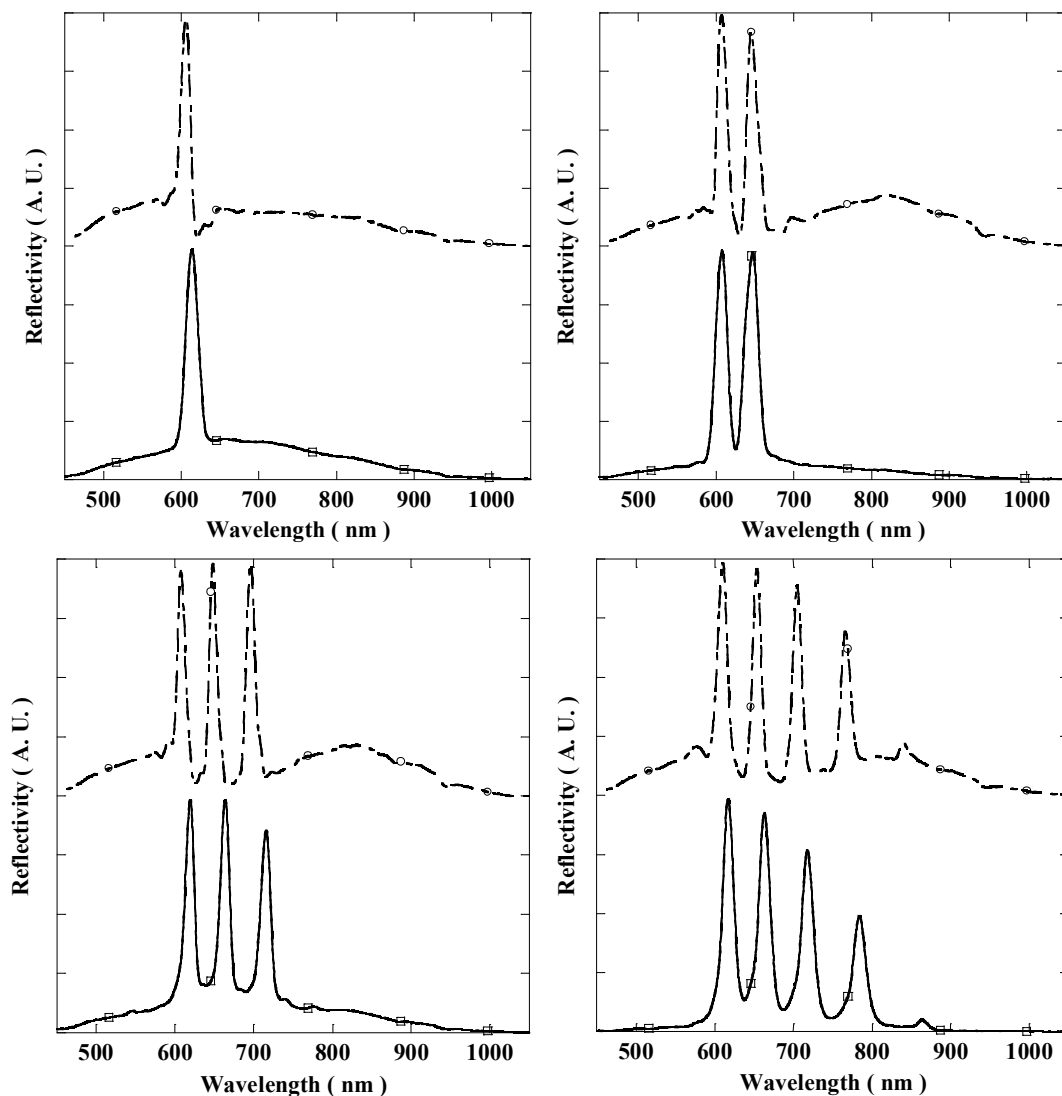
Figure 11.1. Optical reflection spectra of free-standing oxidized MER PS films (dashed line), and multi-encoded PPR (solid line). Samples etched at 0.42, 0.40, 0.38, and 0.36 Hz exhibited sharp lines at 610, 653, 705, and 766 nm for the oxidized MER PS and at 616, 661, 715, and 780 nm for the PPR, respectively.

Polystyrene was dissolved in toluene and cast on the top surface of an oxidized MER PS film. After drying in ambient atmosphere, the resulting composite film was annealed in an oven to fill the pores with the polymer. After removal of the oxidized MER PS from the composite film in an HF solution, the PPR was successfully obtained. This PPR exhibits sharp reflection multi-peaks in the reflectivity spectrum, as shown in Figure 1 (solid line), replicating the photonic features of the oxidized MER PS master. The spectral bands of the PPR samples have a full-width at half-maximum (FWHM) of approximately 13-18 nm, which is much narrower than that of the fluorescence spectrum of a fluorescent organic molecule or quantum dot [16].

To determine the presence of silicon, X-ray diffractometry (XRD) measurements of the MER PS film and the PPR film were taken. Figure 2 shows the XRD pattern of the prepared samples. The peak at about 69°, which can be seen in Figure 2 (top), is attributed to the diffraction from the crystalline silicon of the MER PS film. However, the X-ray diffraction pattern of the PPR in Figure 2 (bottom) indicates that the oxidized MER PS template was completely removed from the composite films and that no crystalline silicon remains.
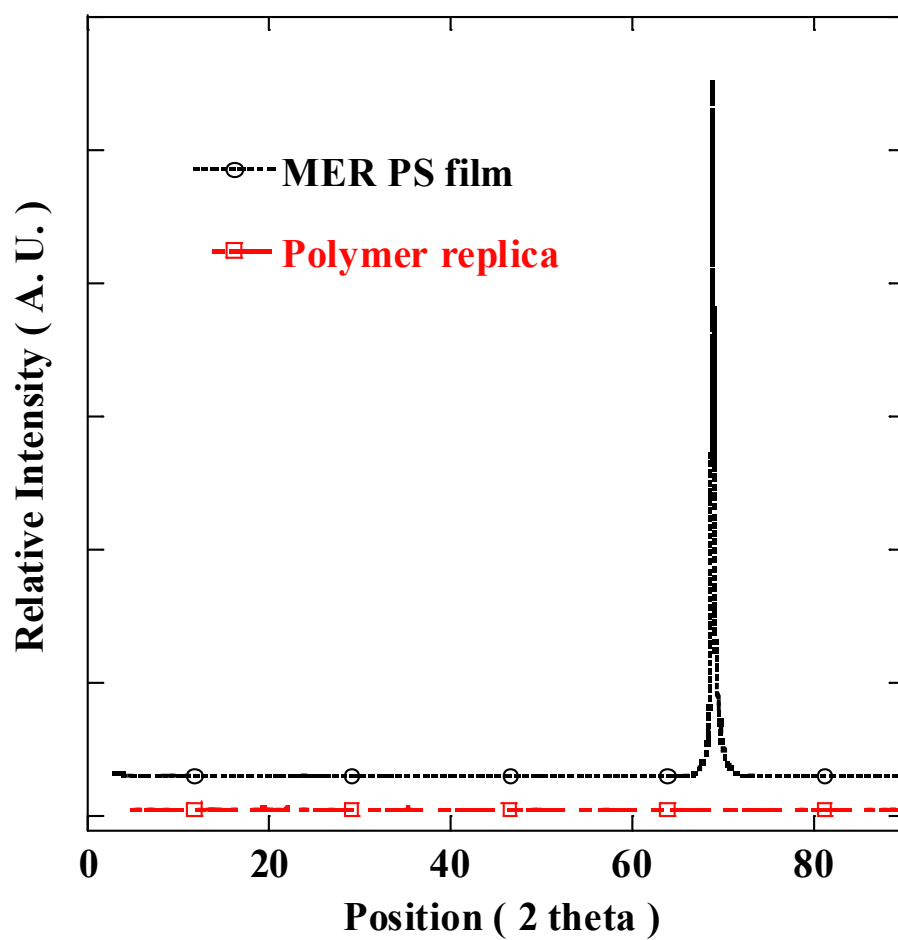
Figure 11.2. XRD patterns of MER PS film and a PPR.

A photograph of a rugate-structured PPR is shown in Figures 3A and 3B and illustrates that its color results from the reflection of the PPR. The PPR is also highly flexible and displays significantly improved mechanical stability without apparent degradation. Its optical property is retained upon flexing. The surface morphology of PPR was obtained with cold field emission scanning electron microscope (FE-SEM); this is shown in Figure 3C. The FE-SEM image of the rugate-structured PPR indicates that the morphology of the polymer film has a photoanode structure of MER PS. These PPRs are stable in aqueous solutions for several days without any degradation and can be useful for applications such as optical code systems, vapor sensors, deformable and tunable optical filters, and bioresorbable materials.
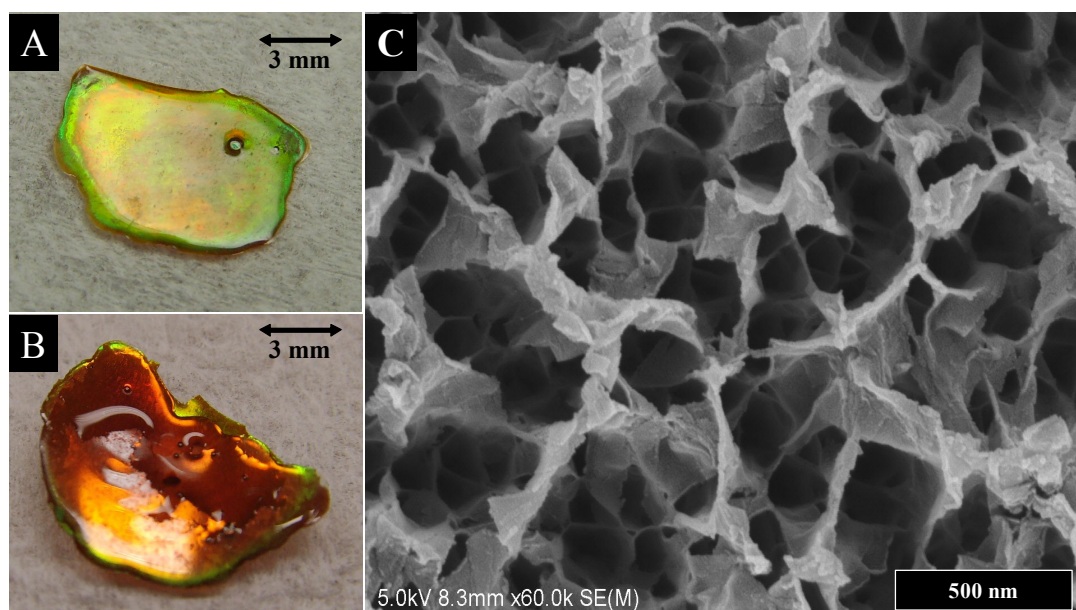
Figure 11.3. Photographs and SEM image of a photonic polymer replica. (A) Polymer replica obtained from PS etched at 0.42 and 0.40 Hz. (B) Polymer replica obtained from PS etched at 0.42, 0.40, 0.38, and 0.36 Hz. (C) Surface morphology of sample B.

In a basic demonstration for biosensor application using PPR, the biotin-incorporated PPR prepared by casting a polymer solution containing biotinyl-L-lysine was used to detect avidin. The biotin-incorporated PPR was placed in detection chamber. Aqueous phosphate buffer solution (PBS) was flushed to perform an initial measurement of reflectivity and to check stability of the reflectivity measurement. The PBS containing 0.2 mg/mL of avidin was then flushed to detect avidin.

Figure 4 showed the reflection spectra (A) under the exposure of avidin to the biotin-incorporated PPR and the difference between the two spectra (B). As expected, exposition to a solution of avidin to the biotin-incoporated PPR resulted in an increase in the red shift of reflection peaks, indicative of a change in refractive index induced by binding of the avidin into the biotin.
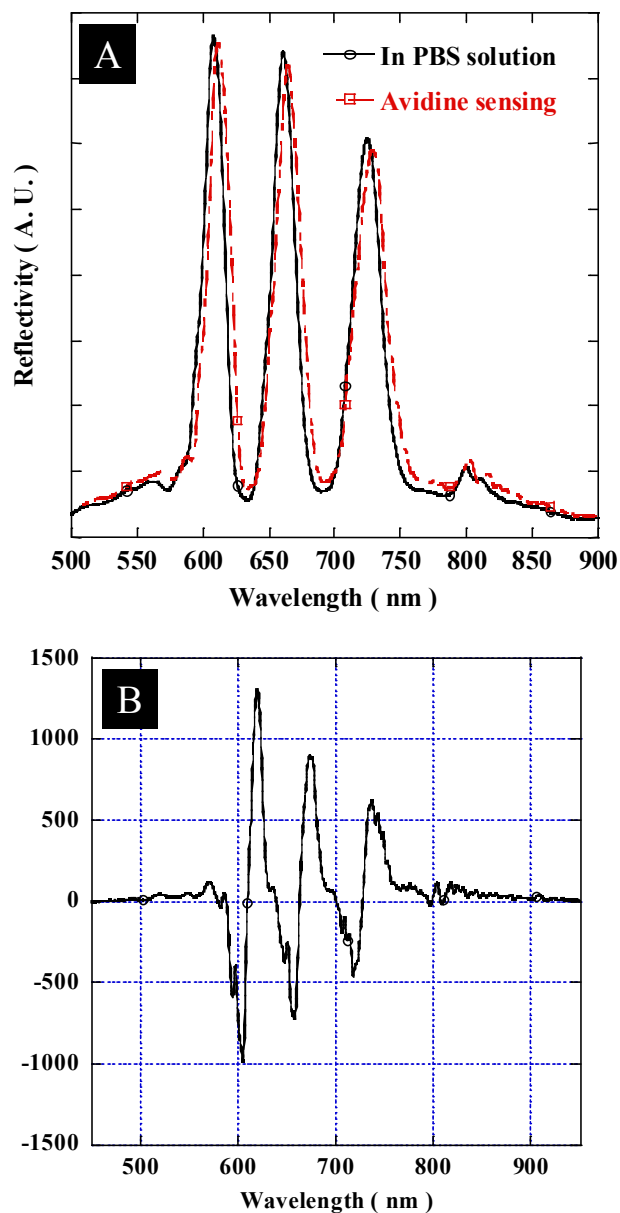
Figure 11.4. (A) Change of reflection peaks using biotin-incoporated polymer replica before (solid line) and after (desh line) exposure of avidin and (B) the difference between two spectra obtained in the presence and absence of avidin.

11.4 Conclusion

In summary, novel photoanode-structured of porous polystyrene thin films containing many independent codes were fabricated by replicating the photonic features and the nanostructure of a multi-encoded rugate porous silicon master. These findings could allow the development of sensing materials for the detection of biomolecules. This method provides an opportunity to construct an elaborate optical nanostructure in the development of polymer materials for photonic applications.

11.5 Reference

[1] C. Paquet and E. Kumacheva, *Mater. Today* **11**, 48 (2008).

[2] W. Zhang, D. Zhang, T. Fan, J. Gu, J. Ding. H. Wang, Q. Guo, and H. Ogawa, *Chem. Mater.* **21**, 33 (2009).

[3] A.-H. Lu and F. Schüth, *Adv. Mater.* **18**, 1793 (2006).

[4] C. M. Bruinink, M. Burresi, M. J. de Boer, F. B. Segerink, H. V. Jansen, E. Berenschot, D. N. Reinhoudt, J. Huskens, and L. Kuipers, *Nano Lett.* 8, 2872 (2008).

[5] Y. Y. Li, F. Cunin, J. R. Link, T. Gao, R. E. Betts, S. H. Reiver, V. Chin, S. N. Bhatia, and M. J. Sailor, *Science* **299**, 2045 (2003).

[6] H. Sohn, S. Létant, M. J. Sailor, and W. C. Trogler, *J. Am. Chem. Soc.* 2122, 5399 (2000).

[7] V. S.-Y. Lin, K. Motesharei, K.-P. S. Dancil, M. J. Sailor, and M. R. Ghadiri, *Science* **278**, 840 (1997).

[8] J. Kim, S. Jang, Y. Koh, C. Park, H.-G. Woo, S. Kim, and H. Sohn, *J. Nanosci. Nanotechnol.* **8**, 4951 (2008).

[9] E. J. Anglin, L. Cheng, W. R. Freeman, and M. J. Sailor, *Adv. Drug Deliv. Rev.* **60**, 1266 (2008).

[10] F. Cunin, T. A. Schmedake, J. R. Link, Y. Y. Li, J. Koh, S. N. Bhatia, and M. J. Sailor, *Nat. Mater.* **1**, 39 (2002).

[11] S. O. Meade, M. S. Yoon, K. H. Ahn, and M. J. Sailor, *Adv. Mater.* **16**, 1811 (2004).

[12] M. J. Sailor and J. R. Link, *Chem. Commun.* 1375 (2005).

[13] S. O. Meade, M. Y. Chen, M. J. Sailor, and G. M. Miskelly, *Anal. Chem.* **81**, 2618 (2009).

[14] Y. Y. Li, V. S. Kollengode, and M. J. Sailor, *Adv. Mater.* **17**, 1249 (2005).

[15] M. Ghulinyan, C. J. Oton, G. Bonetti, Z. Gaburro, and L. Pavesi, *J. Appl. Phys.* **93**, 9724 (2003).

[16] M. Bruchez, M. Moronne, P. Gin, S. Weiss, A. P. Alivisatos, *Science* 281, 2013 (1998).

Acknowledgments

The completion of my doctoral studies would not have been possible without the help of many people. First of all, I would like to express my sincere gratitude to my advisor respected **Professor Honglae Sohn**, for his love, guidance, patience, support and friendship both professionally and personally during the entire course of this dissertation. He allowed me many opportunities to learn and grow the course of my research. Without his help, I would not have developed the independent scientific insight. I would also like to thank to many **Professors Kidong Song**, **Sungdong Cho**, **Moonjoo Ko** and **Beomgyu Lee** in department of chemistry for their great guidance and instruction in scientific area. I would especially like to thank to **Professor Hee-Gweon Woo** from Chonnam national university for kindly accepting to be the chair of the graduation committee and also would like to thank to **Professor Hyun-Dam Jeong** from Chonnam national university and **Professor Yongmin Kim** from Dankook university.

I would also like to thank to my fellow graduate students that I have worked with over the past few years, my friends **Jongsun Kim**, and **Sung Gi Kim** for their sincere friendship and giving me a preasure, my juniors **Younghee Gweon**, **Jaehyun Park**, **Cheolyoung Park**, **Sung Jin Kim**, **Kyoungsun Jung**, **Sung Gi Lee**, **Jinseok Yang**, **Bomin cho**, **Tae-Eun Choi**, **Sunghoon Jin**, and **Sungyong Um** for their cooperation and help to my research. Specially, I would like to thank to **Dr. Seunghyun Jang** and **Mr. Youngdae Koh** who has appreciate the reinforcement and help.

Finally, I greatly appreciate the support and endless love of **my mother**. I will always love and keep her. This thesis is dedicated to all of them.

감사의 글

　2005년도 처음으로 대학원에 입학하여 어느덧 2010년이 다가오면서 저의 작은 결실을 맺게 되었습니다. 석사학위를 비롯해 박사학위를 받는 동안 조선대학교 화학과에서 너무나 많은 도움을 받으면서 여기까지 온 거 같습니다. 무엇보다도 먼저, 여러모로 부족한 저를 학문의 길로 이끌어 주시고 보다 깊은 학문적 성취를 위해 아낌없는 충고와 가르침을 주신 저의 지도교수님이신 손홍래 교수님께 맘을 담아 깊이 감사드립니다. 교수님의 크나크신 가르침을 평생 마음에 새기고 기억하겠습니다. 그리고 대학원 과정동안 각각의 분야에서 많은 학문적 가르침과 관심을 보여주신 송기동 교수님, 조성동 교수님, 고문주 교수님, 이범규 교수님께도 깊은 감사드립니다. 또한 바쁘신 와중에도 저의 논문심사를 맡아주신 심사위원장이신 전남대학교 우희권 교수님, 심사위원이신 단국대학교 김용민 교수님, 전남대학교 정현담 교수님께도 감사드립니다. 대학원 과정동안 저와 함께하며 고생한 우리 광나노소재연구실 선배들인 범석이형, 진우형, 형준이형, 대혁이형과 동기들인 성기, 종선이, 또한 사랑하는 후배들 용희, 재현, 철영, 성진, 경선, 성기, 진석, 보민, 태은, 성용, 성훈이에게 너무나 고맙고 감사의 말을 전하고 싶습니다. 특히, 박사과정동안 함께 고생한 승현이형이랑 영대에게 너무나 고맙다는 말을 전하고 싶습니다.

　항상 끝없는 사랑과 지지를 아껴주시지 않으신 사랑하는 어머니에게도 머리 숙여 깊은 감사의 말을 전합니다. 아마 이들의 관심과 사랑이 없었더라면 힘들고 어려운 매순간마다 이겨내기 힘들었을 것입니다. 이 모든 분들의 가르침과 사랑의 빚을 평생 마음속에 간직하며 보다 더 발전되고 사회에 공한할 수 있는 사람이 되도록 노력하며 살겠습니다. 이 모든 분들께 작은 결실인 이 논문을 바침니다.

저작물 이용 허락서

학 과	화학과	학 번	20077318	과 정	박사
성 명	한글: 김 지 훈 한문: 金 地 訓 영문: Kim, Jihoon				
주 소	광주광역시 북구 일곡동 현대2차APT 205-101				
연락처	E-mail : jhkim1217@dreamwiz.com				
논문제목	한글 : 광결정고분자와 나노소재를 기초로한 새로운 화학 영문 : **New Chemistry Based on Photonic Crystal Polymers and Nanomaterials**				

본인이 저작한 위의 저작물에 대하여 다음과 같은 조건아래 조선대학교가 저작물을 이용할 수 있도록 허락하고 동의합니다.

- 다   음 -

1. 저작물의 DB구축 및 인터넷을 포함한 정보통신망에의 공개를 위한 저작물의 복제, 기억장치에의 저장, 전송 등을 허락함.
2. 위의 목적을 위하여 필요한 범위 내에서의 편집·형식상의 변경을 허락함.
   다만, 저작물의 내용변경은 금지함.
3. 배포·전송된 저작물의 영리적 목적을 위한 복제, 저장, 전송 등은 금지함.
4. 저작물에 대한 이용기간은 5년으로 하고, 기간종료 3개월 이내에 별도의 의사표시가 없을 경우에는 저작물의 이용기간을 계속 연장함.
5. 해당 저작물의 저작권을 타인에게 양도하거나 또는 출판을 허락을 하였을 경우에는 1개월 이내에 대학에 이를 통보함.
6. 조선대학교는 저작물의 이용허락 이후 해당 저작물로 인하여 발생하는 타인에 의한 권리 침해에 대하여 일체의 법적 책임을 지지 않음.
7. 소속대학의 협정기관에 저작물의 제공 및 인터넷 등 정보통신망을 이용한 저작물의 전송·출력을 허락함.

동의여부 : 동의 (○), 반대 (   )

2009년 2월   일

저작자: 김 지 훈   (서명 또는 인)

조선대학교 총장 귀하